S03040000-DAC10011

Second Target Station Project: Thermohydraulic Analysis for the Moderator Reflector Assembly (MRA)

Min-Tsung Kao

April 2026

Draft. Document has not been reviewed and approved for public release.

ORNL IS MANAGED BY UT-BATTELLE LLC FOR THE US DEPARTMENT OF ENERGY

S03040000-DAC10011

Second Target Station Project

THERMOHYDRAULIC ANALYSIS FOR THE MODERATOR REFLECTOR ASSEMBLY (MRA)

Min-Tsung Kao

April 2026

Prepared by
OAK RIDGE NATIONAL LABORATORY
Oak Ridge, TN 37831
managed by
UT-BATTELLE LLC
for the
US DEPARTMENT OF ENERGY
under contract DE-AC05-00OR22725

Approvals

Document Title		ISSUE DATE:
PREPARED BY Min-Tsung Kao	PROJECT Second Target Station	DOCUMENT NUMBER: S03040000-DAC10011

	Signature / Date					
	Rev. 00	Date	Rev. 01	Date	Rev. 02	Date
Analyst						
Reviewer						
Lead Engineer						
L2 Manager						
Configuration Authority						

Revision	Description
00	Initial Release

CONTENTS

ABSTRACT

The Moderator Reflector Assembly (MRA) at the Oak Ridge National Laboratory (ORNL) Second Target Station (STS) is designed to moderate fast spallation neutrons into high-brightness cold neutrons for delivery to neutron scattering instruments. This report evaluates the thermal-hydraulic performance of the current MRA design under nominal operating conditions using Computational Fluid Dynamics (CFD) simulations.

The primary objective of this study is to demonstrate that the MRA design meets all thermal-hydraulic requirements defined in the MRA requirements document (S03040000-SR0001), including limits on cryogenic hydrogen temperature and density, structural and coolant temperatures, and pressure drops. Additionally, the report evaluates air accumulation in the lower reflector vessel during the initial water-filling process and assesses its impact on thermal performance.

Results indicate that the hydrogen moderator operates stably with a maximum temperature of **24.5 K**, well below the **32 K limit**, and an average density above **72 kg/m³**, ensuring effective cold neutron production. The hydrogen loop pressure drop is **0.105 bar**, satisfying the design limit. Thermal response is effectively quasi-steady, with an estimated temperature rise of approximately **0.08 K per pulse**, indicating negligible inter-pulse fluctuations.

All structural and coolant temperatures remain within allowable limits, with peak values of **73.1°C in aluminum**, **54.9°C in beryllium**, **84.6°C in steel**, and **51°C in water**, all below their respective design constraints. Water pressure drops across all cooling circuits remain below **15 psi**.

Transient multiphase simulations show that air introduced into the lower reflector vessel is effectively vented during operation, with only a negligible residual volume (~4.5 cm³) under extreme conditions. Conjugate heat transfer analysis confirms that this residual air has no measurable impact on temperature distribution or heat transfer performance.

Overall, the analysis confirms that the STS MRA design complies with all thermal-hydraulic requirements with adequate safety margins and demonstrates stable and robust operation suitable for reliable cold neutron production.

1. INTRODUCTION

The Second Target Station (STS) will be the third neutron source and will complement the two existing operating neutron sources, the High Flux Isotope Reactor and the Spallation Neutron Source First Target Station (FTS), at Oak Ridge National Laboratory (ORNL). The STS uses a tungsten (W) target at a density of 19.3 g/cm^3, whereas the FTS uses the mercury (Hg) target with a density of 13.6 g/cm^3 density. With the higher density of the W target, the S+TS can produce approximately 25 times higher peak brightness and approximately 4 to 5 times higher time-averaged brightness than the FTS [1]. The STS target wheel is approximately 1.2 m in diameter, consists of 20 separate 0.5 mm tantalum (Ta)-clad W targets, completes one full revolution in 4/3 s (rotational speed of 45 rpm), and is synchronized with a 700 kW, 15 Hz pulsed proton beam (15 Hz × 4/3 s = 20 pulses). Approximately 8.3% of the total beam power is directly deposited in the MRA. The target wheel is sandwiched between the upper cylindrical moderator and the lower triangular tube moderator of the Moderator Reflector Assembly (MRA). When the proton beam bombards the target wheel, spallation reactions in the W blocks generate fast neutrons, which are slowed in the MRA. The upper cylindrical moderator is optimized for peak brightness. The lower tube moderator is optimized for time-integrated brightness because neutrons travel through more moderating materials (liquid hydrogen) before exiting, resulting in more total neutrons per pulse. STS MRA requirements in Table 1.

Table 1. Thermal hydraulics requirements of STS MRA.

Requirement Name	Codebeamer ID	Requirement
MRA Water Loop		
MRA Aluminum Temperature Requirement	2325	The MRA aluminum 6061-T6 structures shall have a maximum operating temperature of 100 °C.
MRA Stainless Steel Temperature Requirement	2326	The MRA stainless steel structures shall have a maximum operating temperature of 200 °C.
MRA Beryllium Temperature Requirement	2327	The MRA beryllium shall have a maximum operating temperature of 100 °C.
MRA Water Temperature Requirement	2328	The MRA cooling water shall have a maximum temperature of 100 °C.
MRA Upper Premoderator Pressure Drop Requirement	2362	The MRA upper premoderator water loop shall have a pressure drop of less than 15 psi at 7.5 gpm and 32.2 °C inlet temperature.
MRA Lower Premoderator Pressure Drop Requirement	2363	The MRA lower premoderator water loop shall have a pressure drop of less than 15 psi at 7.5 gpm and 32.2 °C inlet temperature.
MRA Upper Reflector Pressure Drop Requirement	2364	The MRA upper reflector water loop shall have a pressure drop of less than 15 psi at 7.5 gpm and 32.2 °C inlet temperature.
MRA Lower Reflector Pressure Drop Requirement	2365	The MRA lower reflector water loop shall have a pressure drop of less than 15 psi at 7.5 gpm and 32.2 °C inlet temperature.
MRA Backbone Pressure Drop Requirement	2366	The MRA backbone water loop shall have a pressure drop of less than 15 psi at 15 gpm and 32.2 °C inlet temperature.
MRA Hydrogen Loop		
MRA Hydrogen Loop Pressure Drop Requirement	2356	The MRA hydrogen loop pressure drop shall be less than 0.15 bar @ 0.5 l/s and 18.34 K.
MRA Moderator Hydrogen Density Requirement	2888	The hydrogen in both moderators shall have a minimum average density of 72.0 kg/m^3.
MRA Moderator Hydrogen Maximum Temperature Requirement	2889	The hydrogen temperature shall at no point in the moderators exceed 32 K.

2. SOFTWARE AND HPC RESOURCE

Geometry modification, simplification for analysis, and fluid volumes extraction are conducted in SpaceClaim 2024 R2 [2]. All results in this report are from computational fluid dynamics (CFD) analyses using the commercial software STAR-CCM+ 2306 [3]. STAR-CCM+ is a finite-volume method (FVM)-based multiphase CFD code and is widely used for conjugate heat transfer, single and multiphase flow problems. All simulations were run on the Bernie cluster at ORNL, which comprises six compute nodes, each with 64 CPU cores (2 x AMD EPYC™ 9355 Processor 32-core 3.55GHz 256MB Cache, 280W) and 768 GB of RAM (24 x 32GB PC5-41600 5600MHz DDR5 ECC RDIMM). Depending on the number of meshes generated and the complexity of the problems, 1 – 3 nodes were used for the CFD analyses in this report.

3. GEOMETRY[1]

The relative position of the Moderator Reflector Assembly (MRA) within the Second Target Station (STS) Core Vessel (CV) is shown in Figure 1. As illustrated in Figure 2, Figure 3, and Figure 4, the MRA consists of five main components: the hydrogen loop (upper cylindrical moderator and lower tube moderator), shield block, backbone (upper, middle, and lower blocks), and the upper and lower reflector vessel assemblies.

The hydrogen loop configuration is shown in Figure 3. Liquid hydrogen enters at a flow rate of 0.5 L/s and a temperature of 18.34 K through Invar tubes, flows downward into the aluminum vessel of the cylindrical moderator, exits via the annulus side of the Invar tubes, continues downward to the tube moderator, and finally exits at the top of the assembly.

[1] The geometry file used in CFD analysis:
https://ornl.sharepoint.com/sites/sts/targetsystems/Shared%20Documents/Forms/AllItems.aspx?id=%2Fsites%2Fsts%2Ftargetsystems%2FShared%20Documents%2FS%2E03%2E02%20Target%20Assembly%2F99%5FSANDBOX%2FKAO%2F2026%2FSTS%5FMRA%2F0%5FMRA%5FFDR&viewid=9be9bc88%2D5a13%2D48c7%2D9fff%2Dd22f94ffdeb5
CFD_CAD.zip/
mra_am_001_asm_MTK_Delete_Unwanted_Components_Regroup_Fix_H2_Loop_and_Chamfers_Fix_Backbone_Combine_3_Solid+Fluid.stp

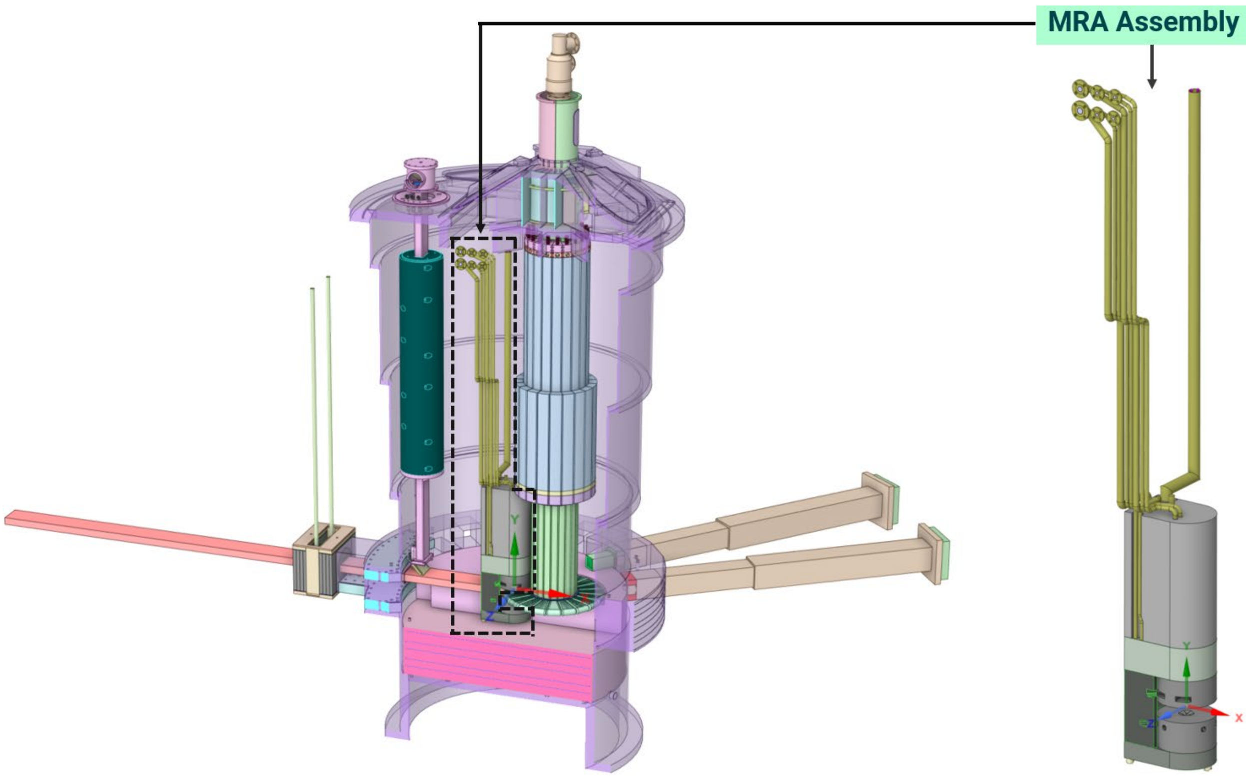

Figure 1. Second target station PBM, TVP, CV, target assembly, and MRA.

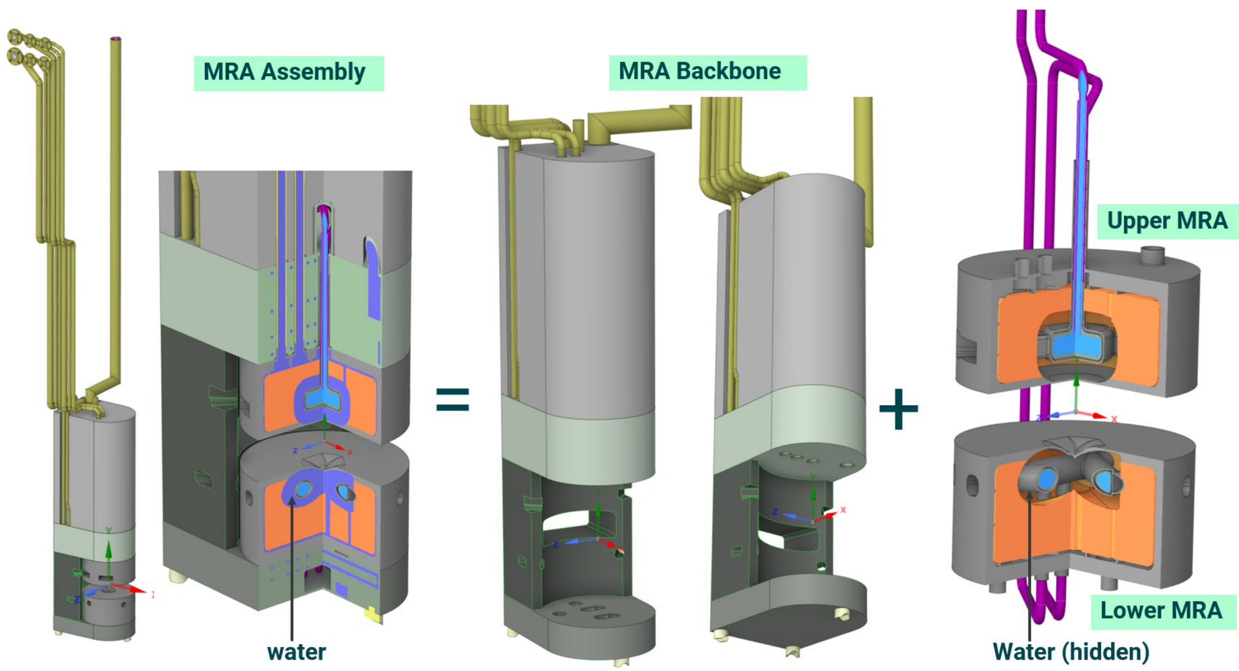

Figure 2. Moderator Reflector Assembly (MRA).

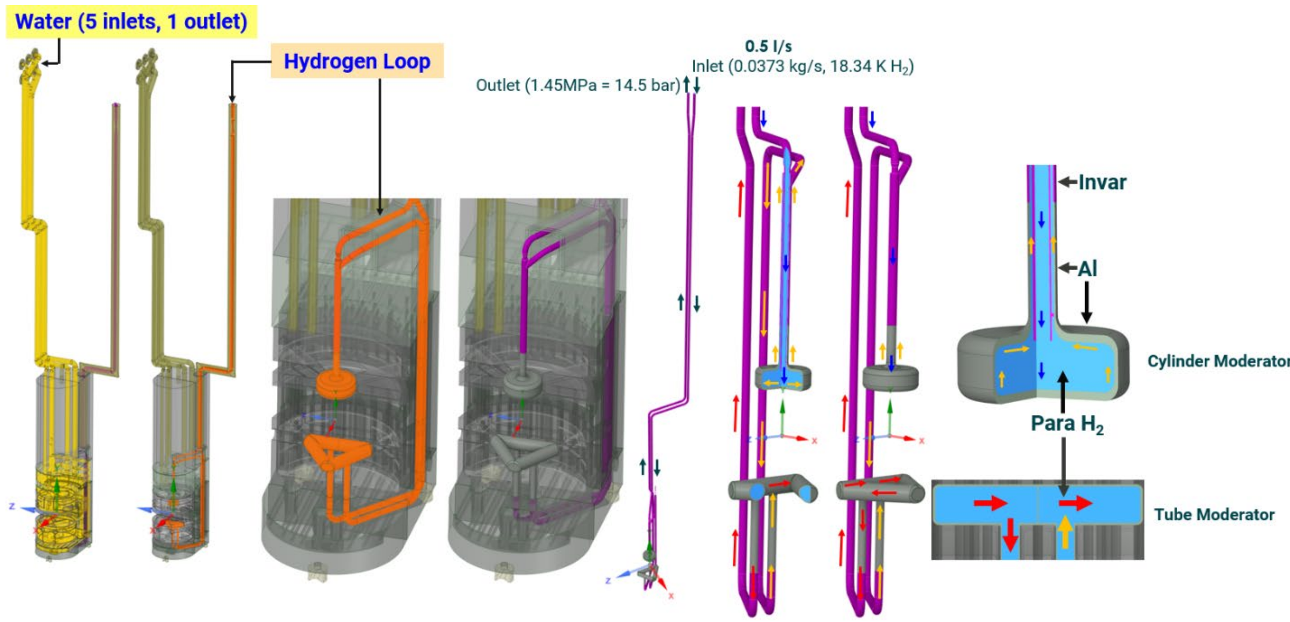

Figure 3. Hydrogen loop in MRA.

Since hydrogen nuclei (protons) have nearly the same mass as neutrons, they provide maximum energy transfer per elastic collision. As a result, liquid hydrogen operated at cryogenic temperatures (~18–21 K) in the MRA serves as an excellent moderator, efficiently slowing fast neutrons (~MeV) produced by spallation reactions in the tungsten target blocks to cold neutron energies (~5 meV). These long-wavelength cold neutrons are well suited for probing structures ranging from nanometers to hundreds of nanometers in soft matter, polymers, biological molecules, and magnetic domains. The Second Target Station (STS) is designed to complement the First Target Station (FTS) at the Spallation Neutron Source (SNS) by providing higher-brightness cold neutron beams for experiments requiring long-wavelength neutrons, whereas the FTS is primarily optimized for thermal neutron production.

Compared with heavy nuclei materials such as tungsten, which generally exhibit higher neutron absorption cross sections and more forward-peaked scattering behavior, beryllium is a light material characterized by a low neutron absorption cross section and a high elastic scattering cross section. Its low atomic mass leads to more isotropic scattering in the center-of-mass frame, increasing the probability of large-angle scattering events that redirect neutrons back toward the cryogenic liquid hydrogen moderator. In addition, beryllium can contribute to neutron multiplication through threshold (n,2n) reactions under high-energy neutron irradiation, thereby improving overall neutron economy in the reflector system.

Water (H_2O) also contains hydrogen and is therefore effective at moderating fast neutrons to thermal energies (~25 meV) at room temperature. As shown in Figure 5, in the MRA, the water located between the liquid hydrogen moderator and the beryllium reflector functions as a thermal neutron moderator (i.e., a premoderator for cold neutrons). Outside the beryllium solid reflector, water serves as coolant for beryllium and aluminum reflector vessels.

Although liquid hydrogen is an excellent cold neutron moderator, it is cryogenic, flammable, and has limited heat removal capability. Fast neutrons from the spallation target are highly energetic (MeV range) and can deposit excess heat in the liquid hydrogen moderator, potentially leading to hydrogen boiling, density variations, and associated safety concerns. In contrast, as a premoderator, water has a high heat capacity, enabling efficient heat removal and partially moderating fast neutrons before they enter the cryogenic hydrogen moderator.

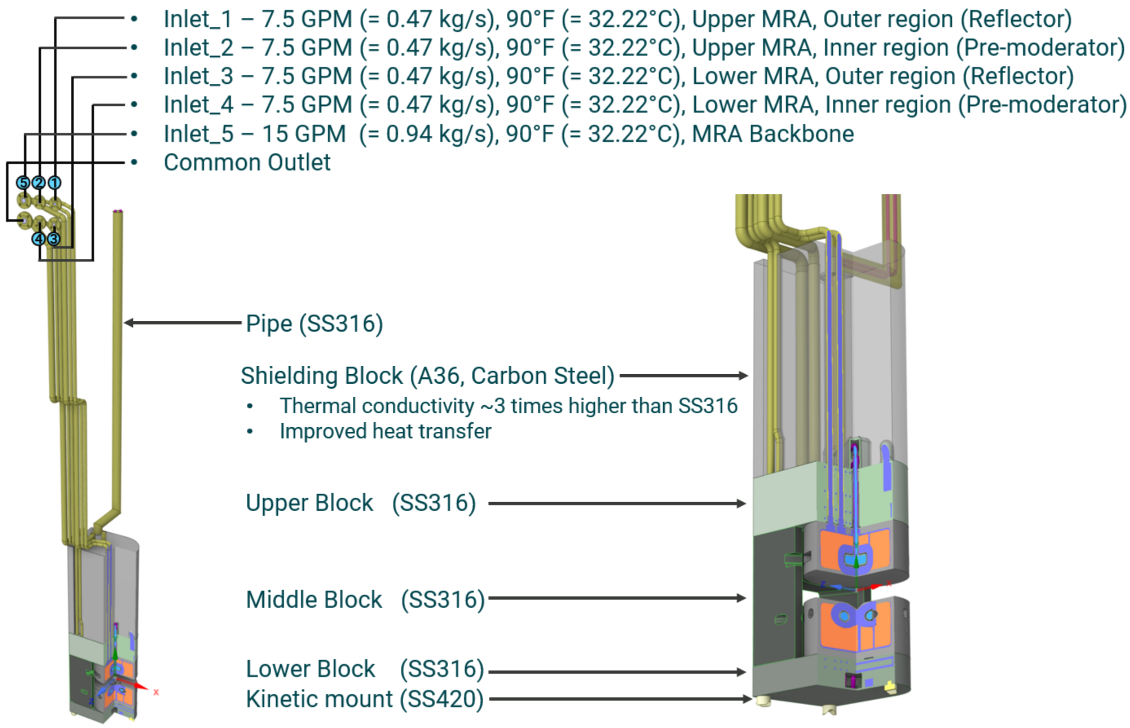

Figure 4. Overview of MRA.

Figure 4 illustrates the five water-cooling loops integrated into the MRA: two serving the upper MRA, two serving the lower MRA, and one serving the backbone. The backbone consists of lower, middle, and upper structural blocks fabricated from SS316 stainless steel. Three SS420 kinetic mounts are attached to the lower block. A shield block, located atop the upper block and not actively water-cooled, is constructed from A36 carbon steel. This material was selected for its thermal conductivity, approximately three times greater than that of stainless steel, enhancing passive heat dissipation. The entire MRA assembly—including the shield block, backbone, upper MRA, lower MRA, and kinetic mounts—is supported by Shield Block #1 within the Core Vessel (CV).

As shown in Figure 5, the beryllium components located within the MRA aluminum vessel are in direct contact with cooling water, with no additional containment vessel. This direct interface ensures efficient heat removal from the beryllium. Additionally, the hydrogen loop vessels—also made of aluminum— are thermally isolated from the rest of the MRA components by a surrounding vacuum. This vacuum barrier minimizes heat conduction and convection from the warmer MRA structure (operating at approximately 32–55°C) to the hydrogen loop, helping maintain the hydrogen temperature at the desired low level of around 20 K.

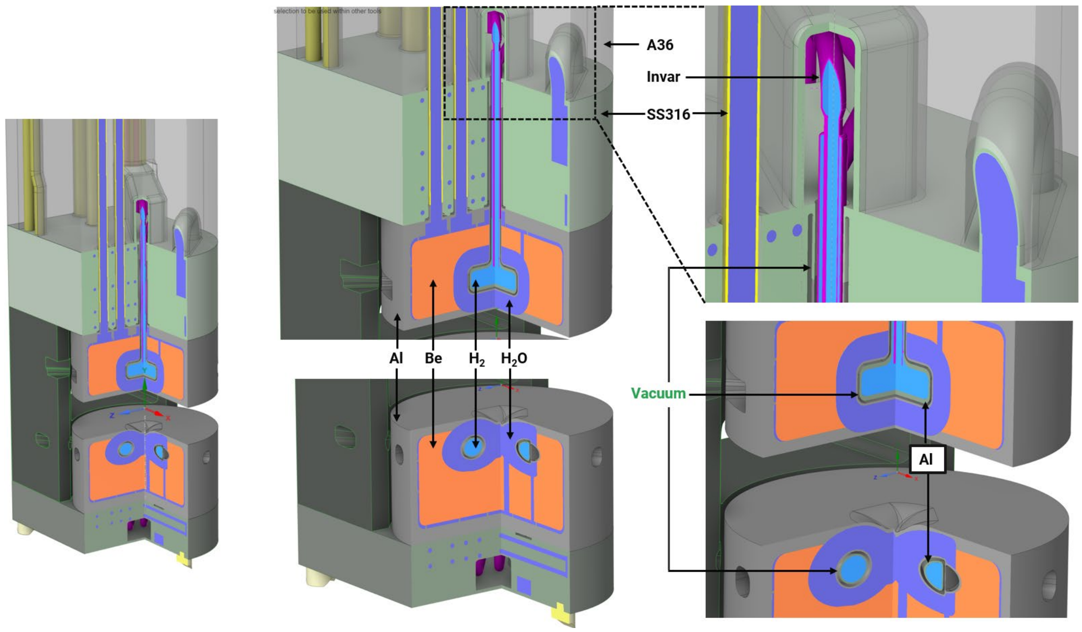

Figure 5. Vacuum region in MRA.

Figure 6 presents the locations of the neutron beam ports. To minimize thermal distortions and ensure precise alignment of these ports within the backbone and the cylindrical (upper) and tube (lower) moderators, the cooling channels in the backbone were specifically adjusted to reduce local temperature gradients.

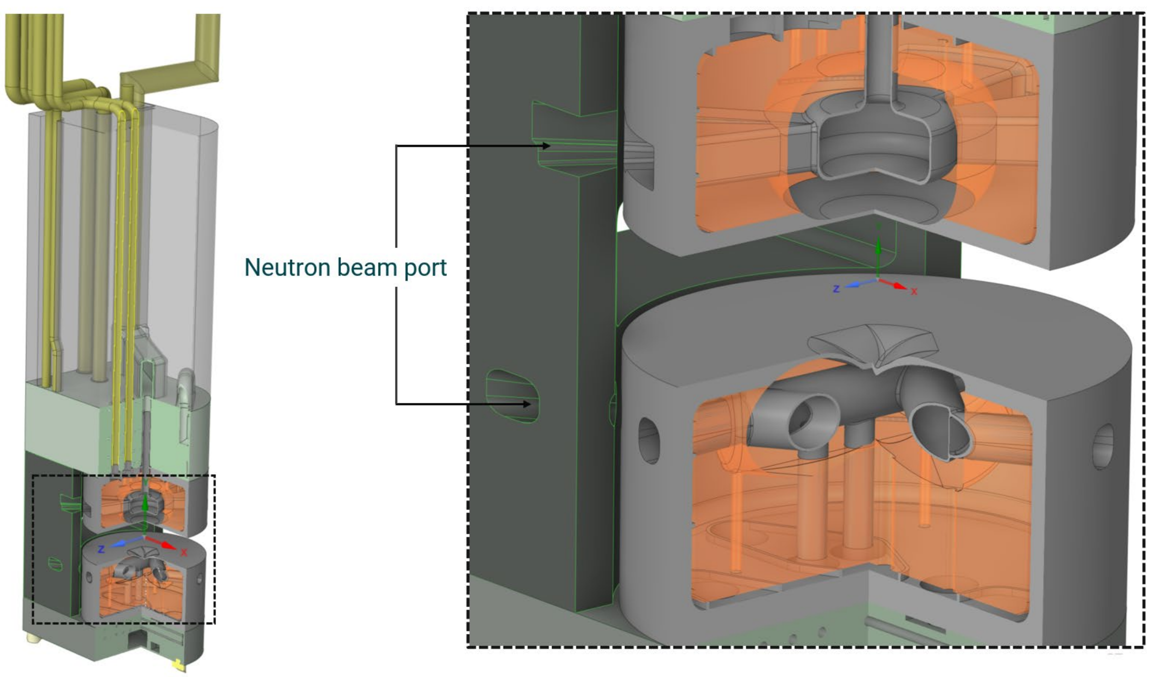

Figure 6. Neutron beam ports in MRA.

The term "reflector" in the Moderator Reflector Assembly (MRA) is used in multiple contexts and may lead to ambiguity. In this report:

- **Beryllium** is referred to as the solid neutron **reflector.**
- The **aluminum** structure enclosing the beryllium is referred to as the **reflector vessel**.
- The **reflector vessel assembly** refers to the integrated system consisting of the **aluminum reflector vessel**, **beryllium reflector**, and **internal water domains**.

In addition, the MRA water forms a single continuous hydraulic system; however, its functional role varies spatially (Figure 5). Water adjacent to the liquid hydrogen moderator (between the moderator and beryllium) is referred to as the **premoderator** water region, as it provides both thermal-hydraulic cooling and neutron moderation prior to the hydrogen moderator.

Water located outside the beryllium is referred to as the **reflector cooling water** region (Figure 5, Figure 8, Figure 9 and Figure 64), where its primary function is heat removal from surrounding structures, including the beryllium reflector and aluminum reflector vessel. Its presence has a minor adverse effect on neutron economy and is therefore treated primarily as a coolant in the design basis.

Figure 7 shows the water-cooled regions and the five cooling loops identified in Figure 4. The inner and outer sections of the upper MRA are cooled by two independent water streams, each operating at a flow rate of 7.5 GPM (0.47 kg/s) and a temperature of 90 °F (32.2 °C). The lower MRA follows a similar cooling configuration with two additional streams. The backbone is cooled by a separate water stream at 15 GPM (0.94 kg/s) and 90 °F (32.2 °C). All five cooling streams enter the MRA independently but eventually merge at the top of the backbone, where they exit the system through a single common outlet. The directions of water flow through the upper MRA, lower MRA, and backbone are shown in Figure 8, Figure 9, and Figure 10, respectively.

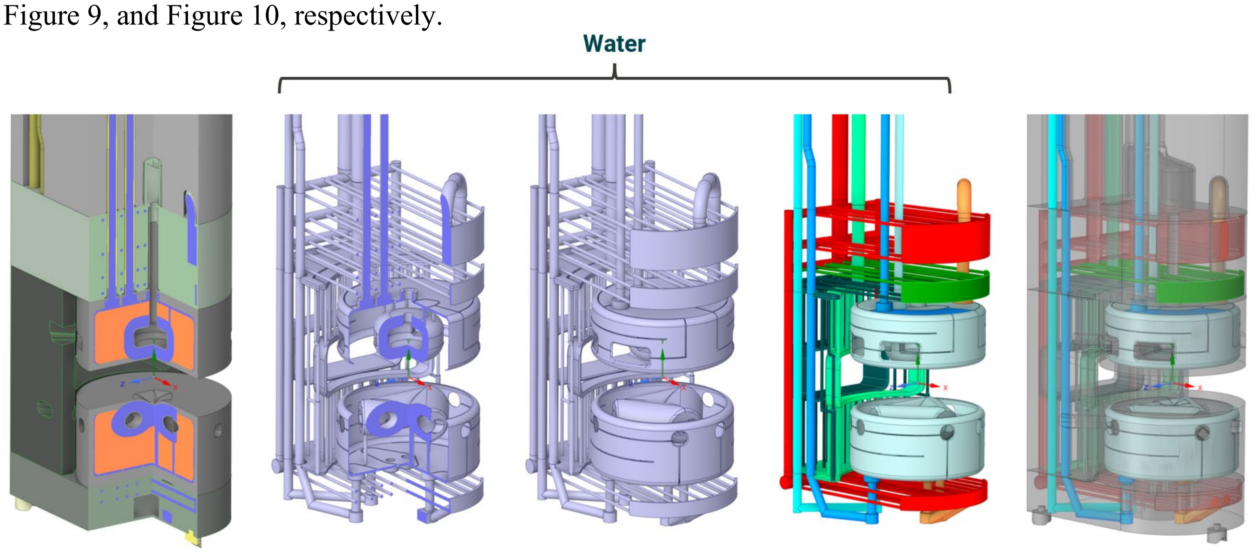

Figure 7. Water region in MRA.

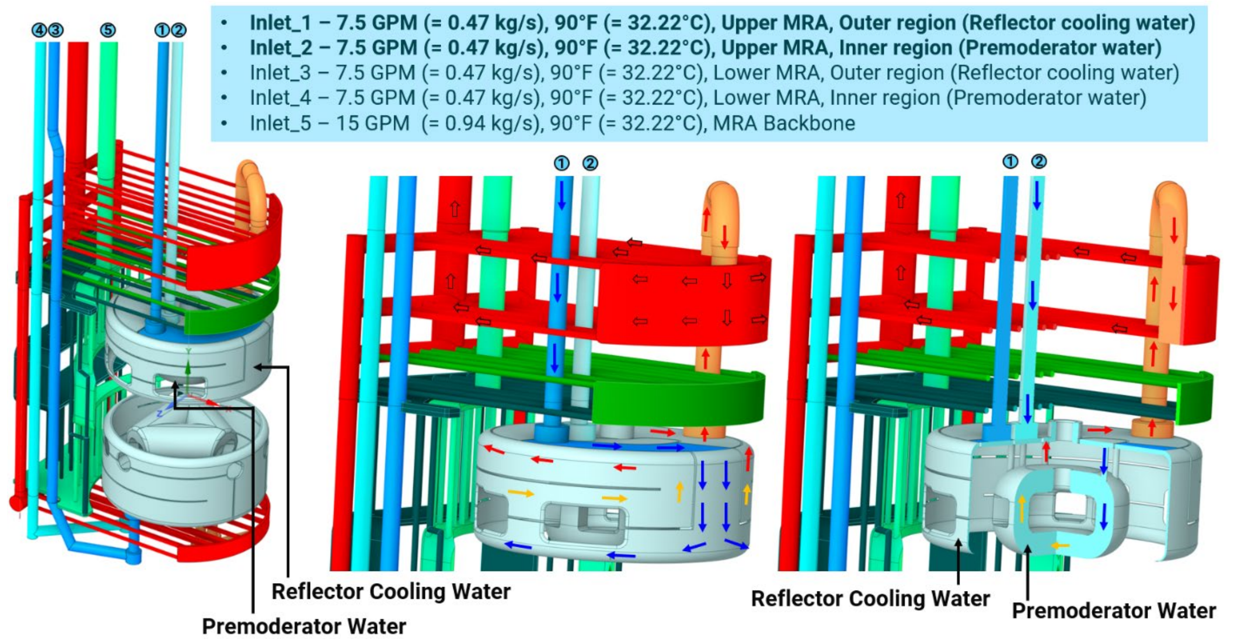

Figure 8. Waer cooling loops in the upper MRA (from inlet_1 and inlet_2).

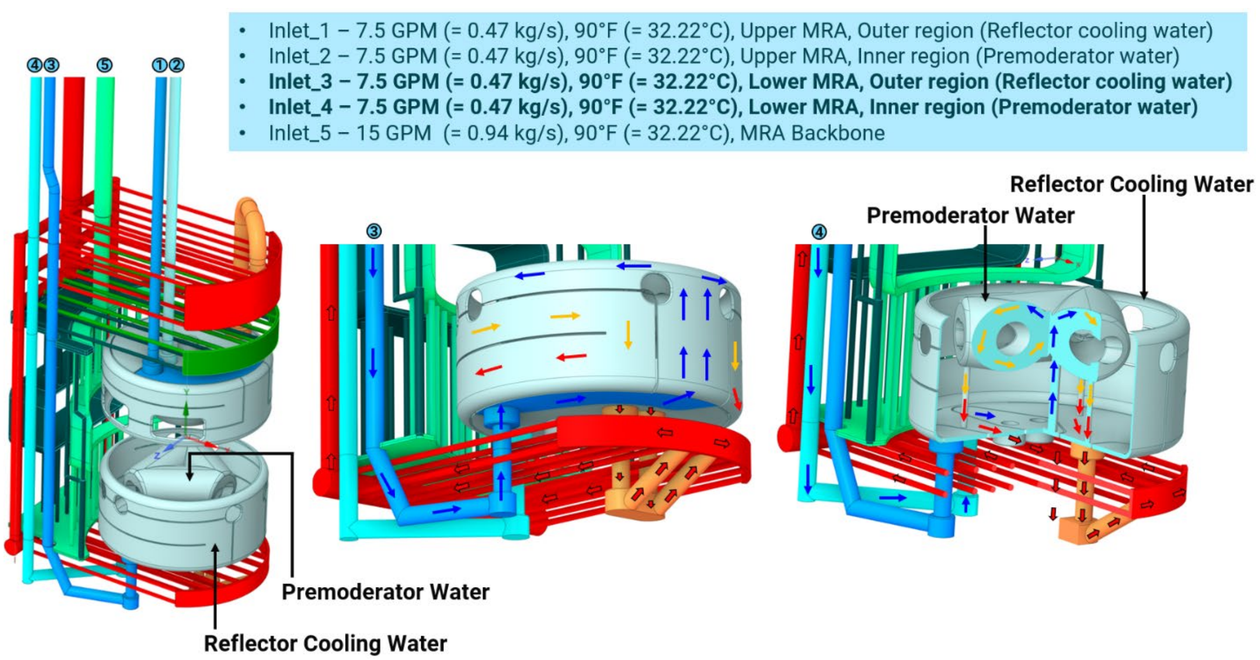

Figure 9. Water cooling loops in the lower MRA (from inlet_3 and inlet_4).

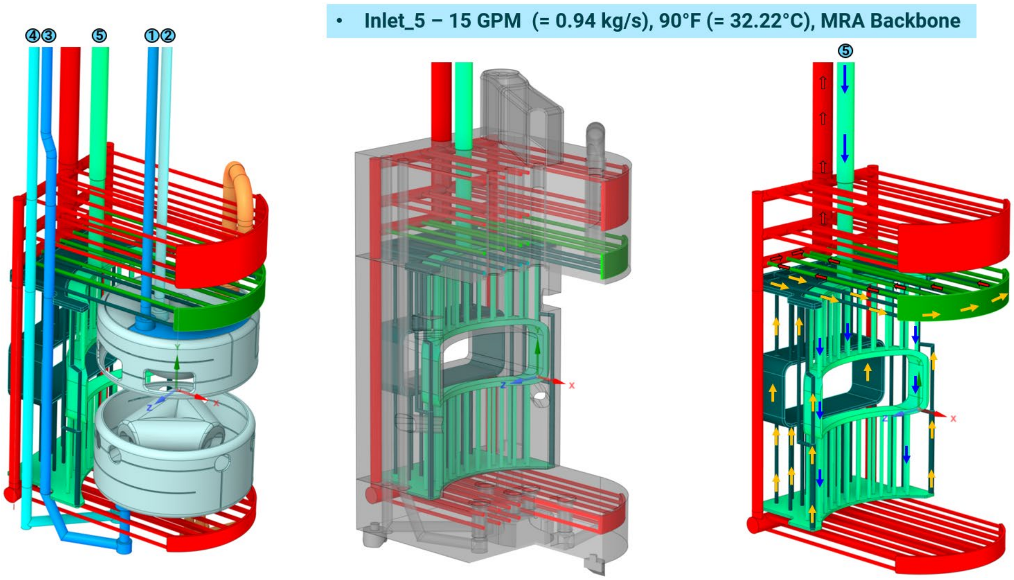

Figure 10. Water cooling loops in the MRA backbone.

Figure 11 shows the overall dimensions of the MRA. The height of the MRA backbone (lower, middle, upper, and shield blocks) is approximately 1.65 m, while the total height of the assembly, including piping, is approximately 4.3 m. The MRA has an overall width of approximately 38 cm and a depth of 53 cm.

The upper and lower reflector vessel assemblies are attached to the backbone and are separated by 100 mm, with the target wheel positioned between them (Figure 1). The inner diameter of the cylindrical moderator is 100 mm, and its height is 30 mm. Similarly, the inner diameter of the tube moderator is 30 mm. The vacuum gap between the moderator and aluminum reflector vessels is approximately 3 mm.

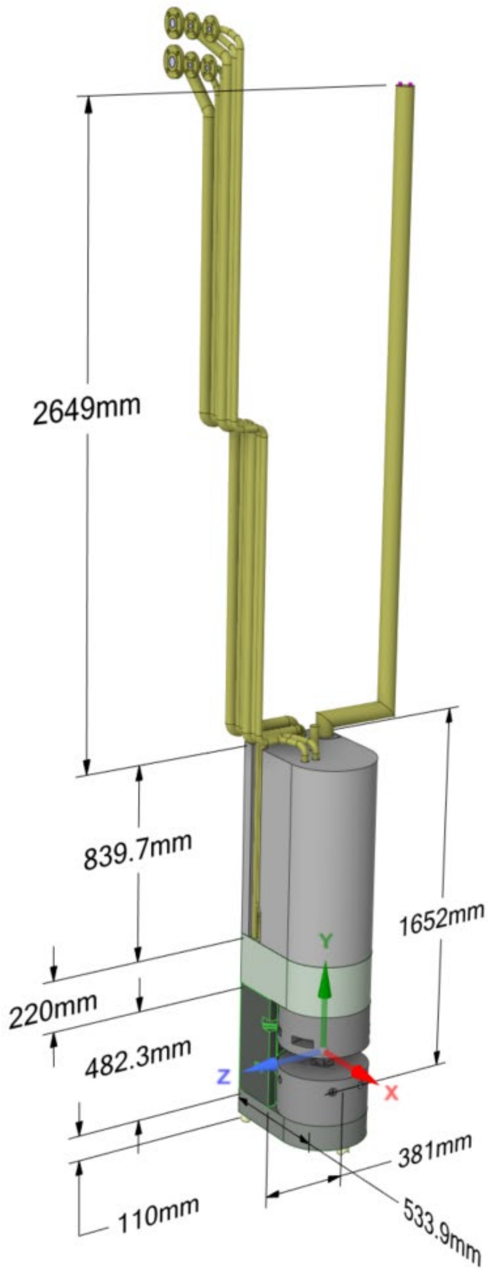

Figure 11. Dimensions of the full MRA assembly.

4. MATERIAL PROPERTY

The thermophysical properties of materials used in all simulations are summarized in Table 2. According to NIST data (https://trc.nist.gov/cryogenics/materials/6061%20Aluminum/6061_T6Aluminum_rev.htm), the thermal conductivity and specific heat capacity of aluminum 6061 vary significantly between 20 K and 300 K (room temperature), as illustrated in Figure 12 and Figure 13, which are based on curve-fitting equations (1) and (2). At 20 K, the thermal conductivity of Al6061 is approximately 5.5 times lower than at room temperature, though it remains higher than that of SS316 stainless steel. Under normal operating conditions, the temperature of the aluminum vessel in the hydrogen loop varies by roughly 5 K around 20 K, while the vessel temperatures in the upper and lower MRA fluctuate by 10–15 °C near room temperature. Given these relatively narrow temperature ranges, constant thermal property values for Al 6061, as listed in Table 2, were used in the simulations.

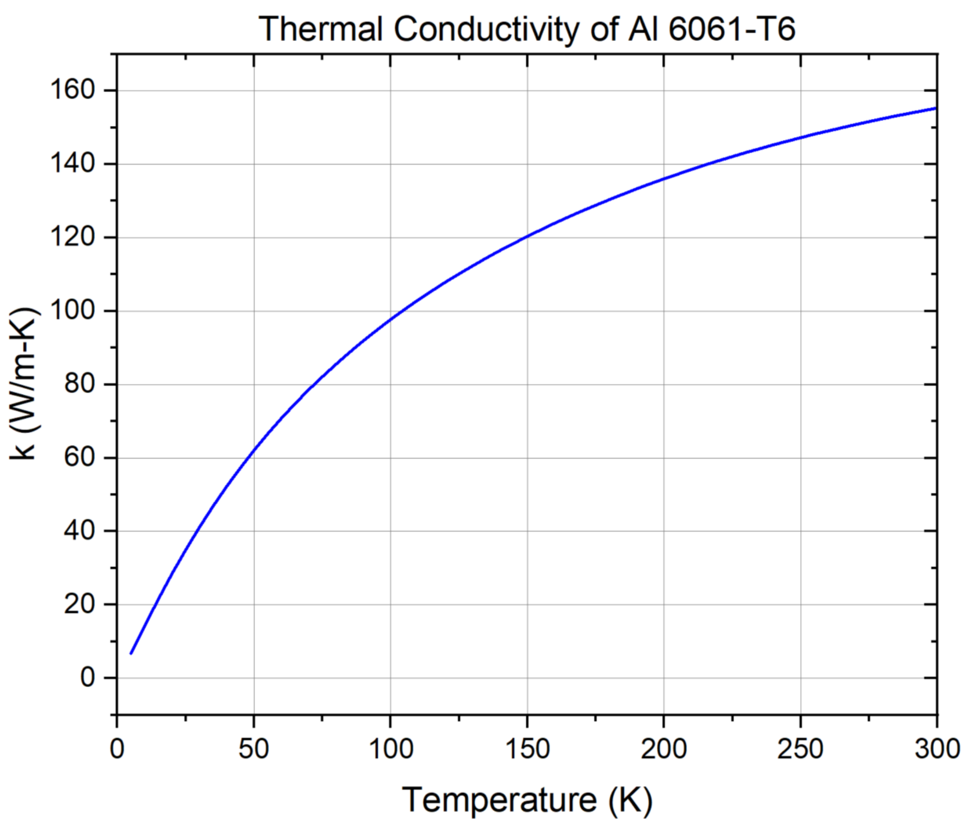

Figure 12. Thermal conductivity of Al 6061-T6 (data from NIST).

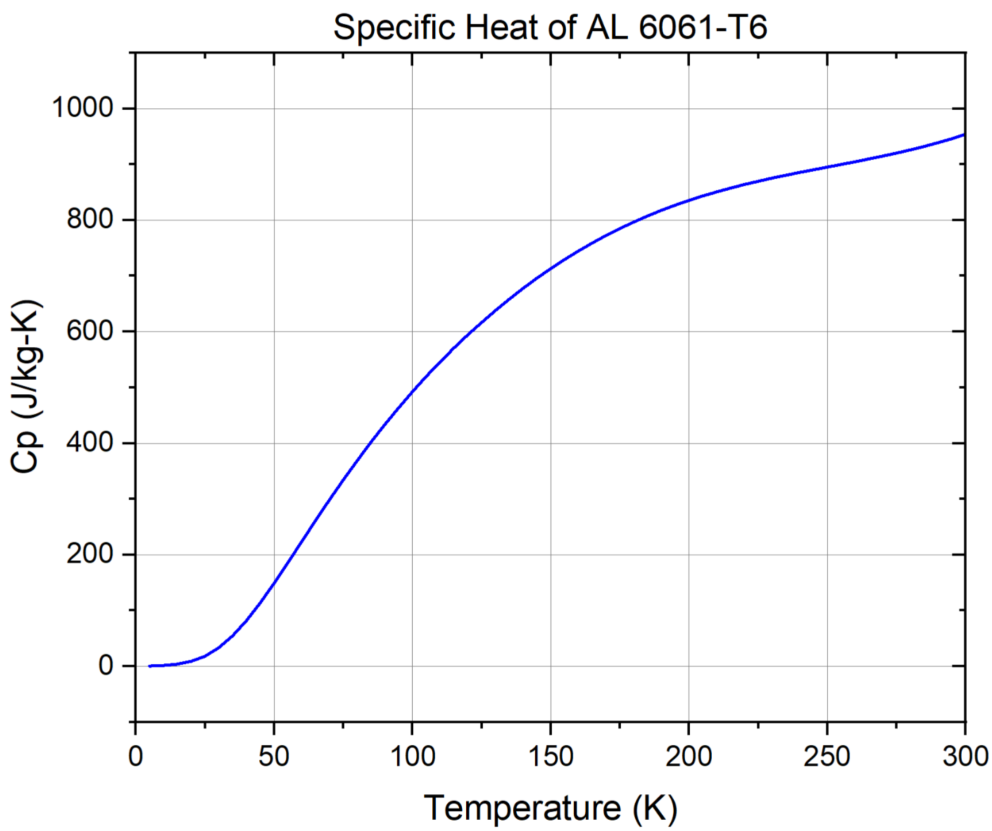

Figure 13. Specific heat of Al 6061-T6 (data from NIST).

For the remaining structural materials, thermophysical properties were obtained from standard engineering databases. Properties for SS316 were taken from the ANSYS material library, while properties for A36 carbon steel were obtained from MakeItFrom.com, and properties for beryllium, Invar, and SS420 stainless steel were obtained from MatWeb. The thermal conductivity of beryllium was assumed to be 168 W/m-K. While literature values for pure beryllium at room temperature are approximately 200 W/m-K, lower values are commonly used in engineering analyses to account for material impurities and microstructural effects; therefore, the selected value (168 W/m-K) provides a conservative estimate for thermal analysis.

Table 2. Material thermophysical properties.

Material	Thermal Conductivity, k (W/m-K)	Density, ρ (kg/m^3)	Specific Heat, Cp (J/kg-K)	Viscosity (Pa-s)
Al 6061 @20K (NIST)	28.43	2713	8.85	N/A
Al 6061 @room T (Ansys)	155.3	2713	915.7	N/A
A36 (Carbon Steel)	50	7850	470	N/A
Be	168	1850	1925	N/A
Invar	10.15	8050	515	N/A
Para H_2 (Liquid)	Table(T)	Polynomial in T	Table(T)	Table(T)
SS 316	14.58	8000	486.1	N/A
SS 420	24.9	7800	460	N/A
H_2O	0.620271	997.561	4181.72	8.89E-04

$$k_{Al}(T) = 10^{a+b(log_{10}T)+c(log_{10}T)^2+d(log_{10}T)^3+e(log_{10}T)^4+f(log_{10}T)^5+g(log_{10}T)^6+h(log_{10}T)^7+i(log_{10}T)^8} \quad (1)$$

$$Cp_{Al}(T) = 10^{a+b(log_{10}T)+c(log_{10}T)^2+d(log_{10}T)^3+e(log_{10}T)^4+f(log_{10}T)^5+g(log_{10}T)^6+h(log_{10}T)^7+i(log_{10}T)^8} \quad (2)$$

$$\rho_{H_2}(T) = a + bT + cT^2 + dT^3 \quad (3)$$

Temperature-dependent properties of para-hydrogen, obtained from NIST, are presented in Table 4. The thermal conductivity, specific heat, and viscosity data listed in Table 4 were incorporated into the CFD simulations of the hydrogen loop. These data tables were imported into STAR-CCM+. Hydrogen density was represented using a polynomial fit, as shown in Equation (3) and Figure 14, and implemented within the simulation. The coefficients for Equations (1), (2), and (3) are summarized in Table 3. Table 5 compares the hydrogen density from NIST with that obtained from the polynomial fit. As shown in Figure 14, during normal operation, the temperature of hydrogen ranges from 18.34 K to 24.5 K, which falls well within the range of the curve-fit function. The inlet condition for the hydrogen loop was set to a volume flow rate of 0.5 L/s and a temperature of 18.34 K, corresponding to an inlet mass flow rate of 0.0373 kg/s. It should be emphasized that the outlet temperature of the hydrogen loop is approximately 21 K. Therefore, the temperature variation of the majority of the hydrogen is within 3 K. Hydrogen at temperatures above 21 K exists only in thin near-wall regions that are in direct contact with aluminum surfaces. Further details will be discussed in Chapter 8.

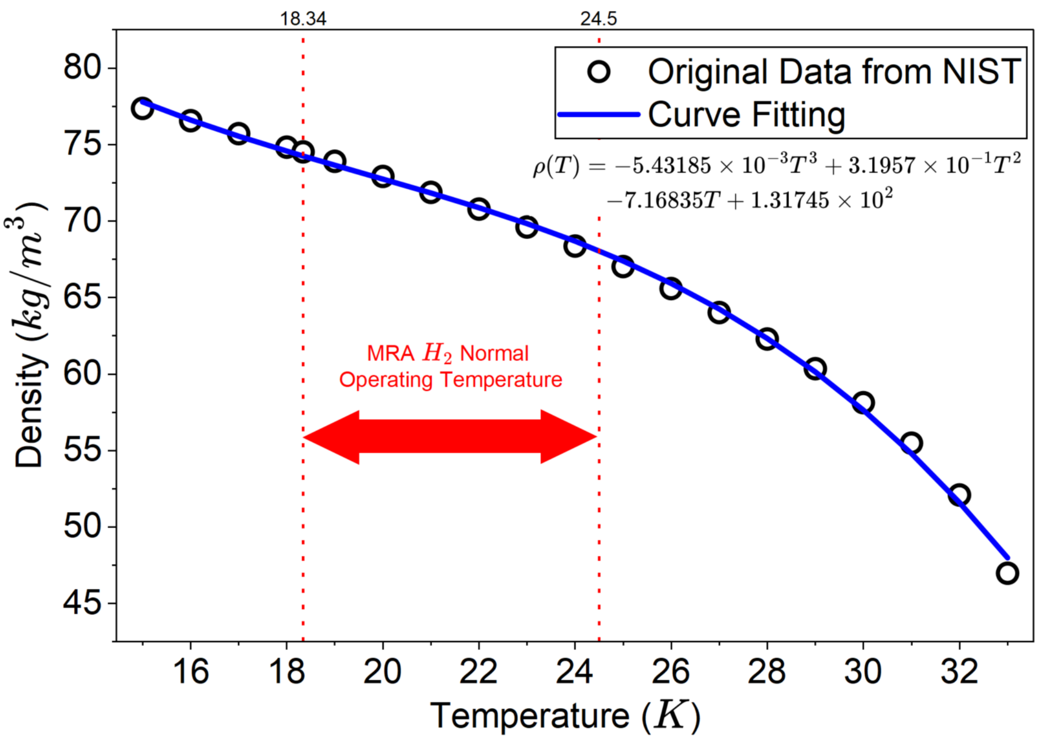

Figure 14. Comparison of hydrogen density from NIST data and polynomial curve-fit function.

Table 3. Coefficient.

Coefficient	ρ_{H_2} (kg/m^3)	k_{Al} (W/m-K)	Cp_{Al} (J/kg-K)
a	138.907	0.07918	46.6467
b	-8.23187	1.0957	-314.292
c	0.370104	-0.07277	866.662
d	-0.00621765	0.08084	-1298.3
e		0.02803	1162.27
f		-0.09464	-637.795
g		0.04179	210.351
h		-0.00571	-38.3094
i		0	2.96344

Table 4. Thermal properties of para-H_2 at 1.45 MPa (14.5 bar) (from NIST).

Temperature (K)	Pressure (MPa)	Density (kg/m3)	Volume (m3/kg)	Internal Energy (kJ/kg)	Enthalpy (kJ/kg)	Entropy (J/g*K)	Cv (J/g*K)	Cp (J/g*K)	Sound Spd. (m/s)	Joule-Thomson (K/MPa)	Viscosity (Pa*s)	Therm. Cond. (W/m*K)	Phase
15.000	1.4500	77.241	0.012946	-48.154	-29.382	-2.6918	5.2775	7.0899	1277.6	-1.5529	2.4601e-05	0.092173	liquid
16.000	1.4500	76.451	0.013080	-41.113	-22.146	-2.2249	5.3273	7.3893	1261.2	-1.4699	2.2056e-05	0.095267	liquid
17.000	1.4500	75.618	0.013224	-33.762	-14.587	-1.7667	5.3864	7.7374	1244.7	-1.3801	1.9938e-05	0.097931	liquid
18.000	1.4500	74.738	0.013380	-26.058	-6.6569	-1.3136	5.4585	8.1293	1226.8	-1.2869	1.8140e-05	0.10016	liquid
19.000	1.4500	73.806	0.013549	-17.961	1.6851	-0.86267	5.5415	8.5610	1206.8	-1.1922	1.6595e-05	0.10197	liquid
20.000	1.4500	72.820	0.013733	-9.4346	10.478	-0.41178	5.6311	9.0301	1184.5	-1.0969	1.5250e-05	0.10334	liquid
21.000	1.4500	71.775	0.013932	-0.44422	19.758	0.040913	5.7227	9.5370	1160.1	-1.0008	1.4069e-05	0.10430	liquid
22.000	1.4500	70.665	0.014151	9.0459	29.565	0.49705	5.8123	10.085	1133.5	-0.90325	1.3020e-05	0.10484	liquid
23.000	1.4500	69.483	0.014392	19.076	39.944	0.95832	5.8974	10.682	1104.9	-0.80288	1.2081e-05	0.10498	liquid
24.000	1.4500	68.220	0.014659	29.695	50.950	1.4266	5.9763	11.340	1073.9	-0.69779	1.1232e-05	0.10471	liquid
25.000	1.4500	66.862	0.014956	40.964	62.651	1.9042	6.0484	12.078	1040.6	-0.58545	1.0454e-05	0.10405	liquid
26.000	1.4500	65.393	0.015292	52.968	75.141	2.3939	6.1136	12.925	1004.5	-0.46250	9.7355e-06	0.10301	liquid
27.000	1.4500	63.789	0.015677	65.820	88.551	2.8999	6.1729	13.926	965.25	-0.32430	9.0613e-06	0.10164	liquid
28.000	1.4500	62.015	0.016125	79.687	103.07	3.4277	6.2284	15.155	921.99	-0.16406	8.4190e-06	0.099862	liquid
29.000	1.4500	60.021	0.016661	94.820	118.98	3.9859	6.2833	16.742	873.63	0.028890	7.7952e-06	0.097672	liquid
30.000	1.4500	57.719	0.017325	111.63	136.76	4.5883	6.3446	18.948	818.36	0.27297	7.1732e-06	0.095018	liquid
31.000	1.4500	54.952	0.018198	130.89	157.27	5.2609	6.4264	22.384	752.91	0.60440	6.5284e-06	0.091797	liquid
32.000	1.4500	51.357	0.019472	154.29	182.52	6.0618	6.5662	28.974	670.52	1.1108	5.8131e-06	0.087785	liquid
33.000	1.4500	45.670	0.021896	187.70	219.45	7.1966	6.9155	50.428	552.16	2.1104	4.8772e-06	0.082744	supercritical
34.000	1.4500	26.227	0.038129	290.76	346.04	10.961	8.2878	154.04	393.52	5.7891	2.7995e-06	0.072017	supercritical
35.000	1.4500	18.615	0.053721	344.62	422.52	13.185	7.5856	45.216	417.49	6.7857	2.3764e-06	0.050051	supercritical
36.000	1.4500	16.043	0.062333	368.49	458.87	14.210	7.1967	30.303	436.27	6.7671	2.3032e-06	0.045324	supercritical
37.000	1.4500	14.475	0.069086	385.70	485.87	14.950	6.9661	24.392	451.59	6.5915	2.2854e-06	0.043362	supercritical
38.000	1.4500	13.346	0.074928	399.88	508.52	15.554	6.8168	21.189	464.92	6.3739	2.2889e-06	0.042386	supercritical
39.000	1.4500	12.466	0.080217	412.32	528.64	16.077	6.7152	19.171	476.92	6.1480	2.3033e-06	0.041886	supercritical
40.000	1.4500	11.747	0.085129	423.64	547.07	16.544	6.6434	17.781	487.97	5.9262	2.3239e-06	0.041658	supercritical

Table 5. Comparison of hydrogen density from NIST tabulated data and polynomial curve-fit Function used in simulations.

	Original Data from NIST	**Curve Fitting**	
Temperature (K)	**Density (kg/m^3)**	**Density (kg/m^3)**	**Error (%)**
15	77.365	77.791	-0.43
16	76.564	76.612	-0.05
17	75.723	75.552	0.17
18	74.839	74.577	0.26
18.34	**74.528**	**74.259**	**0.27**
19	73.907	73.654	0.25
20	72.925	72.751	0.17
21	71.886	71.836	0.05
22	70.786	70.875	-0.09
23	69.618	69.836	-0.22
24	68.371	68.687	-0.32
25	67.035	67.395	-0.36
26	65.593	65.927	-0.33
27	64.024	64.251	-0.23
28	62.295	62.334	-0.04
29	60.359	60.144	0.22
30	58.138	57.648	0.49
31	55.491	54.813	0.68
32	52.106	51.607	0.50
33	46.986	47.997	-1.01

5. SUMMARY OF HEAT LOAD[2]

The volumetric heat sources used in all simulations in this report were obtained from MCNP calculations conducted by the STS neutronics team (Report: S03040000-DAC10010). The heat loads in the MRA components are summarized in Table 6. The total heat deposited in the hydrogen loop is 884 W. The combined heat deposited in the shield block, backbone, lower, and upper MRA is 57.2 kW. Overall, the 700 kW proton beam deposits approximately 8.29% of its total power—about 58 kW—into the Moderator Reflector Assembly.

Table 6. Summary of heat load in MRA.

	Component	Heat (W)		Total Heat (W)
MRA Moderator (H_2 Loop)	Upper Al Vessel (Cylindrical)	188.58	409.50	884.41
	Lower Al Vessel (Tube)	220.92		
	Upper Hydrogen (Cylindrical)	183.95	419.51	
	Lower Hydrogen (Tube)	235.56		
	Invar		55.39	
MRA Non- H_2 Loop (Reflectors, Shield Block, and Backbone)	Upper Al Vessel (Cylindrical)	4354.10	8946.56	57194.97
	Lower Al Vessel (Tube)	4592.46		
	Upper Beryllium	6006.45	12320.05	
	Lower Beryllium	6313.60		
	A36 Shield Block		798.72	
	SS316 Pipes	28.91	25915.75	
	SS316 Upper Block	7725.11		
	SS316 Middle Block	12525.80		
	SS316 Lower Block	5635.93		
	SS420		11.01	
	Water		9202.89	
	Sum			**58079.38**

[2] Heat source files used in CFD analysis:
https://ornl.sharepoint.com/sites/sts/targetsystems/Shared%20Documents/Forms/AllItems.aspx?id=%2Fsites%2Fsts%2Ftargetsystems%2FShared%20Documents%2FS%2E03%2E02%20Target%20Assembly%2F99%5FSANDBOX%2FKAO%2F2026%2FSTS%5FMRA%2F0%5FMRA%5FFDR&viewid=9be9bc88%2D5a13%2D48c7%2D9fff%2Dd22f94ffdeb5
CFD_Heat_Sources.zip

6. MESH CONFIGURATION

STAR-CCM+ provides three types of volume meshers: polyhedral, tetrahedral, and trimmed cell meshers. Compared to tetrahedral cells, polyhedral cells typically have around ten neighboring cells, which enables better gradient estimation. Furthermore, polyhedral meshes require approximately four times fewer cells, use half the memory, and need only one-fifth to one-tenth of the computing time to achieve the same order of accuracy as tetrahedral meshes (Simcenter STAR-CCM+ 2019.2 User Guide, 2019). Therefore, polyhedral meshes are adopted for this study.

For turbulence modeling with wall treatment methods, two general approaches are available: low y^+ and high y^+ treatments. These approaches solve one or more equations to model near-wall turbulence quantities such as wall shear stress, turbulent production, and dissipation rates. All simulations in this report employ the two-layer all y^+ wall treatment in STAR-CCM+. This hybrid method combines the high y^+ treatment (where the near-wall cell lies within the logarithmic region of the boundary layer, $y^+ > 30$), the low y^+ treatment (where the viscous sublayer is well resolved, $y^+ < 1$), and provides reasonable solutions in the buffer region ($1 < y^+ < 30$).

The mesh configurations for the Moderator Reflector Assembly (MRA) are shown in Figure 15–Figure 17. Eight prism layers are used at the water and hydrogen boundaries to resolve the fluid boundary layers near walls. As shown in Figure 18 and Figure 19, the wall y^+ values across the MRA are mostly kept below 5 to ensure that the wall treatment method is applied appropriately. The mesh settings for individual materials are summarized in Table 7. Overall, approximately 81 million cells are used to mesh the MRA domain. The mesh independence study for the MRA is discussed in APPENDIX A. MESH INDEPENDENCE STUDY.

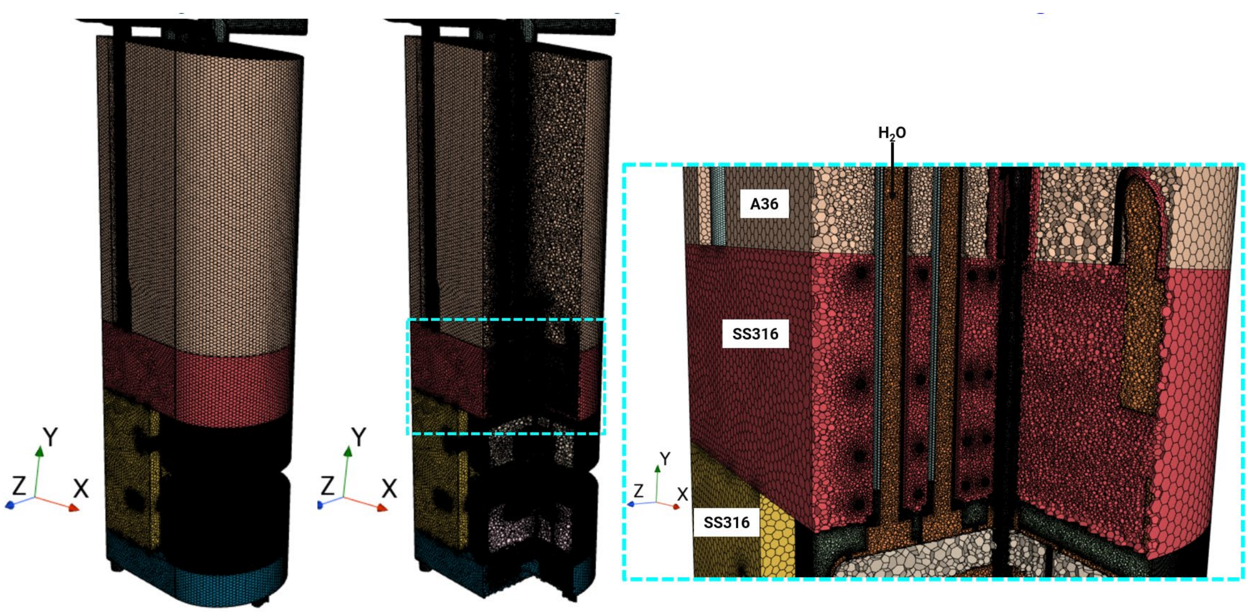

Figure 15. MRA mesh configuration 1.

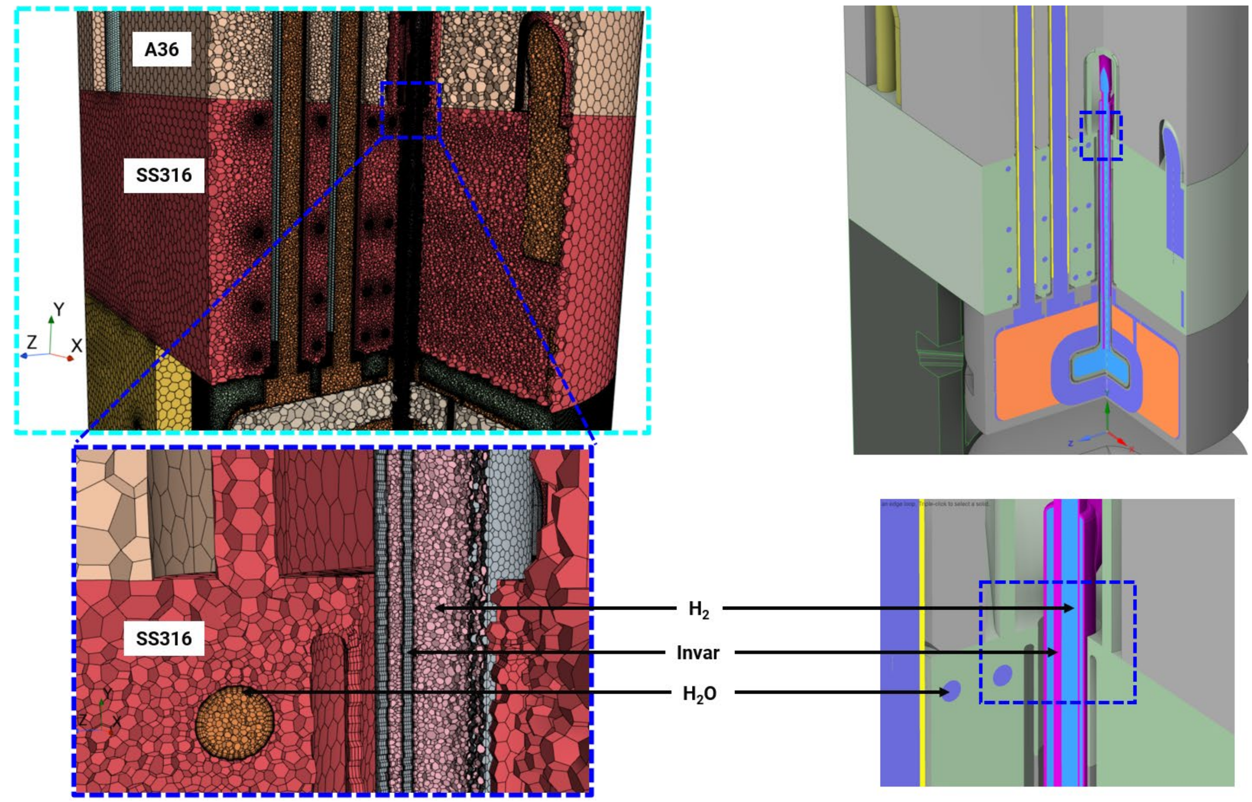

Figure 16. MRA mesh configuration 2.

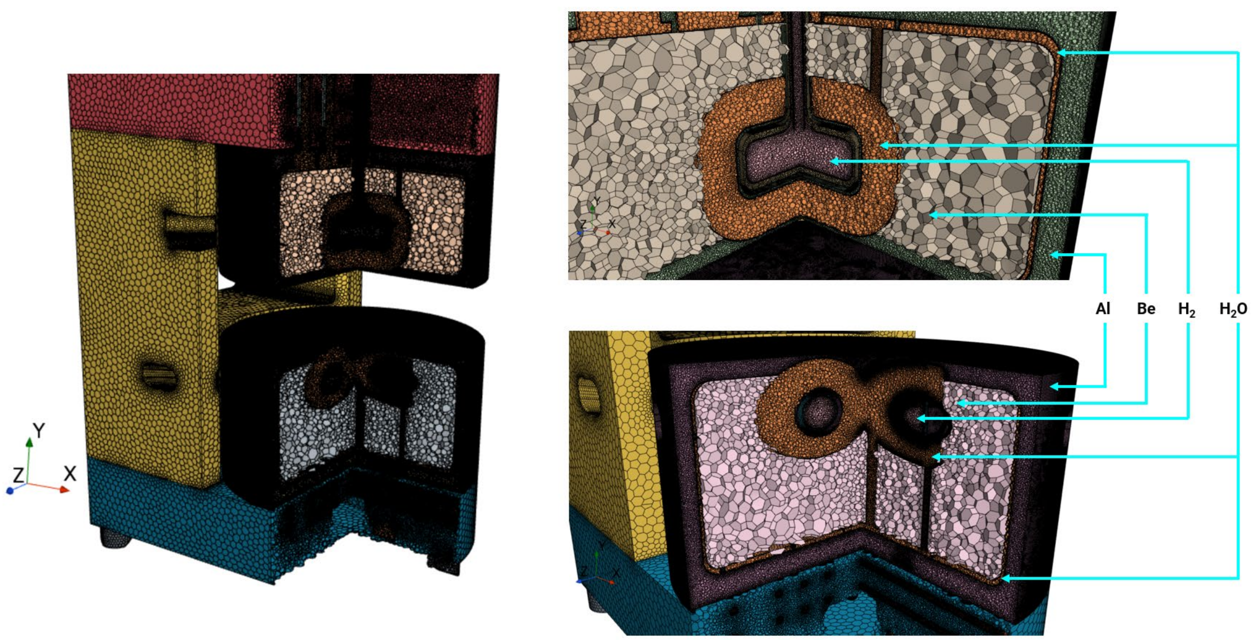

Figure 17. MRA mesh configuration 3.

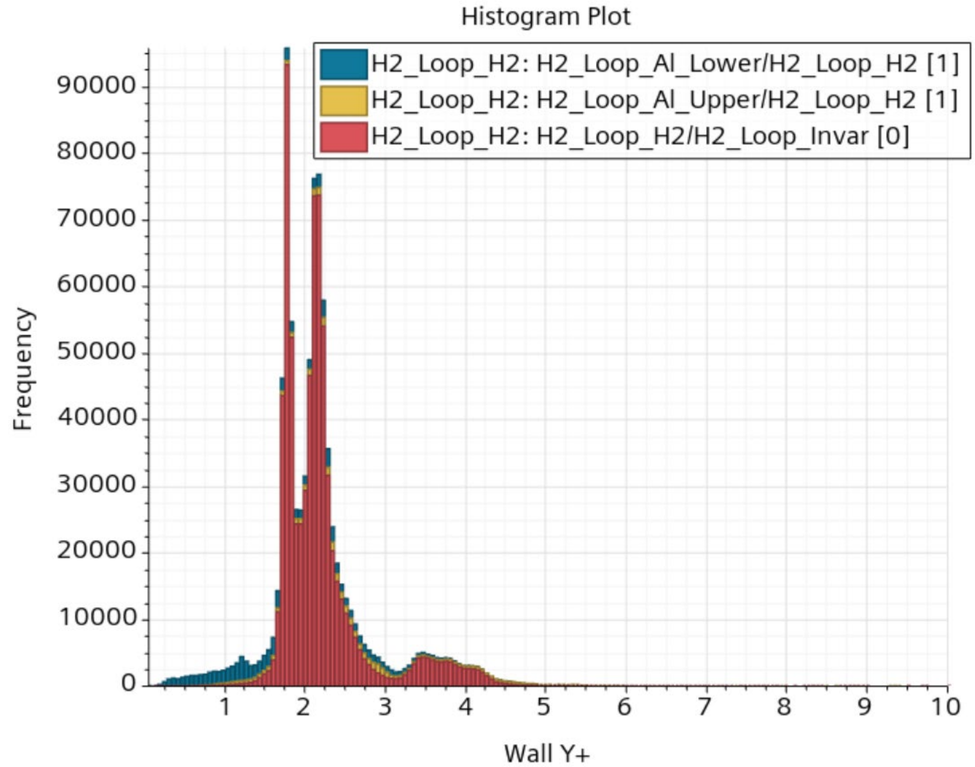

Figure 18. Wall Y+ of the hydrogen loop.

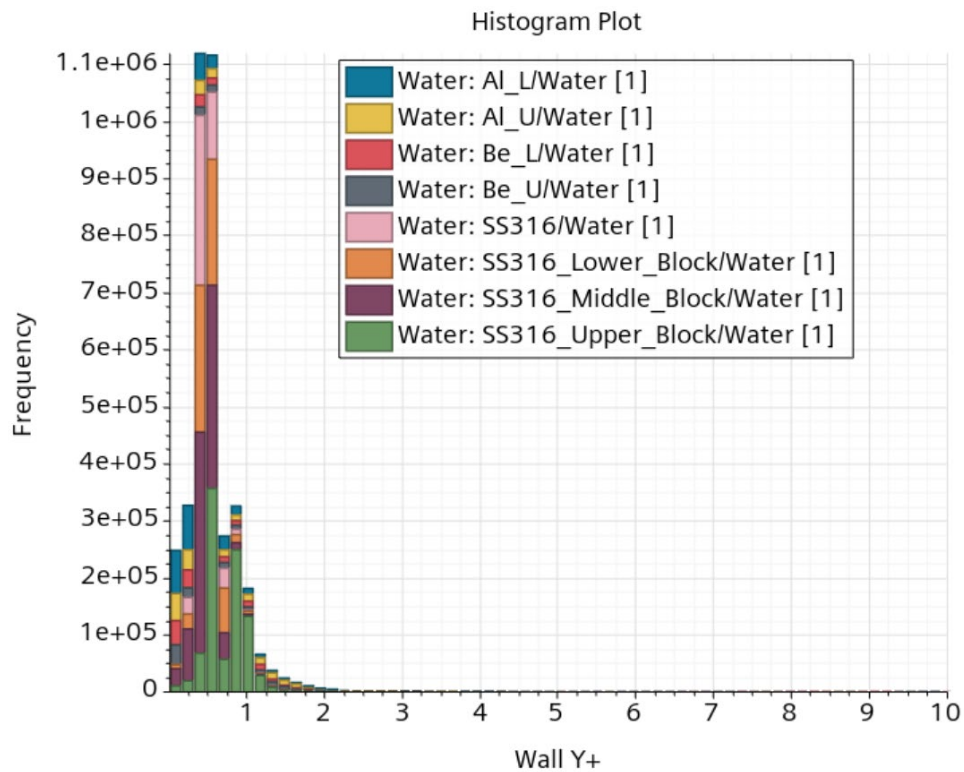

Figure 19. Wall Y+ of MRA (excluding the hydrogen loop).

Table 7. Mesh configuration of MRA.

MRA (with H_2 Loop included)						
	Al	**Be**	**H_2**	**Water**	**Invar**	**SS**
Mesh Type	Polyhedral mesh	Polyhedral mesh	Polyhedral mesh	Polyhedral mesh	Polyhedral mesh	Polyhedral mesh
Base Size (m)	0.0025	0.05	0.0025	0.0025	0.0025	0.01
Target Surface Size (m)	9.00E-04	2.50E-02	9.00E-04	2.50E-03	9.00E-04	1.00E-02
Minimum Surface Size (m)	2.50E-04	5.00E-03	2.50E-04	2.50E-04	2.50E-04	1.00E-03
Volume Growth Rate	1.2	1.2	1.2	1.2	1.2	1.1
Number of Prism Layers	4	N/A	8	8	N/A	N/A
Prism Layer Stretching	1.5	N/A	1.5	1.5	N/A	N/A
PrismLayerTotalThickness(m)	2.50E-04	N/A	3.50E-04	6.25E-04	N/A	N/A
Number of Thin Layers	N/A	N/A	N/A	N/A	5	5
Number of Cells	**2.56E+07**	**3.77E+04**	**8.83E+06**	**3.58E+07**	**3.58E+06**	**7.34E+06**
Total Cells	**8.12E+07**					

7. SOLVER AND BOUNDARY CONDITIONS

In the Moderator Reflector Assembly (MRA), the moderator hydrogen loop (liquid hydrogen and Al vessels) is thermally isolated from the reflector vessel assemblies (Al vessels, Be reflectors, and water domains) by a surrounding vacuum. Therefore, the CFD analysis of the full MRA is divided into two parts: one for the hydrogen loop—including the cylindrical (upper) hydrogen moderator, tube (lower) hydrogen moderator, Invar tubes, and aluminum hydrogen vessels—and another for the remaining MRA components, including the upper and lower reflector vessel assemblies (water, beryllium, and aluminum vessel), the backbone (SS316), the shield block (A36 carbon steel), and the kinetic mounts (SS420). The solvers and boundary conditions for these two separate simulations are summarized in Table 8 and Table 9, respectively (MRA-CMS Interface Sheet S01020500-IST10148 and MRA-Process Systems Interface Sheet S01020500-IST10186).

Since the MRA operates within the CV environment (rough vacuum or helium mode), all heat loads are assumed to be removed by the internal cooling circuits (liquid hydrogen and water coolant). Accordingly, adiabatic boundary conditions are applied to all external surfaces of the MRA and its alignment features.

Because the MRA backbone and aluminum reflector vessels are equipped with independent water-cooling systems, the thermal contact resistance between them is assumed to be negligible (i.e., perfect thermal contact) in the CFD analysis. This assumption is justified by earlier design iterations, in which these components were analyzed in separate CFD simulations to establish adequate cooling performance for each subsystem. Therefore, the influence of interfacial thermal resistance on the overall thermal response is expected to be minimal.

The shield, upper, middle, and lower blocks of the MRA backbone are assumed to be in perfect contact, with zero thermal resistance between them. The impact of thermal resistance on peak temperature is expected to be less than 4°C, based on the analysis performed using an earlier MRA model developed for the Preliminary Design Review (PDR). Since then, the cooling performance of the MRA backbone has been improved. The effect of inter-block thermal resistance in the PDR design is discussed in APPDNDIX B. IMPACT OF THERMAL CONTACT RESISTANCE.

The reference pressures listed in Table 8 and Table 9 are applied at the outlet boundaries in the simulations. Since no phase change is expected under normal operating conditions, a single-phase model is used for both analyses. In STAR-CCM+, the reference pressure is used to evaluate the pressure drop corresponding to the specified inlet mass flow rates. Therefore, for single-phase simulations, the absolute value of the reference pressure at the outlet is not critical; it serves only as a baseline for pressure drop calculations and does not affect the simulation results, even if a different reference value is used.

Table 8. Solvers and boundary conditions for the moderator (hydrogen loop).

Fluid	Hydrogen
Time model	Steady state
Flow and energy model	Segregated solver
Turbulence model	Realizable k-ε two-layer
Wall treatment	Two-layer all y+
Inlet mass flow rate	0.0373 kg/s
Inlet temperature	18.34 K
Reference pressure	14.5 bar

Table 9. Solvers and boundary conditions for the MRA (excluding the hydrogen loop).

Fluid	Water
Time model	Steady state
Flow and energy model	Segregated solver
Turbulence model	Realizable k-ε two-layer
Wall treatment	Two-layer all y+
Inlet mass flow rate	inlets 1- 4: 0.47 kg/s (7.5 GPM); inlet 5: 0.94 kg/s (15 GPM)
Inlet temperature	32.22°C (90°F)
Reference pressure	2.5 bar

8. RESULTS OF NORMAL OPERATION

8.1 MODERATOR (HYDROGEN LOOP)

8.1.1 Heat Source Distribution

For the hydrogen loop, the heat source distributions in the aluminum vessel, hydrogen, and Invar tubes are shown in Figure 20, Figure 21, and Figure 22, respectively. The total heat deposited in the aluminum vessel is 409.5 W, with 188.58 W in the upper aluminum vessel (cylindrical moderator) and 220.92 W in the lower aluminum vessel (tube moderator). As indicated in Figure 20, the energy deposition in aluminum vessels peaks towards their rear side with respect to the proton beam due most probably to the increased absorption of thermal and epithermal neutrons generated in the rear portions of the tungsten target.

In contrast, the heat source in the hydrogen peaks in the front region, upstream of the proton beam, as shown in Figure 21. The total heat deposited in the hydrogen is 419.51 W, with 183.95 W in the upper region (cylindrical moderator) and 235.56 W in the lower region (tube moderator). The total heat deposited in the Invar tube is 55W.

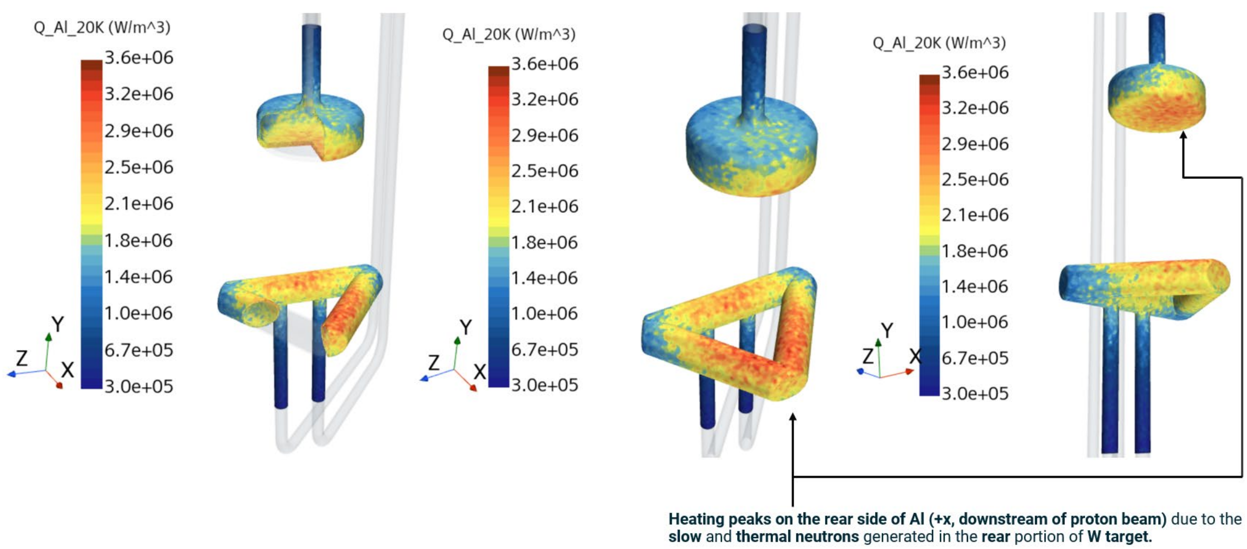

Figure 20. Volumetric heat source distribution in the aluminum vessel of the hydrogen loop.

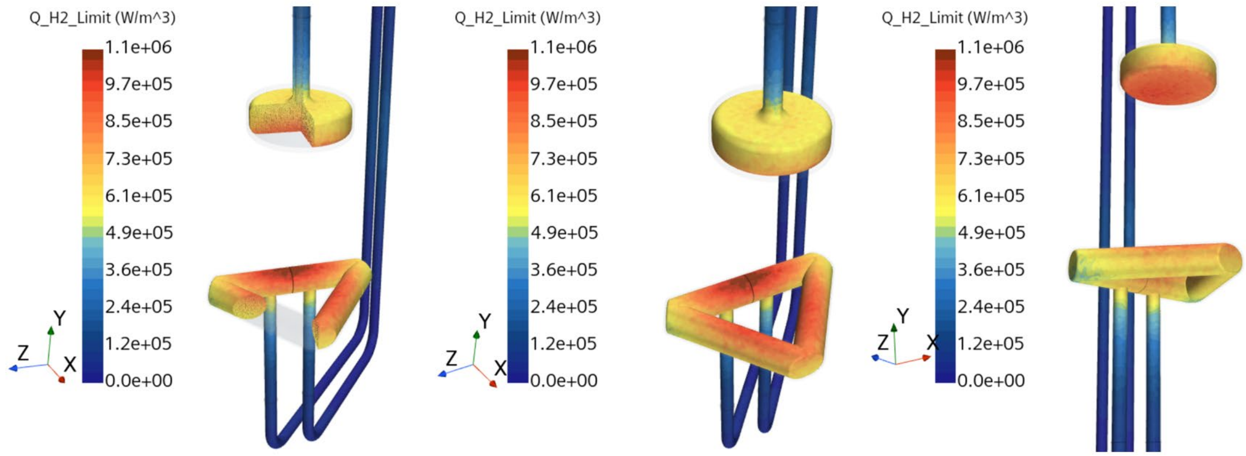

Figure 21. Volumetric heat source distribution in the hydrogen of the hydrogen loop.

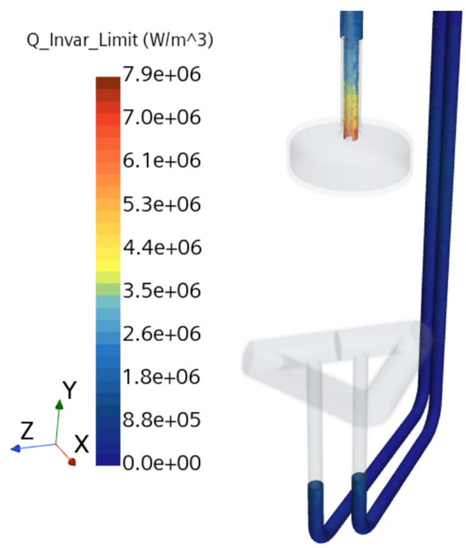

Figure 22. Volumetric heat source distribution in the Ivar tubes of the hydrogen loop.

8.1.2 Pressure Distribution

The pressure distribution in the hydrogen loop is shown in Figure 23. A reference pressure of 14.5 bar is set at the outlet, and hydrogen enters from the top at a mass flow rate of 0.0373 kg/s (0.5 L/s), flows downward through the cylindrical and tube aluminum vessels, and then returns upward to the outlet. Under these conditions, the total pressure drop of the hydrogen loop is 1.52 psi (0.105 bar), which satisfies the design requirement of 0.15 bar.

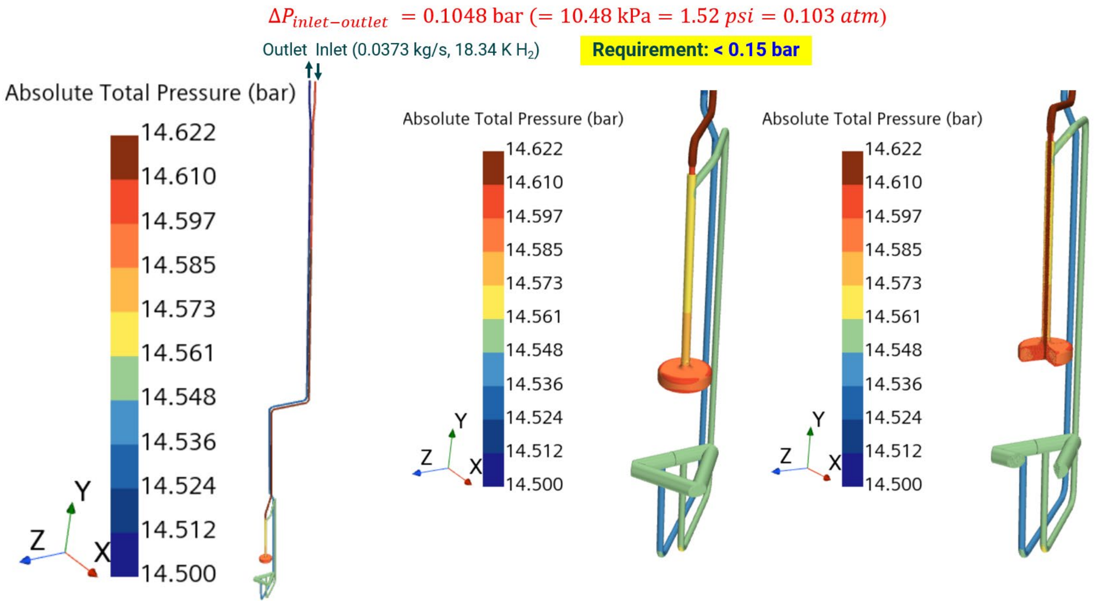

Figure 23. Pressure distribution in hydrogen of the hydrogen loop.

8.1.3 Temperature Distribution

The temperature distribution in the aluminum vessel of the hydrogen loop is shown in Figure 24 and Figure 25. As indicated in these figures, with a more uniform velocity as shown in Figure 32, the temperature of the cylindrical (upper) Al vessel is more uniform with temperature peaks at 23.1 K in the rear portion due to higher energy deposition as shown in Figure 20. In contrast, due to a non-uniform velocity profile and formation of vortex as shown in Figure 33, the temperature field is much more non-uniform in the tube (lower) Al vessel and peaks at 24.6 K at one of the triangular corners where the velocity is significantly reduce due to the vortices.

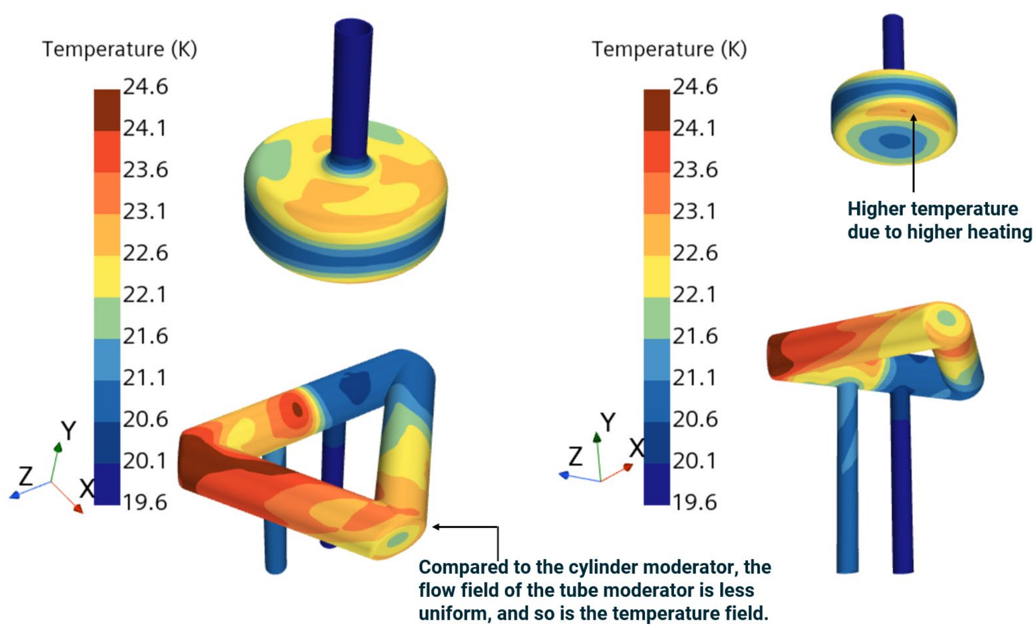

Figure 24. Temperature distribution in the aluminum vessel of the hydrogen loop.

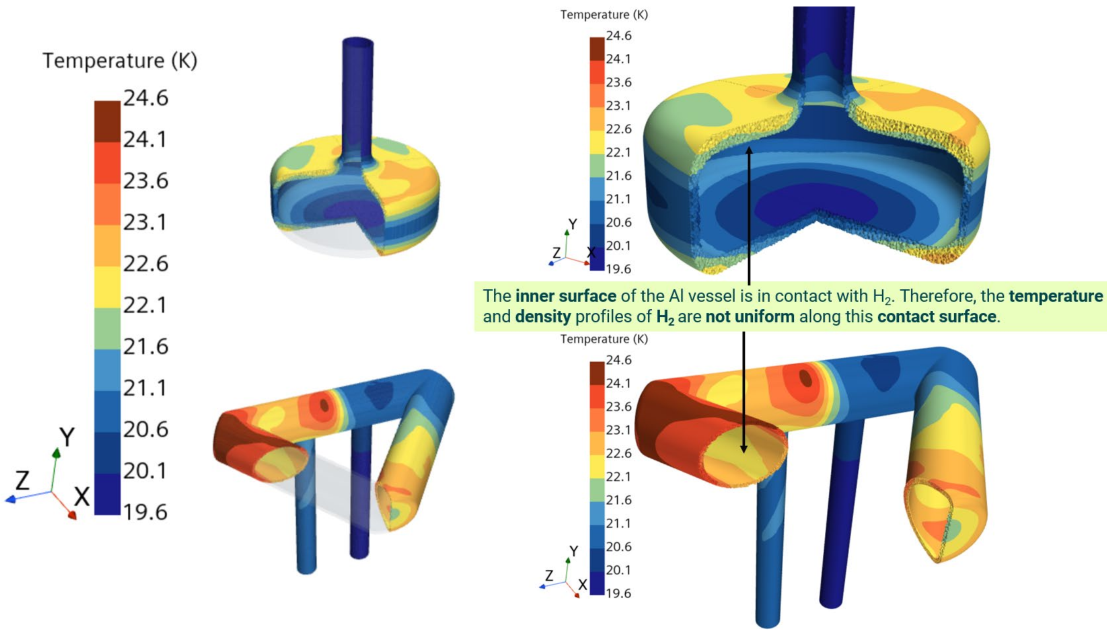

Figure 25. Section view of the temperature profile of the hydrogen loop aluminum vessel.

The hydrogen temperature distribution in the hydrogen loop is shown in Figure 26, Figure 27, and Figure 28. With a mass flow rate of 0.0373 kg/s (0.5 L/s), liquid hydrogen enters the loop from the top at a temperature of 18.34 K and flows sequentially through the upper and lower sections. As it flows through the loop, the hydrogen absorbs energy deposited directly in the fluid as well as heat transferred from the aluminum vessels, and exits the loop at a temperature of 21.021 K. As shown in the section views of the model in Figure 27 and Figure 28, the hydrogen temperature profile is largely uniform, ranging from approximately 18.3 K to 20.8 K. The temperature at the interface between the hydrogen and the aluminum vessel is non-uniform and can reach up to 24.5 K. This elevated hydrogen temperature occurs only within a very thin layer near the contact region between the aluminum vessel and the hydrogen. The average hydrogen temperature in the cylindrical moderator is 19.23 K, while that in the tube moderator is 20.43 K (corresponding to the regions shown in Figure 31).

The critical temperature is defined as the highest temperature at which a liquid phase can exist, regardless of system pressure. The critical temperature of para-hydrogen is approximately 33 K. When operating above the critical temperature, hydrogen becomes supercritical, and its density decreases significantly while becoming highly sensitive to temperature. Even small temperature changes can cause large density fluctuations, leading to unstable moderator performance. Cold neutron production relies on a high hydrogen number density to enable multiple elastic scattering events. In the supercritical regime, the effective hydrogen density is much lower, resulting in fewer scattering events to slow neutrons to cold energies and, consequently, degraded cold neutron brightness.

Near the critical point (~33 K), the thermal properties such as specific heat, thermal expansion coefficient, and compressibility vary rapidly with temperature. These drastic changes in thermal properties can result in thermo-hydraulic instability, leading to local hot spots and flow transients that make accurate prediction of the temperature field more difficult. Therefore, the design requires the maximum hydrogen temperature to remain below 32K. As shown in Figure 26, the peak hydrogen temperature is 24.5 K and occurs only in a thin region near the aluminum wall, providing a margin of approximately 8 K below the critical temperature. As discussed in Section 8.1.7, the temperature rise per pulse for both moderators is approximately 0.08 K, further confirming that STS MRA operates safely well below the critical point.

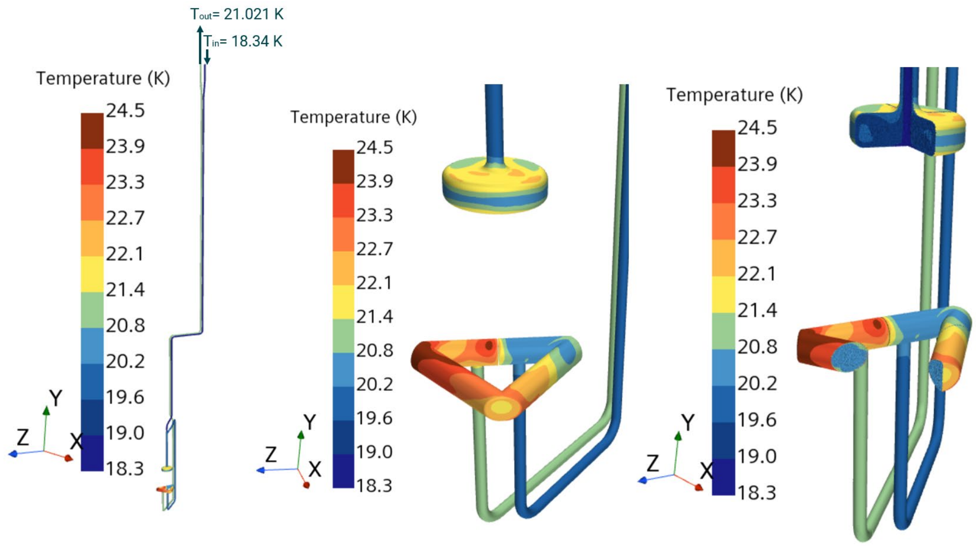

Figure 26. Temperature distribution in hydrogen of the hydrogen loop.

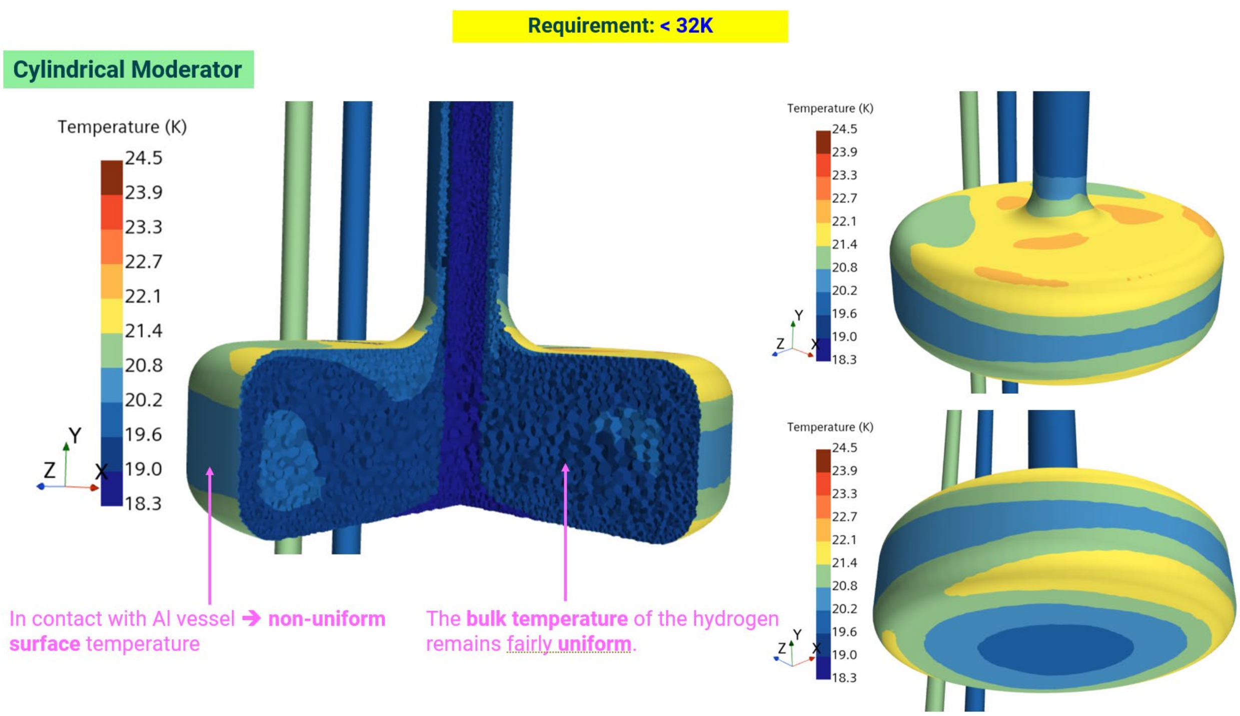

Figure 27. Section view of the hydrogen temperature in the cylindrical (upper) moderator.

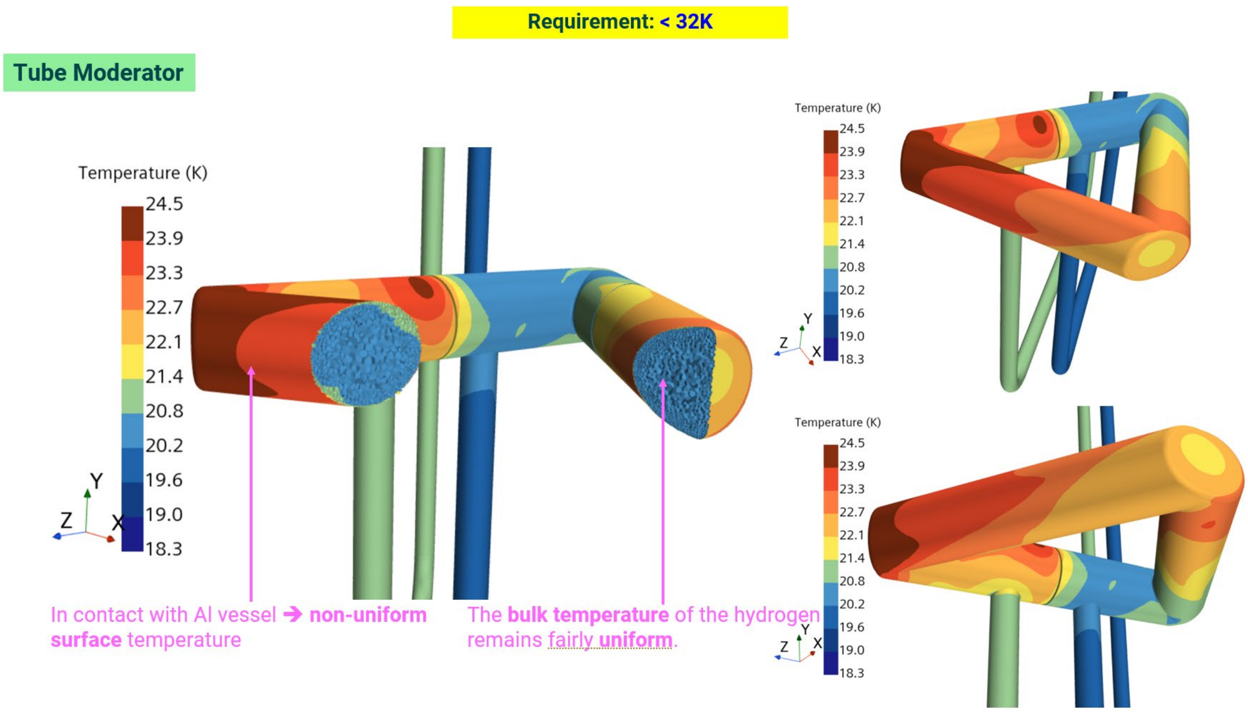

Figure 28. Section view of the hydrogen temperature.

8.1.4 Density Distribution in Hydrogen

The hydrogen density distributions in the moderators are shown in Figure 29, Figure 30, and Figure 31. As shown in Figure 14, a temperature-dependent density correlation has been implemented in the CFD simulations; therefore, the density distributions closely follow the temperature distributions discussed in the previous section. The bulk fluid regions exhibit relatively uniform hydrogen density, with an average value of 72.883 kg/m³, which supports stable cold neutron production performance. As shown in Figure 31, the average hydrogen densities are 73.185 kg/m³ and 72.353 kg/m³ for the cylindrical and tube moderators, respectively. Compared with the inlet density of 74.26 kg/m³ at an inlet temperature of 18.34 K, these values correspond to density reductions of 1.45% for the cylindrical moderator and 2.57% for the tube moderator.

The minimum hydrogen density decreases to 70.6 kg/m³ in the cylindrical moderator and 68.0 kg/m³ in the tube moderator due to the thin heated regions near the aluminum vessel walls. For neutronics analyses, hydrogen densities of 73.1 kg/m³ for the cylindrical moderator and 72.1 kg/m³ for the tube moderator are used in MCNP calculations by the STS neutronics team. These values are in close agreement with the CFD results. The STS neutronics team also performed a hydrogen density sensitivity study and concluded that the neutronic performance is relatively insensitive to hydrogen density variations between 68 kg/m³ and 74 kg/m³, with a maximum change in performance of approximately 0.5% per 2 kg/m³ change in hydrogen density. Together, these results confirm that the STS MRA operates under conditions that ensure stable neutron production.

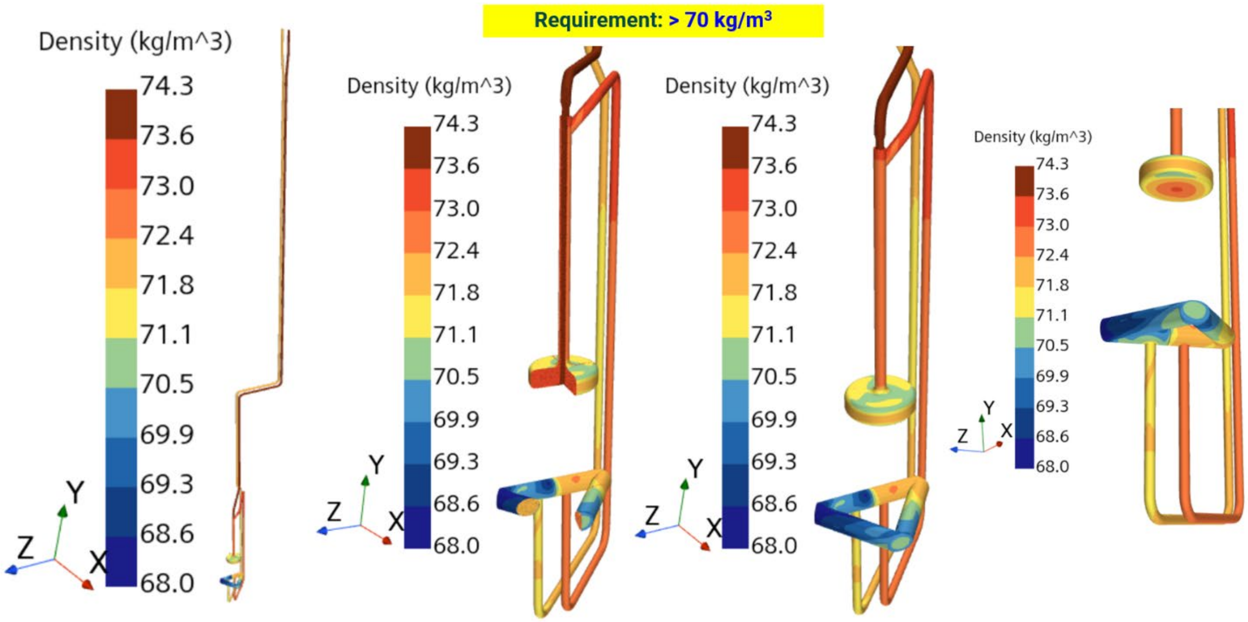

Figure 29. Hydrogen density distribution in the MRA.

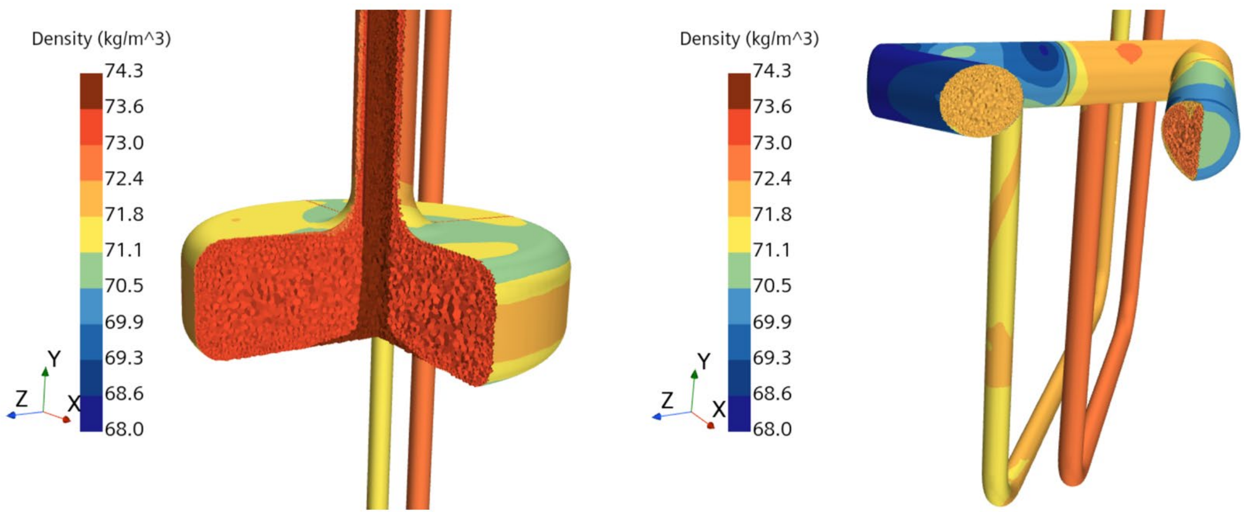

Figure 30. Section view of the hydrogen density distribution.

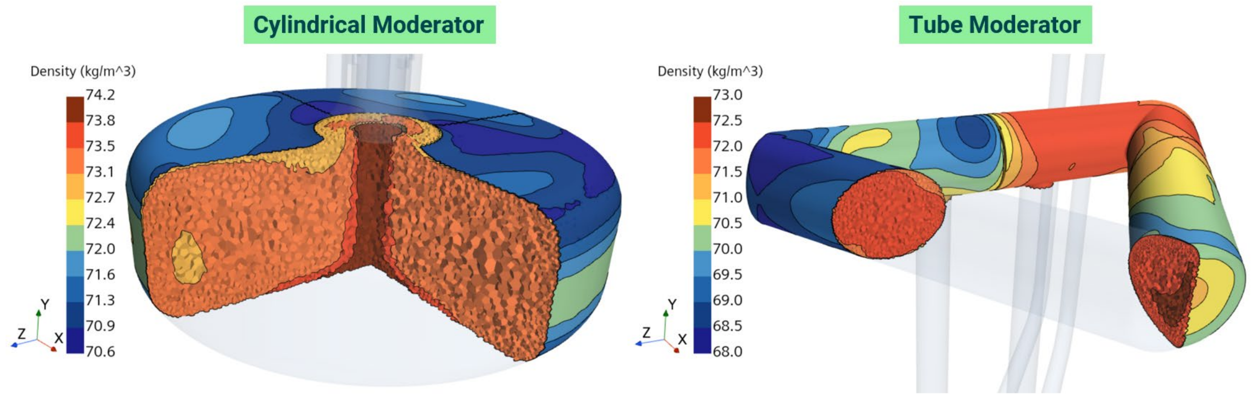

Figure 31. Hydrogen density distribution in the cylindrical and tube moderators.

8.1.5 Streamlines

The streamlines of hydrogen in the cylindrical and tube moderators are shown in Figure 32 and Figure 33, respectively. For the cylindrical (upper) moderator, liquid hydrogen flows downward through a central pipe, fills the cylindrical volume, and then returns through the outer anulus. As shown in Figure 34, the liquid hydrogen accelerates to up to 8.2 m/s when passing through the small gaps in the outer shell. The hydrogen exiting the anulus side of the cylindrical moderator continues flowing downward to the triangular tube (lower) moderator.

In contrast to the cylindrical moderator, hydrogen makes three turns while flowing through the triangular pipes in the tube moderator, resulting in swirling flow and vortex formation, which leads to a highly non-uniform streamline profile. Figure 35 and Figure 36 present the density profile along with the streamlines in the cylindrical and tube moderators, respectively. It should be noted that the density ranges shown in these figures depend on the number of streamlines plotted and do not represent the density in the near-wall region, as shown in Figure 31. Increasing or decreasing the number of streamlines changes the displayed density range.

As shown in Figure 35, denser liquid hydrogen, with a density of 74 kg/m^3, enters the cylindrical moderator. After absorbing the heat in the cylindrical moderator, the density decreases to approximately 72.8 kg/m^3 and then continues flowing downward into the tube moderator. Within the tube moderator, the hydrogen density further decreases to 71.4 kg/m^3 after additional heat absorption.

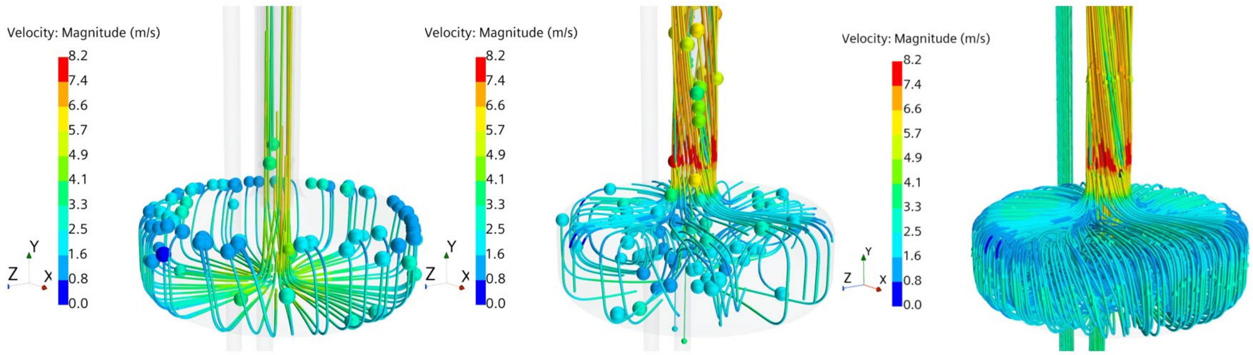

Figure 32. Streamlines of hydrogen in the cylindrical moderator.

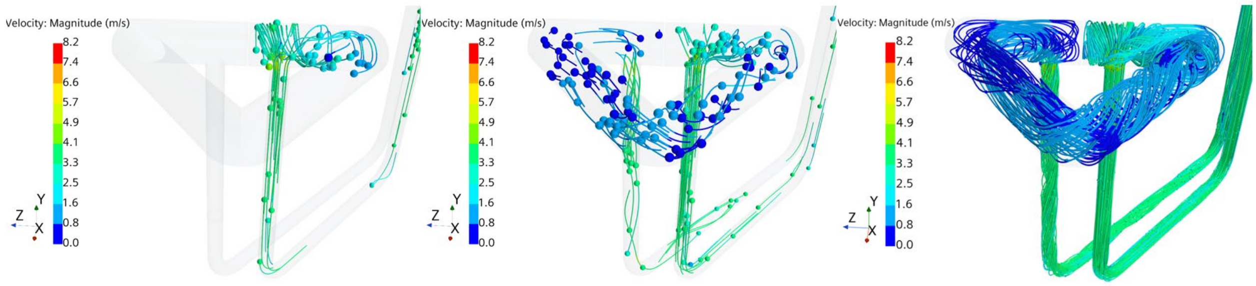

Figure 33. Streamlines of hydrogen in the tube moderator.

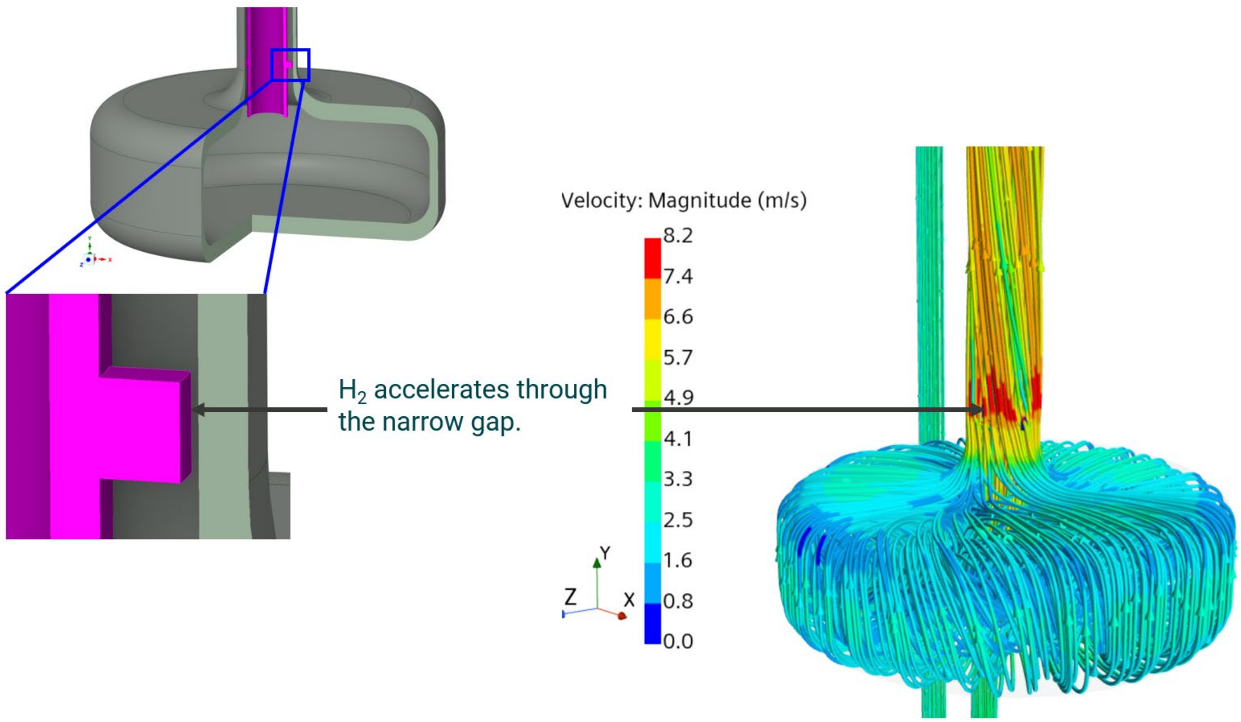

Figure 34. High speed region in the cylindrical moderator.

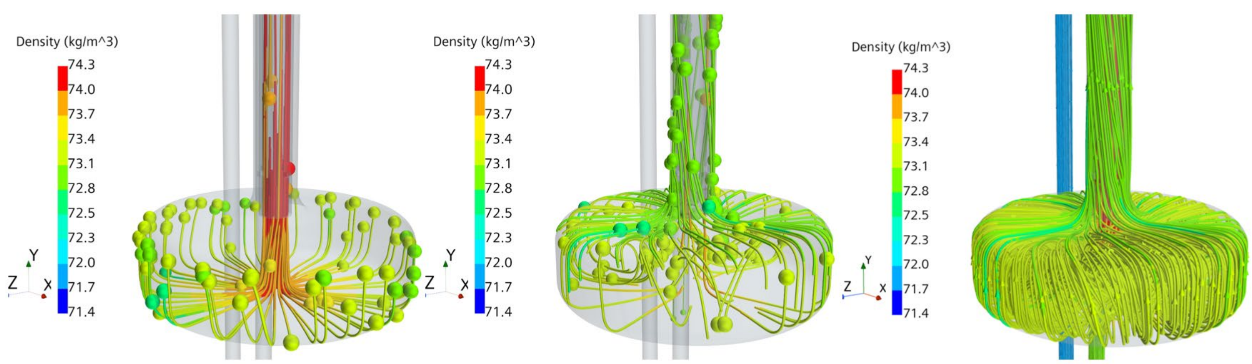

Figure 35. Density distribution in the cylindrical moderator.

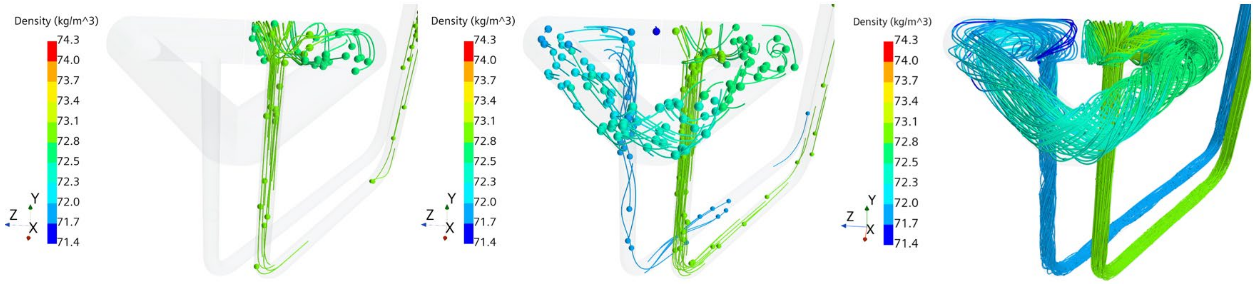

Figure 36. Density distribution in the tube moderator.

8.1.6 Velocity Distribution

The velocity distributions in the cylindrical and tube moderators are shown in Figure 37. The impinging jet enters the cylindrical moderator at a relatively high velocity (~7 m/s), impacts the bottom of the cylinder, forms vortices near the cylinder wall, and then returns upward. These vortices near the cylinder wall correspond to the higher residence times shown in Figure 40. Except for the impinging jet, the velocity within the cylindrical moderator is relatively uniform, ranging from approximately 0.8 m/s to 2.5 m/s. In contrast, due to the vortex formation in the tube moderator, the velocity within the triangular tubes ranges from 0.5 m/s to 4.1 m/s.

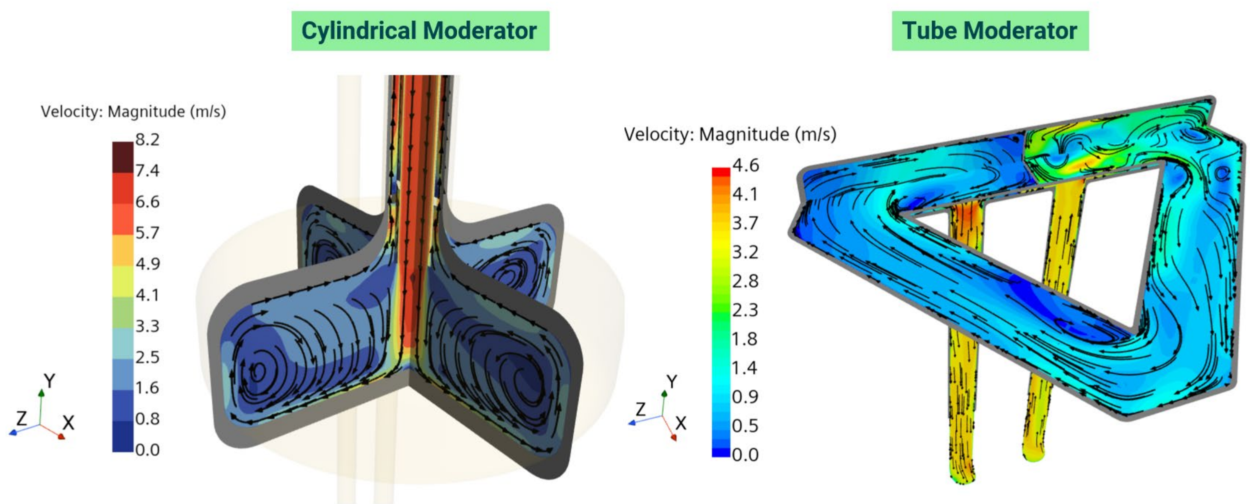

Figure 37. Velocity distribution in the cylindrical and tube moderators.

Figure 38 shows the heat source in the aluminum vessel, the streamlines in the tube (lower) moderator, and the temperature profile of the aluminum vessel. As shown in Figure 38, the peak temperature of 24.6 K in the aluminum vessel occurs at a corner of the triangular tubes, where the velocity is below 0.8 m/s due to vortex formation, rather than at the location of peak heating.

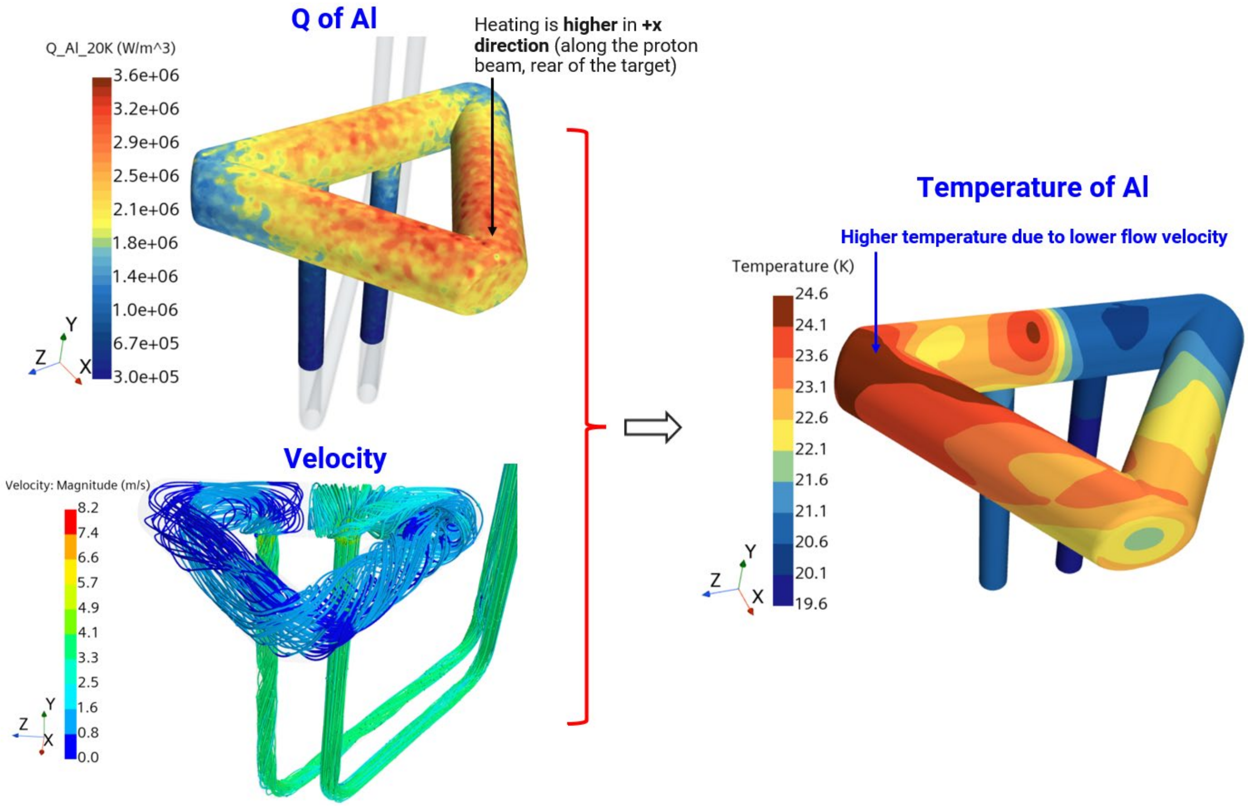

Figure 38. Heat source, streamline, and the temperature profile of tube moderator Al vessel.

8.1.7 Residence Time

The Second Target Station (STS) at ORNL operates with short proton pulses of approximately 1 microsecond (~1 µs). The neutron moderation time from fast to cold energies is on the order of 10–100 µs, while the pulse repetition period is 0.067 s (15 Hz). In contrast, the residence time of liquid hydrogen in the moderators is on the order of 0.1–1 s for the regions directly exposed to the pulsed beam. Since neutron moderation occurs orders of magnitude faster than the hydrogen residence time, the residence time does not affect the conversion of neutrons to cold energies within a single pulse. Instead, cold neutron brightness depends strongly on hydrogen density, the para/ortho hydrogen ratio, and temperature uniformity. Each proton pulse deposits energy in the liquid hydrogen (via neutrons and gamma rays), causing a small, localized temperature rise, and a corresponding slight reduction in hydrogen density. If the residence time is too long and the heated hydrogen remains in the moderators for many pulses, the temperature can increase, the density can decrease, and consequently the cold neutron brightness can be reduced.

As shown in Figure 39, the main volumes receiving energy deposition from the pulsed proton beam are approximately 231755.5769 mm^3 and 304496.5331 mm^3 for cylindrical and tube moderators, respectively. The volumetric flow rate of liquid hydrogen is 0.5 L/s. Based on these volumes, the corresponding hydrogen flow-through times (defined as the moderator volume divided by the volumetric flow rate) are 0.46 s for the cylindrical moderators and 0.61 s for the tube moderator. As shown in Figure

32, Figure 33, and Figure 37, recirculation zones exist within the moderators, indicating that a portion of the hydrogen remains in the system longer than the nominal flow-through time. Figure 40 presents the residence time distributions for the cylindrical and tube moderators obtained from CFD simulations, which account for the increased residence time due to recirculation effects. It should be noted that the residence time distributions shown in Figure 40 include liquid hydrogen entering and exiting from both moderators, as well as the associated transfer lines, and are not limited solely to the main beam-exposed volumes shown in Figure 39. From Figure 40, the effective residence times are τ_c = 0.62 s (=1.87 s - 1.25 s) for the cylindrical moderator and τ_t = 0.82 s (= 3.00 s - 2.18 s) for the tube moderator, both of which are higher than the corresponding flow-through times of 0.46 s and 0.61 s.

As listed in Table 6, the steady-state heat loads of the cylindrical and tube moderators are 183.95 W and 235.56W, respectively. The energy deposited during one residence period can be estimated as 114.1 J for the cylindrical moderator (E_c = 183.95W*0.62s = 114.1 J) and 193.1 J for the tube moderator (E_t = 235.56W*0.82s = 193.1J).

The liquid hydrogen density at 20 K is approximately 72.82 kg/m^3 (Table 4), corresponding to hydrogen masses of 0.0169 kg for the cylindrical moderator and 0.0222 kg for the tube moderator within the beam-exposed volumes shown in Figure 39. The specific heat of liquid hydrogen at 14.5 bar and 20 K is 9030 J/kg-K (Table 4). The resulting temperature rise per residence time is therefore estimated to be ΔT_c = 0.75 K (=114.1 J / (0.0169 kg*9030 J/Kg-K)) for the cylindrical moderator and ΔT_t = 0.96 K (=193.1 J/ (0.0222 kg*9030 J/Kg-K)) for the tube moderator.

The number of proton pulses experienced during one residence period can be calculated as N_c = 15 Hz* τ_c = 15Hz*0.62s = 9 pulses for the cylindrical moderator and N_t = 15 Hz* τ_t = 15Hz*0.82s = 12 pulses for the tube moderator. Accordingly, the temperature rise per pulse is approximately ΔT_{cp} = 0.75 K/9 = 0.083 K/pulse for the cylindrical moderator and ΔT_{tp} = 0.96 K/12 = 0.08 K/pulse for the tube moderator.

In summary, the estimated temperature rise per residence time is less than 1 K, and the temperature rise per pulse is approximately 0.08 K. Although these estimates account only for energy deposition directly in the liquid hydrogen but do not include the heat transferred from the aluminum vessels to the hydrogen, they are consistent with the CFD simulation results.

The small temperature rise per pulse, combined with the relatively long thermal residence time compared to the pulse period, indicates that the moderator thermal response is effectively averaged over multiple pulses, leading to quasi-steady thermal behavior rather than significant transient fluctuations. This interpretation is supported by the CFD simulations, which show relatively uniform temperature and density distributions within the moderators under normal operating conditions.

Overall, a liquid hydrogen flow rate of 0.5 L/s provides adequate thermal margin to limit hydrogen density variations and thereby maintain stable cold neutron production performance.

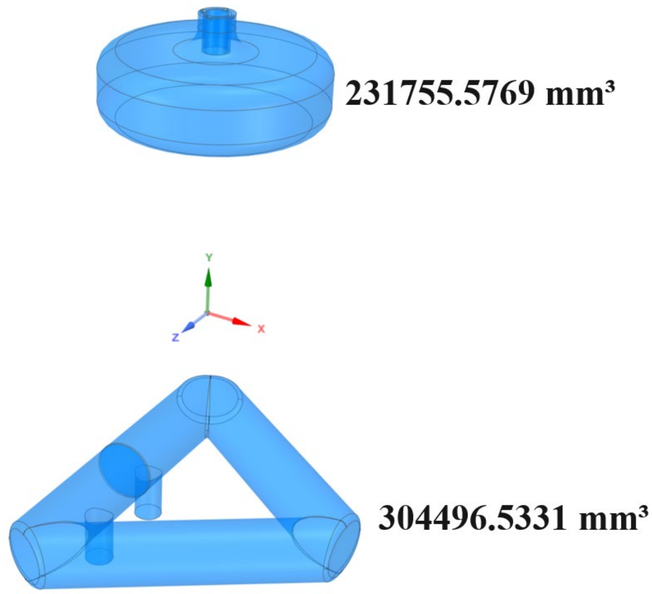

Figure 39. Main moderator volumes receiving the majority of pulsed proton beam energy.

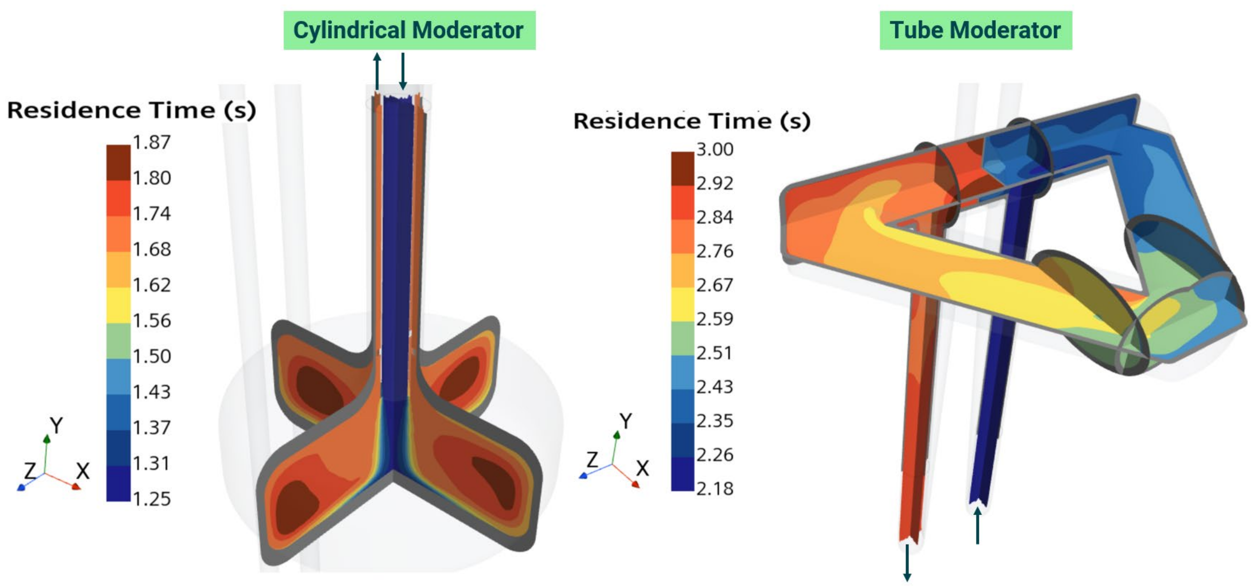

Figure 40. Residence time of hydrogen in cylindrical and tube moderators.

8.2 REFLECTOR VESSEL ASSEMBLY, BACKBONE, AND SHIELD BLOCK

8.2.1 Heat Source Distribution

The heat source distribution for the hydrogen loop is discussed in Section 8.1.1. The heat loads for the remaining MRA components are presented in this section. Figure 41 shows the overall heat source distribution of the MRA excluding the hydrogen loop. As illustrated in Figure 5, water and beryllium are encapsulated within aluminum vessels. The heat source distribution in the aluminum vessel is shown in

Figure 42. As summarized in Table 6, the total heat load in the aluminum vessels is 8.9 kW, with 4.3 kW in the upper reflector vessel and 4.6 kW in the lower reflector vessel.

Figure 43 presents the heat source distribution in the beryllium. Similar to the distributions observed in the hydrogen system (Figure 20) and the aluminum vessels containing beryllium and water (Figure 42), the beryllium exhibits heat peaking on the downstream side of the proton beam (+x direction). This behavior is attributed to slow and thermal neutrons generated in the rear portion of the tungsten targets. The total heat load in the beryllium is 12.3 kW, with 6.0 kW in the upper and 6.3 kW in lower beryllium components, as listed in Table 6.

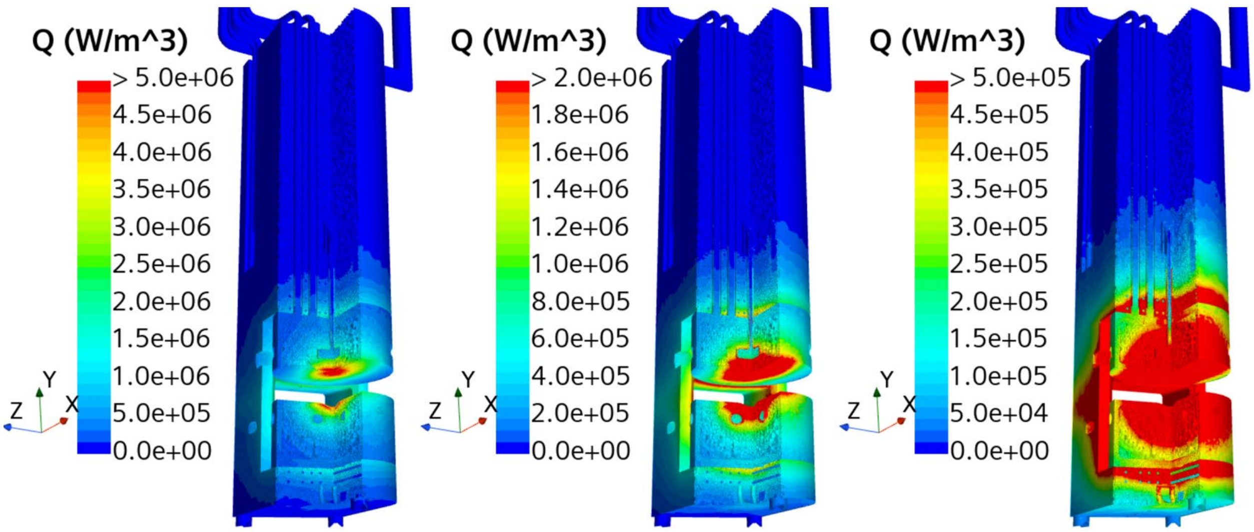

Figure 41. Heat source distribution in MRA (excluding H_2 Loop)

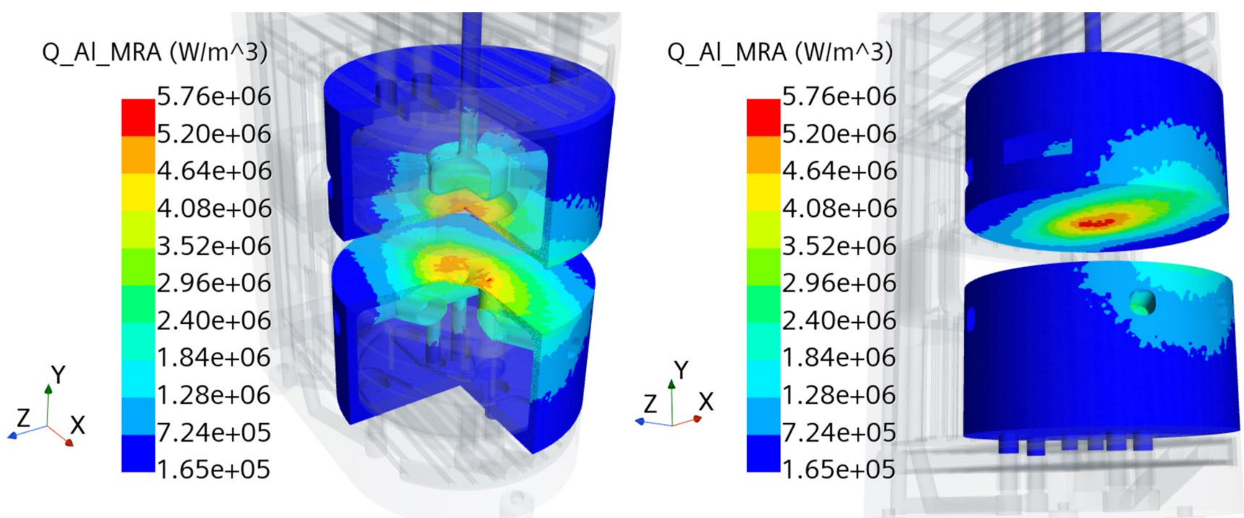

Figure 42. Heat source distribution in the Al vessel for water and beryllium (excluding the Al vessel for H_2 loop).

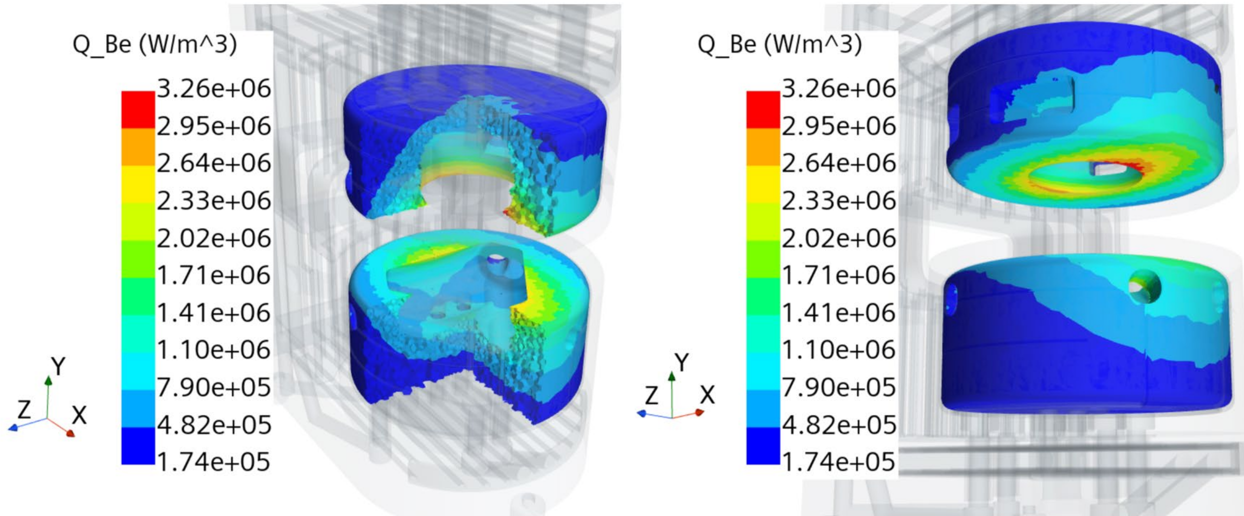

Figure 43. Heat source distribution in beryllium.

Stainless steel (SS316) provides excellent corrosion resistance and is commonly used for containment or confinement boundaries, making it well suited for corrosive or wet environments with reduced maintenance requirements. Accordingly, in the early MRA design, the shield block was fabricated from SS316 and incorporated internal cooling circuits to control temperature gradients and minimize thermal deflection. This design was required because the shield block is mechanically attached to the upper MRA block (Figure 44 and Figure 48); consequently, temperature gradients and thermal deformation in the shield block may be transferred to the upper block and influence moderator positioning and neutron beam port alignment.

Carbon steel (A36), while more susceptible to corrosion, can be adequately protected through surface coating, and controlled core vessel environment. Because the MRA is located within the Core Vessel (CV) and operates under vacuum or helium environments, the ambient conditions are well-controlled, significantly mitigating corrosion concerns.

Both A36 and SS316 are iron-based materials with comparable density (Table 2) and therefore exhibit similar energy deposition characteristics and shielding performance for gamma rays and fast neutrons. However, SS316 typically produces higher residual dose levels and requires longer cooldown periods due to activation of alloying elements such as nickel (e.g. formation of Co-60). In contrast, A36 contains fewer long-lived activation products. In addition, A36 is significantly less expensive and easier to machine and weld. For these reasons, A36 is generally favored for large shielding masses and has been selected for the final MRA shield block design.

An additional advantage of A36 is its higher thermal conductivity, which is approximately three times higher than that of SS316 (Table 2). This higher thermal conductivity allows for more effective heat diffusion within the shield block and enables a simplified cooling design. Because the A36 shield block is in direct contact with the well-cooled upper MRA block (Figure 45 and Figure 48), dedicated cooling circuits within the shield block can be minimized. The cooling configuration of the MRA backbone is shown in Figure 7 through Figure 10.

The total heat load in the A36 shield block is 798.7W, as listed in Table 6, and the corresponding heat source distribution is shown in Figure 44.

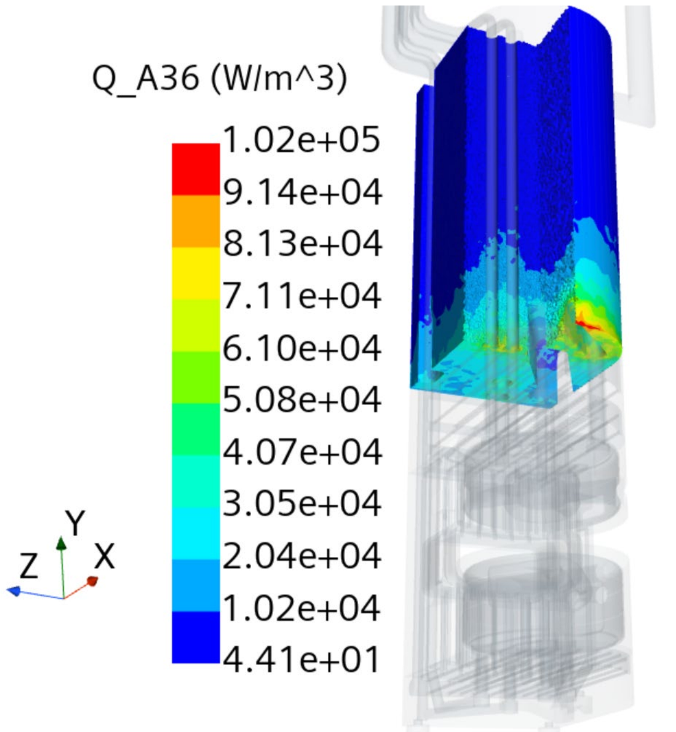

Figure 44. Heat source distribution in the A36 shield block.

While water serves as the primary coolant in the MRA, it also functions as a thermal neutron moderator (i.e., a premoderator for cold neutrons, as shown in Figure 46 and Figure 47) by slowing fast neutrons before they enter the liquid hydrogen moderator, thereby reducing heat deposition in the hydrogen. A total of **9.2 kW** of energy is deposited in the water, accounting for **15.8%** of the total heat load in the MRA; this energy deposition is included as a heat source term in the CFD simulations. The corresponding heat source distribution in the water is shown in Figure 45.

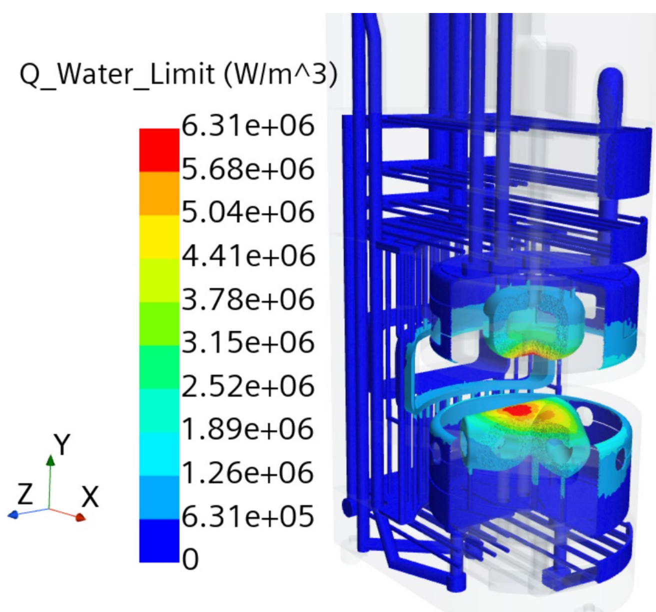

Figure 45. Heat source distribution in water (premoderators and reflector cooling waters).

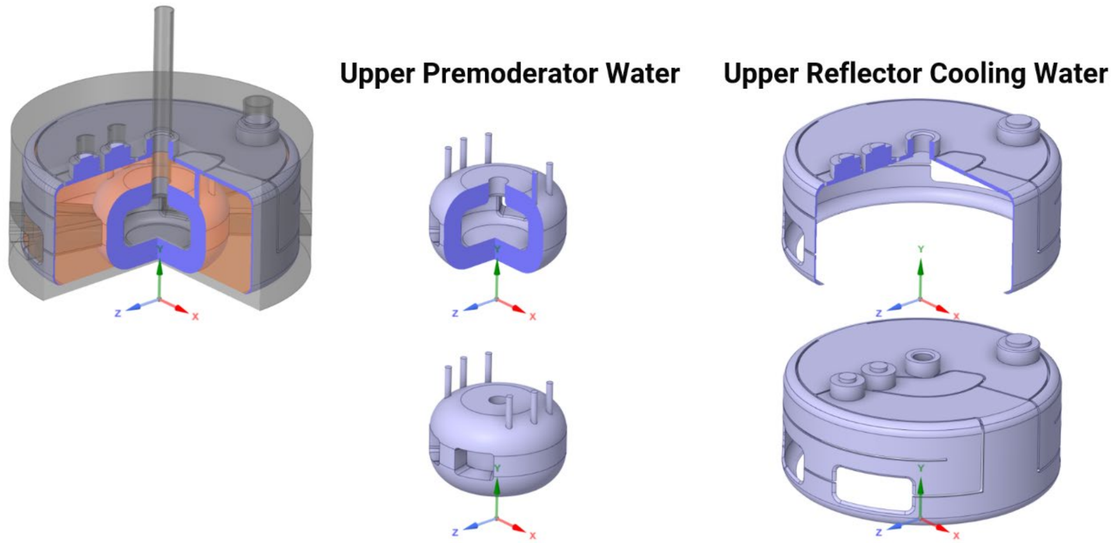

Figure 46. Upper premoderator water and upper reflector cooling water.

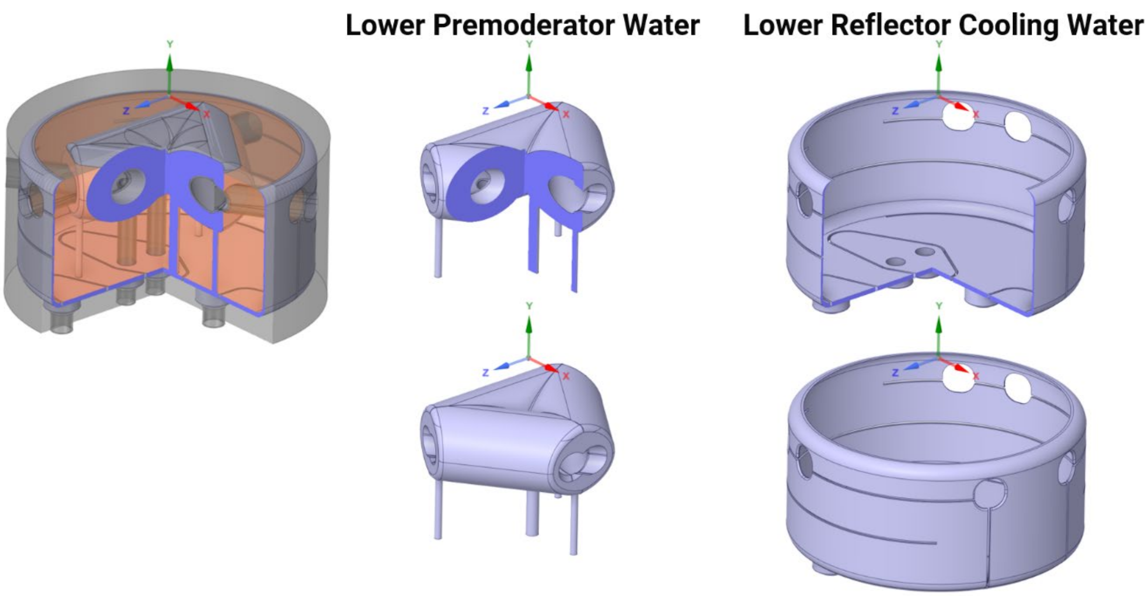

Figure 47. Lower premoderator water and lower reflector cooling water.

The heat loads deposited in the lower, middle and upper SS316 blocks are 5.6 kW, 12.5 kW, and 7.7 kW, respectively (Figure 48). The heat load in the SS420 kinetic mounts is 11 W (Figure 49). In the MRA backbone, the lower, middle, and upper blocks are assumed to be in perfect thermal contact for the heat transfer analysis as the majority of their contact areas are welded. The impact of thermal contact resistance is less than 3 °C and is discussed further in APPDNDIX B.

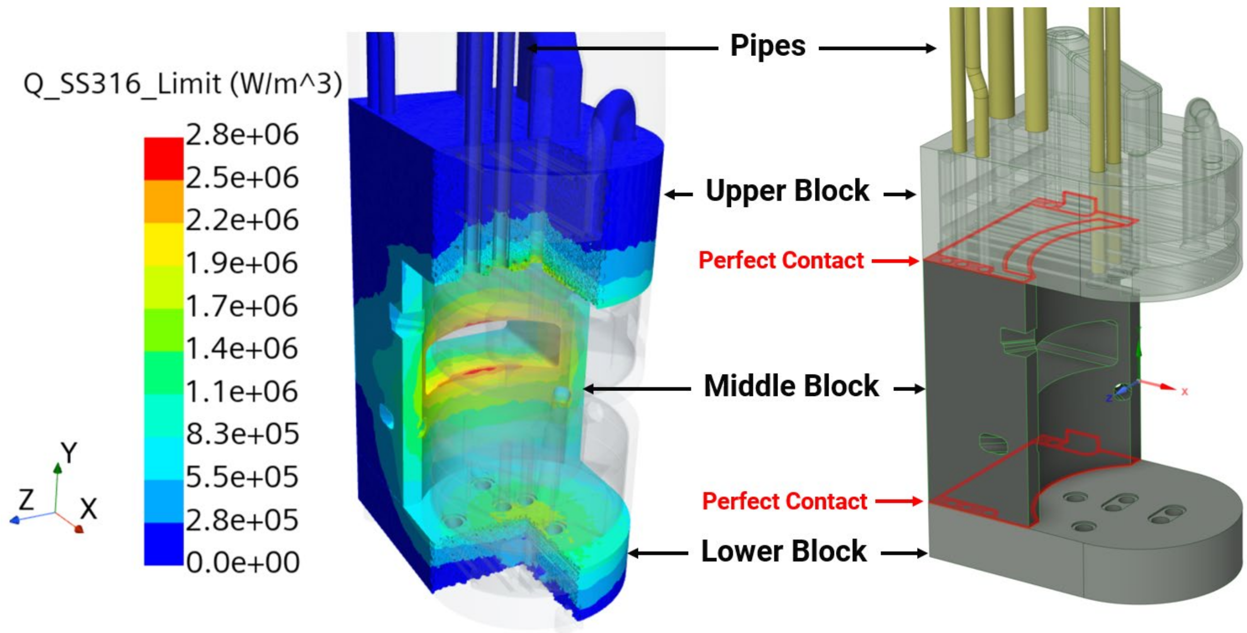

Figure 48. Heat source distribution in the upper, middle, and lower blocks.

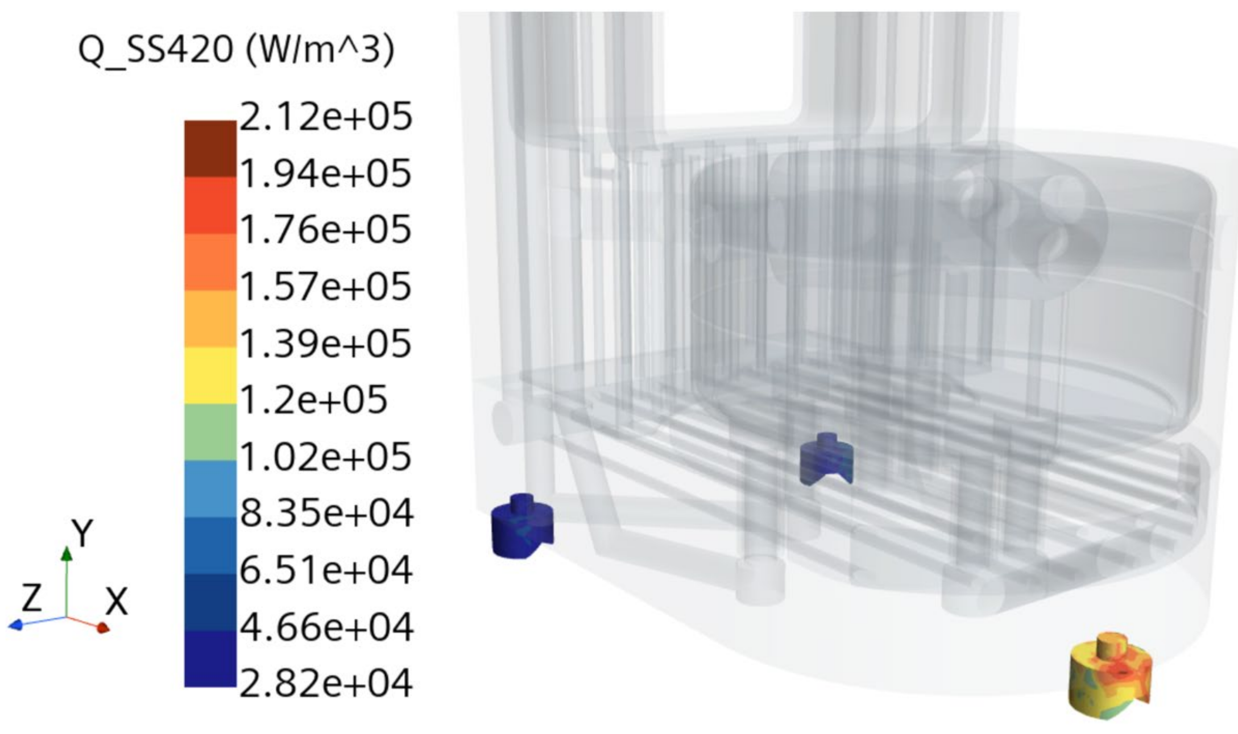

Figure 49. Heat source distribution in the kinetic mounts.

8.2.2 Pressure Distribution

As shown in Figure 4 and Figure 7, the MRA water cooling system consists of five independent inlet streams that merge into a single common outlet. Inlet_1 and inlet_3 supply water to the outer regions of the upper and lower reflector vessels, respectively, where the water functions as reflector cooling water. Inlet_2 and inlet_4 supply water to the inner regions of the upper and lower reflector vessels, respectively, where the water serves as premoderator water adjacent to the hydrogen moderators while also providing cooling. Each of these four circuits operates at a flow rate of 7.5 GPM (0.47 kg/s) with an inlet temperature of 90 °F (32.2 °C). The MRA backbone is cooled by a separate water stream (Inlet_5) operating at 15 GPM (0.94 kg/s) and 90 °F (32.2 °C).

The pressure drops across the upper and lower premoderator water circuits are 5.2 psi and 6.86 psi, respectively. Due to the narrower flow passages in the reflector cooling water regions (Figure 46 and Figure 47), higher pressure drops are observed, with values of 9.65 psi for the upper reflector cooling circuit and 9.55 psi for the lower reflector cooling circuit. The pressure drop across the backbone cooling loop is 4.3 psi. The pressure distributions are shown in Figure 50 and Figure 51.

The simulation results indicate that the current MRA satisfies the design requirement of maintaining a pressure drop below 15 psi across the entire assembly.

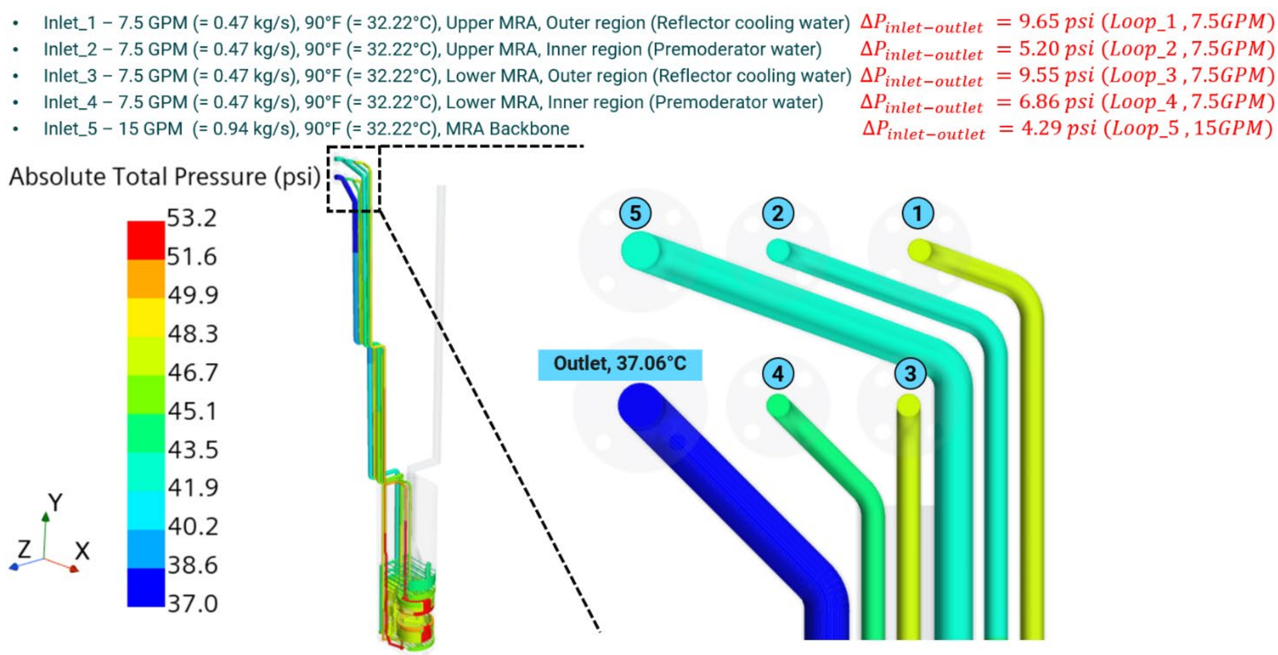

Figure 50. Pressure distribution in MRA with the four supplies and the common return.

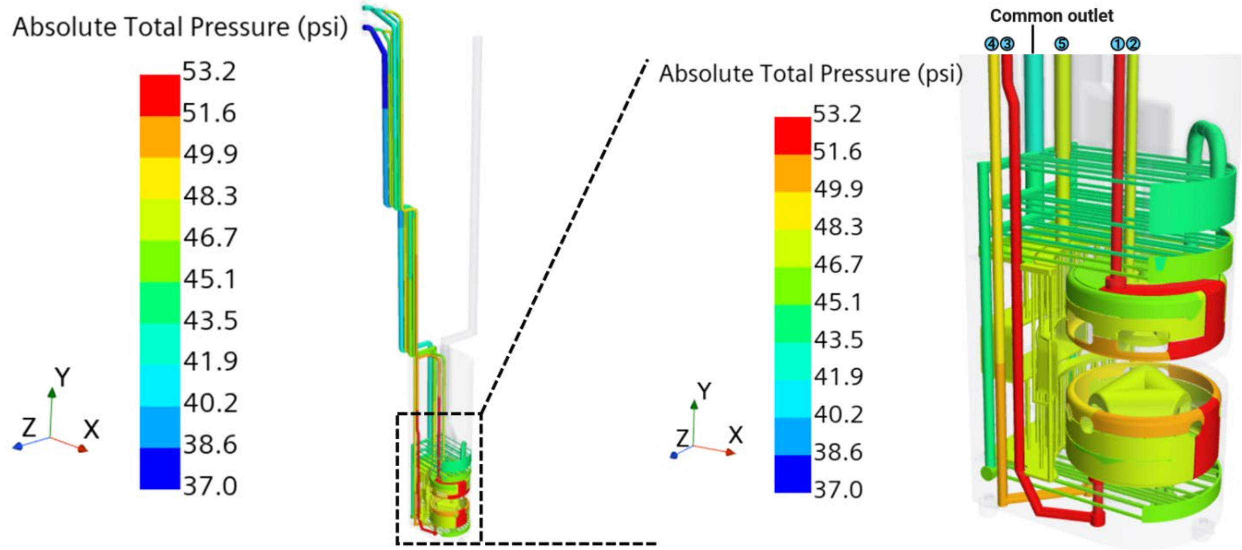

Figure 51. Pressure distribution in the upper and lower reflectors.

8.2.3 Temperature Distribution

Five water streams enter the MRA at an inlet temperature of 90 °F (32.2 °C) and exit through a common outlet at a temperature of 37.06 °C, as shown in Figure 52. The peak water temperature of 51 °C occurs at the top of the tube premoderator, where the water is in direct contact with the aluminum vessel (Figure 5 and Figure 47). This region is characterized by low flow velocity due to the vessel geometry and high volumetric heat deposition resulting from energetic fast neutrons entering the aluminum vessel (Figure 42) and the water (Figure 45).

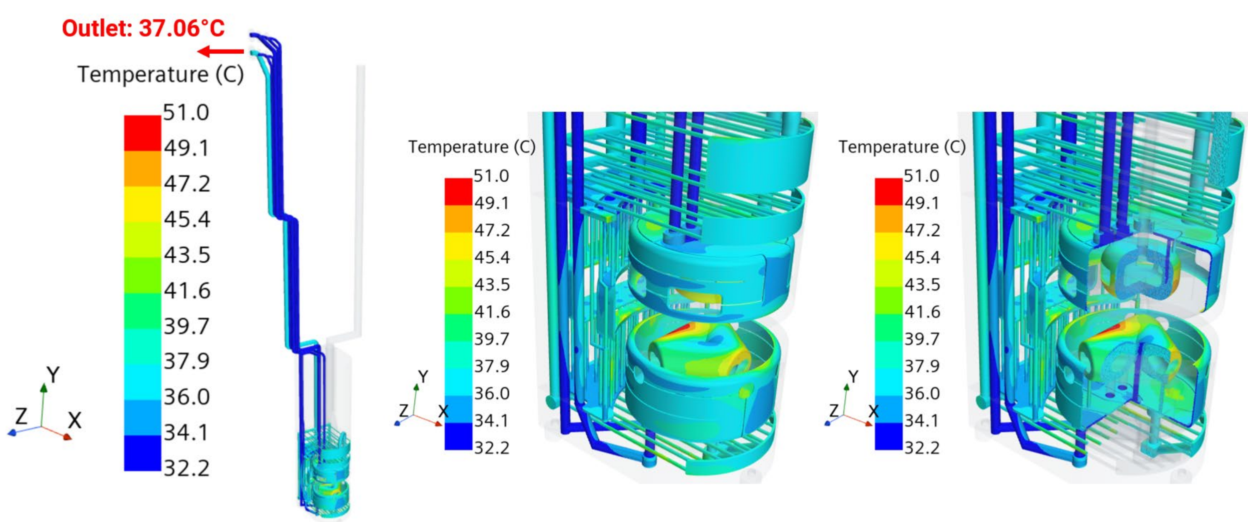

Figure 52. Temperature distribution in water of MRA.

Figure 53 shows the temperature distribution in the MRA, excluding the hydrogen loop. The peak temperature of 84.4 °C occurs in the lower SS316 block. It can be observed that the temperature profiles around the kinetic mounts are not uniform due to the non-uniform heat sources, as shown in Figure 41 and Figure 49. The entire MRA is supported on CV shield Block #1 via kinetic mounts. The temperature profile is exported for structural analysis to ensure the thermal distortion around the mounts does not have a significant impact on the alignment of the neutron beam ports.

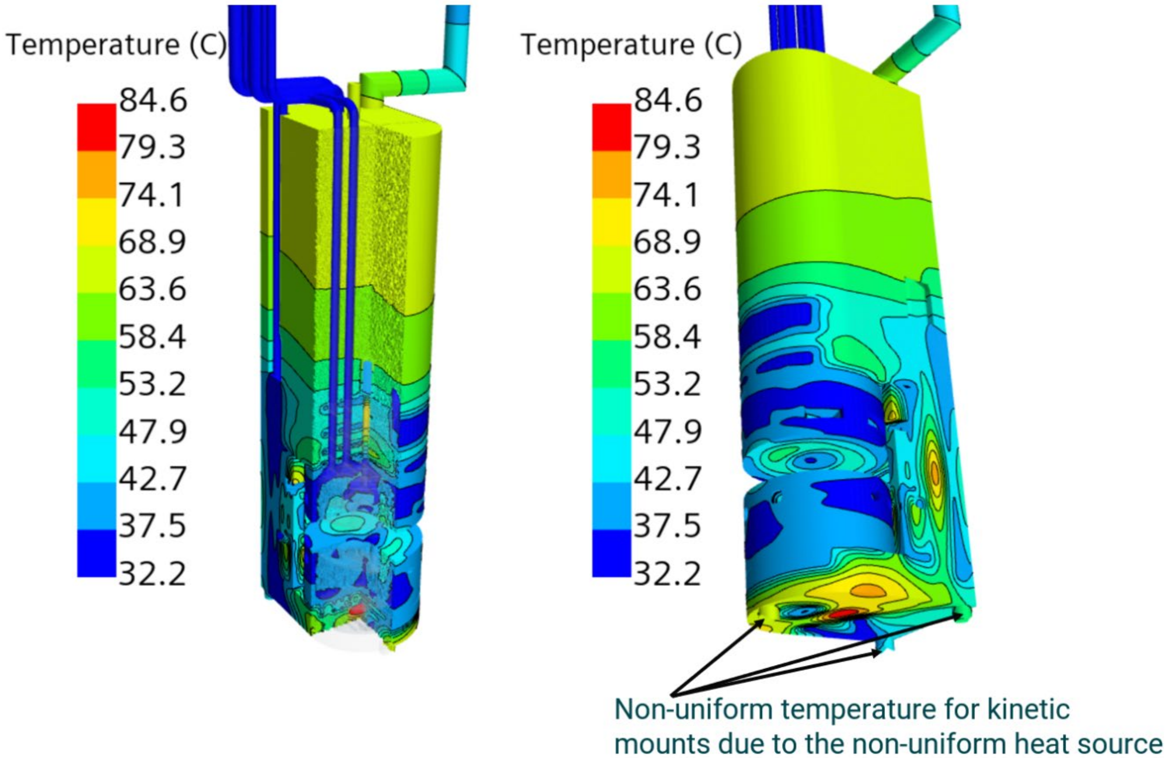

Figure 53. Temperature distribution in MRA (excluding H_2 Loop).

Figure 54 shows the temperature distribution in the aluminum vessels. The peak temperature in the lower vessel is approximately 53 °C, while the peak temperature in the upper vessel is approximately 58 °C; both occur in the region close to the proton beam. The peak temperature on the surface of the lower vessel facing the hydrogen loop is 42 °C, while the peak temperature on the upper vessel facing the hydrogen loop is 39 °C. It can also be observed that the peak temperature in the connecting aluminum pipe is 73.1 °C due to the long vacuum region along the pipe, which hinders heat conduction.

Figure 55 shows the temperature distribution in the beryllium components. In the STS MRA design, no additional dedicated vessels are used for the berylliums. The inner surfaces of the beryllium components are in direct contact with the premoderators (water), while the outer surfaces are in direct contact with the reflectors (water), thereby enhancing heat transfer. The top surface of the lower beryllium component and the bottom surface of the upper beryllium component are in direct contact with the aluminum vessels and therefore experience higher peak temperatures of 51°C and 55°C, respectively.

Figure 56 shows the temperature distribution in the A36 carbon steel shield block. Due to the higher thermal conductivity of A36, the temperature profile is relatively uniform even without dedicated cooling circuits. The temperature peaks at 65.2 °C and gradually reduces to 42.2 °C at the bottom surface, where it is in contact with the well-cooled upper block of the MRA backbone.

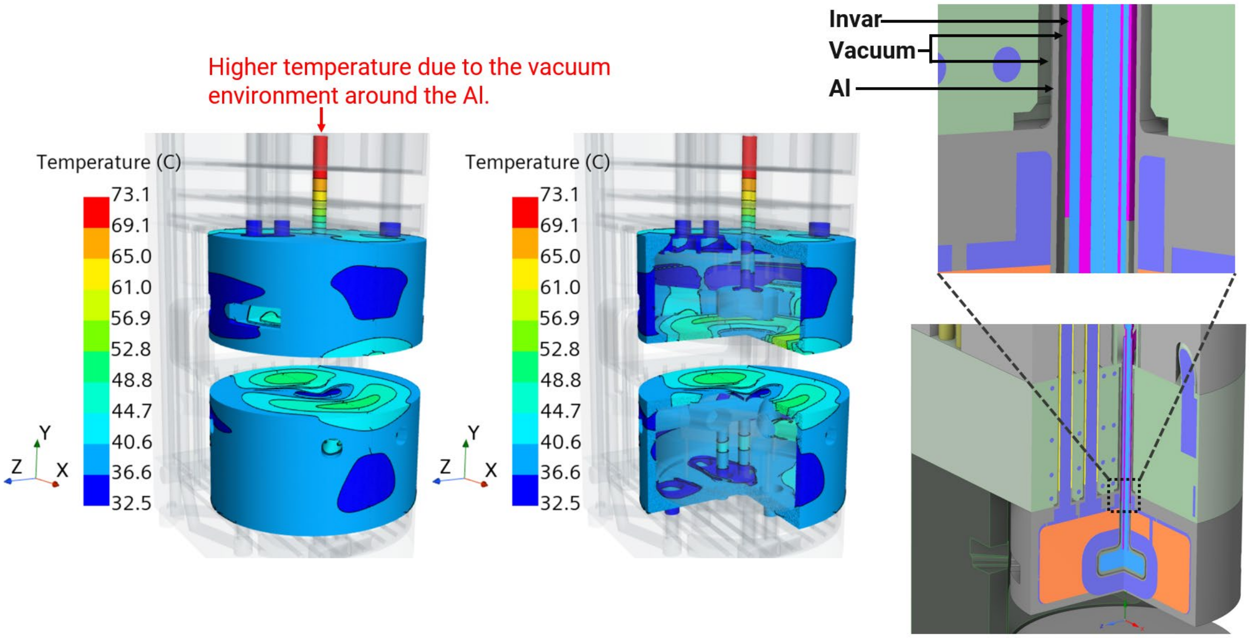

Figure 54. Temperature distribution in the Al vessel.

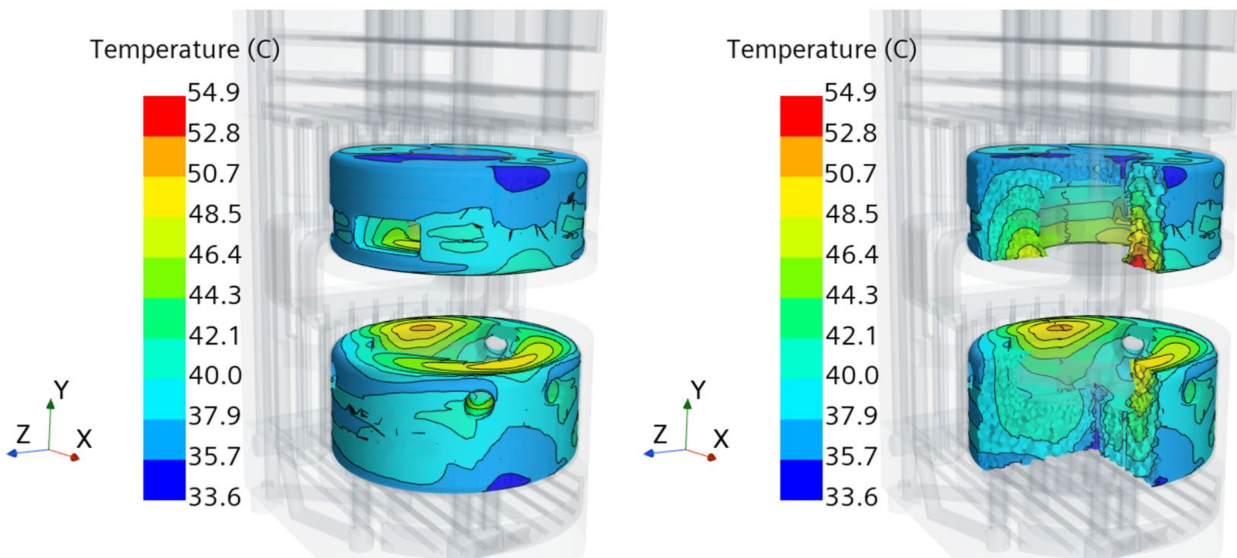

Figure 55. Temperature distribution in beryllium.

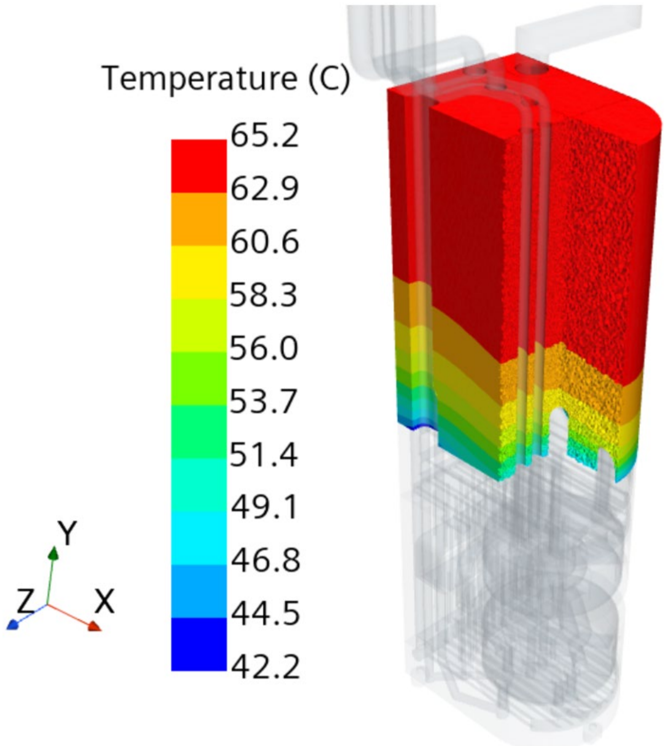

Figure 56. Temperature distribution in the shield Block (A36).

Figure 57 shows the temperature distribution in the SS316 components (MRA backbone). In the preliminary MRA design, all backbone blocks (lower, middle, upper, and shield) were made of SS316, with a peak temperature of 117 °C occurring in the upper block. In the final MRA design, the SS316 shield block is replaced with an A36 block with higher thermal conductivity. Furthermore, the cooling circuits have been modified to improve heat transfer, resulting in a more uniform backbone temperature profile and reduced thermal distortion that could affect moderator alignment. The peak temperature of 84.6 °C occurs in the lower backbone vacuum cover, which is located in the lower block and is associated with the hydrogen loop piping and limited space for cooling circuits, as shown in Figure 58 and Figure 59. As shown in Figure 60, the peak temperature of the SS420 kinetic mounts is 66 °C.

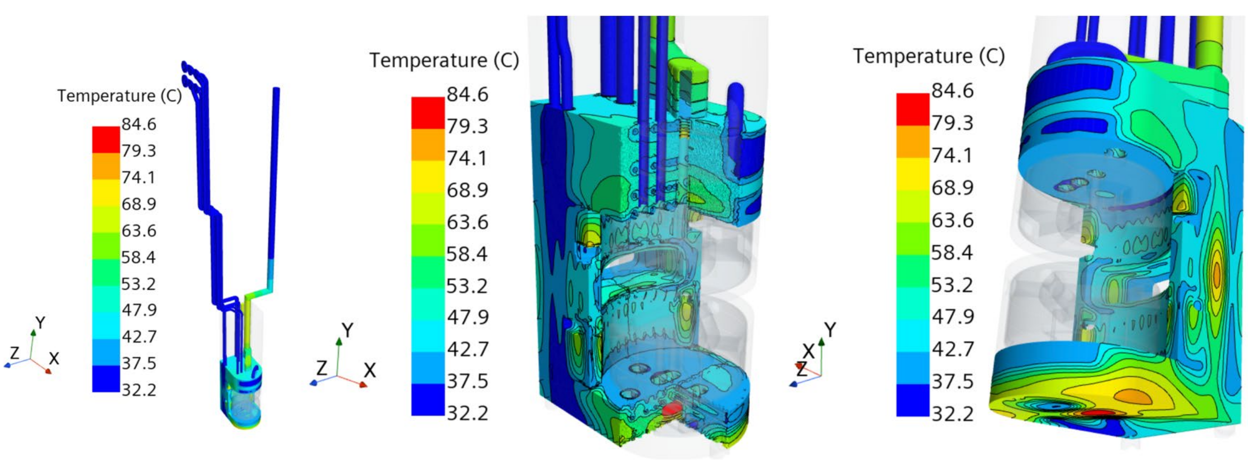

Figure 57. Temperature distribution in SS316 (pipes, upper, middle, and lower blocks).

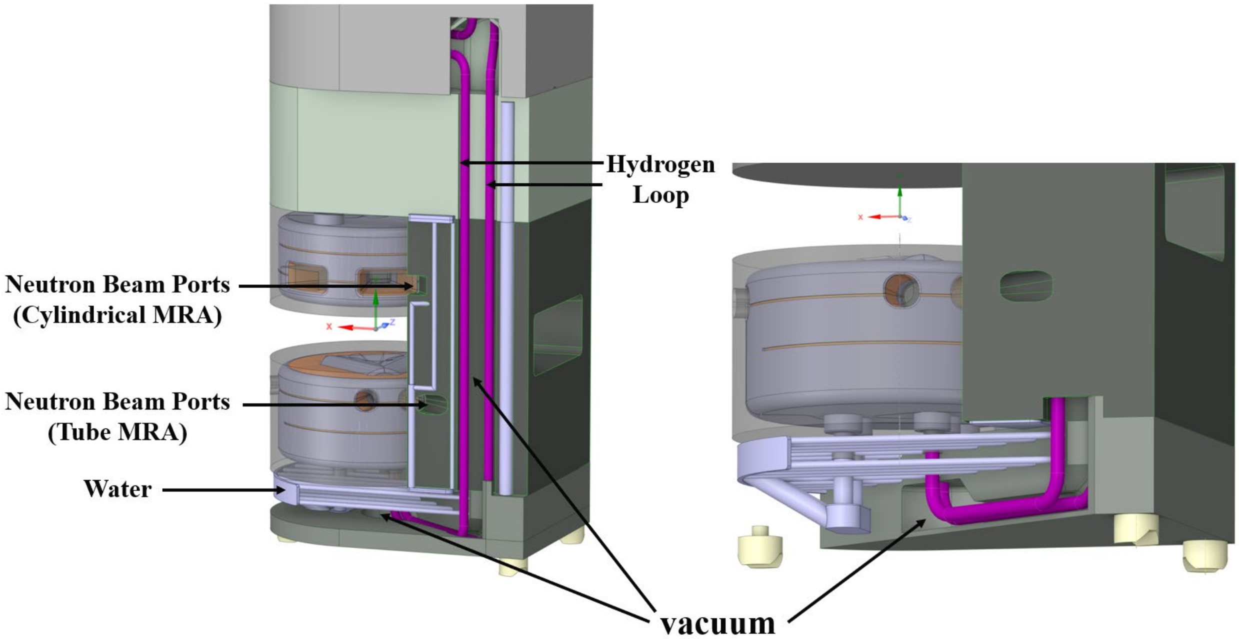

Figure 58. Neutron beam ports and vacuum region in the MRA.

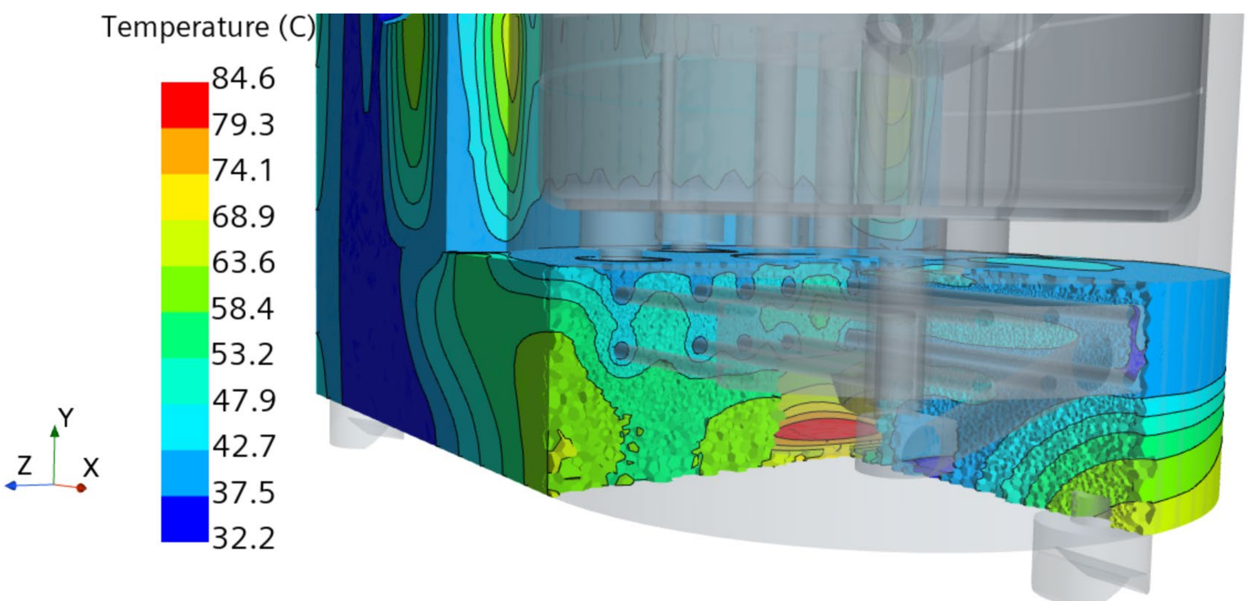

Figure 59. Temperature distribution in the lower block.

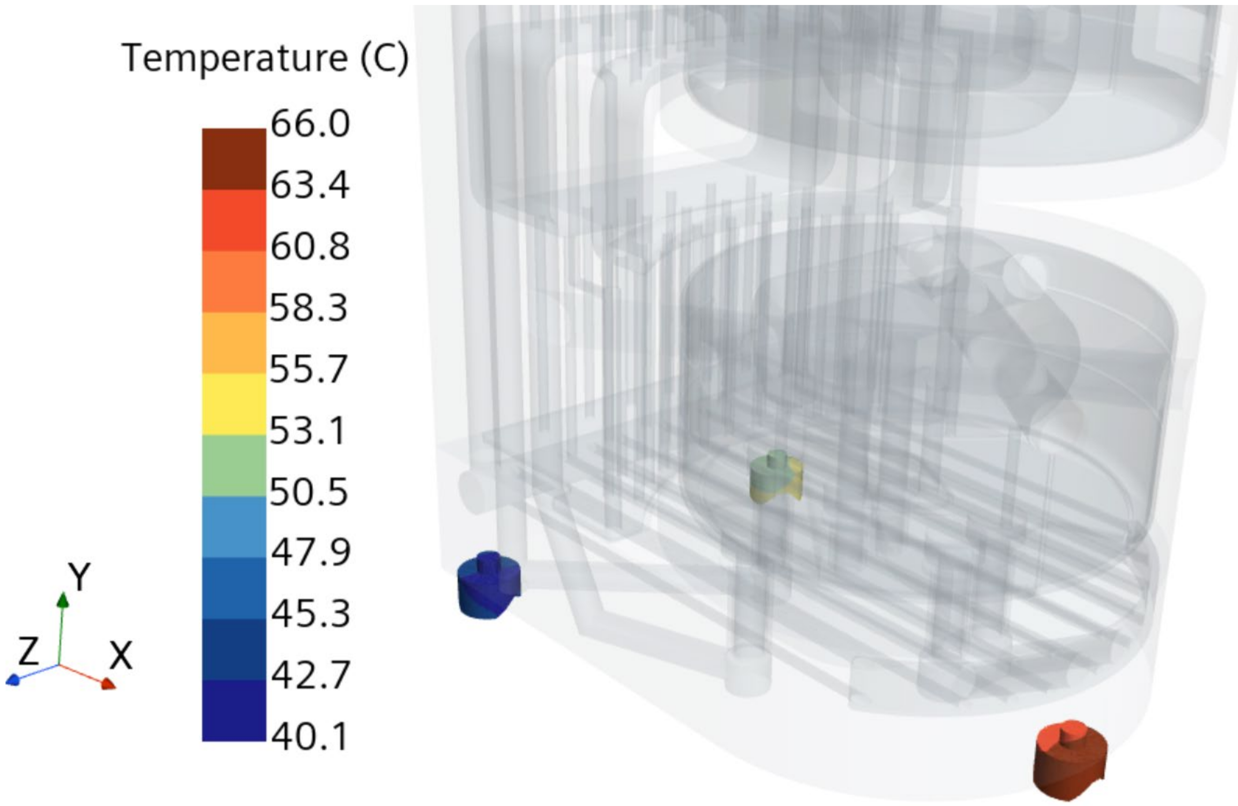

Figure 60. Temperature distribution in SS420 kinetic mounts.

Figure 61 shows the temperature distribution on different cut planes of the MRA backbone. Plane_1 corresponds to the upper (cylindrical) MRA neutron beam ports (Figure 58), with temperatures ranging from 33.5 °C to 59.4 °C. The peak temperature of 59.4 °C occurs near the vacuum region (pipe chase) associated with the hydrogen loop, as shown in Figure 58. Similarly, the Plane_5 corresponds to the lower (tube) MRA neutron beam ports (Figure 58), with temperatures ranging from 34 °C to 66 °C.

Plane_3 corresponds to the middle of the backbone and lies in the horizontal plane of the STS global center, where the target wheel is centered and the proton beam enters. The temperature distribution in Plane_3 ranges from 34 °C to 76 °C, which represents the highest temperature outside of the lower backbone vacuum cover.

Plane_2 is located between Plane_1 (cylindrical MRA) and the large open window of the MRA, with temperatures ranging from 34 °C to 64 °C. Similarly, Plane_4 corresponds to the plane between Plane_5 (tube MRA) and the large open window, with temperatures ranging from 34 °C to 70 °C.

Figure 62 compares the temperature profiles on the planes through the upper (cylindrical MRA) and lower (tube MRA) neutron beam ports between the MRA PDR and FDR designs. As shown in Figure 62, there are four rows of cooling channels passing through the MRA backbone. In the PDR design, the spacing between the rows of cooling channels is smaller, leading to a more non-uniform temperature profile. In the FDR design, additional cooling channels are added at hot spots, the sizes of some cooling channels are modified, and, most importantly, the four rows of cooling channels are rearranged to increase the spacing, all of which result in a more uniform temperature profile and reduced thermal distortion around the neutron beam ports.

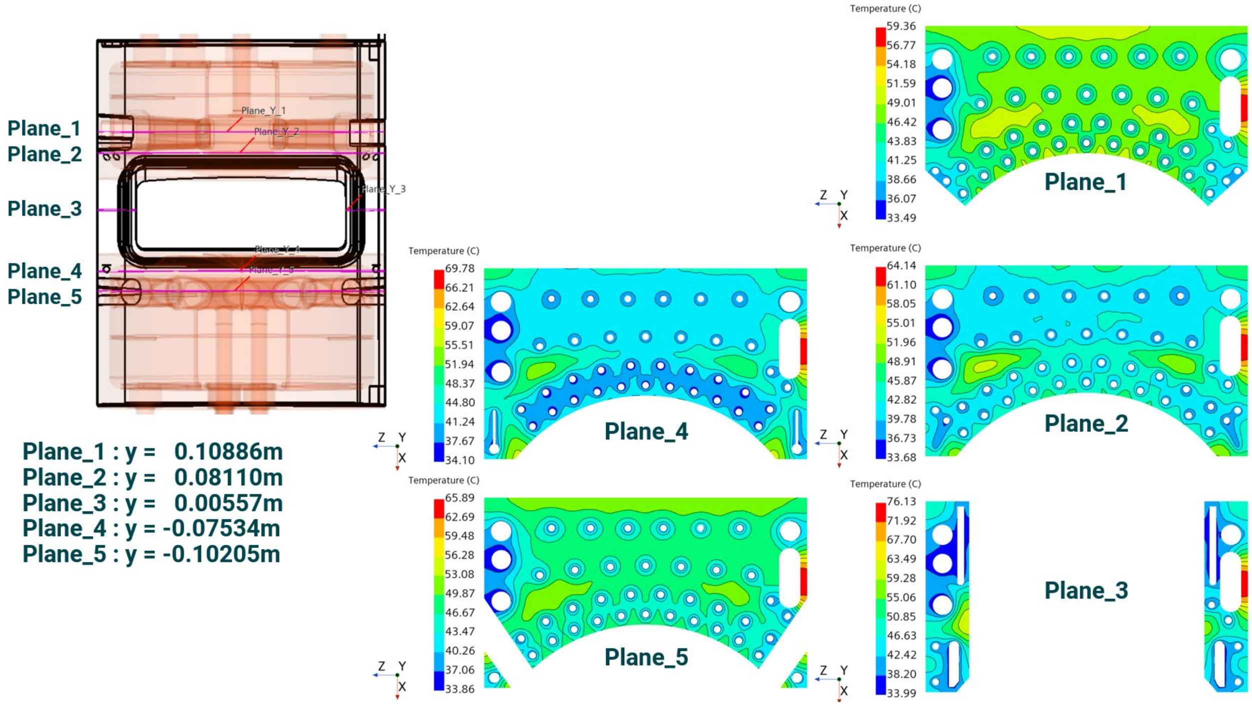

Figure 61. Temperature distribution in MRA backbone around the neutron beam ports (Plane_1 and Plane_5).

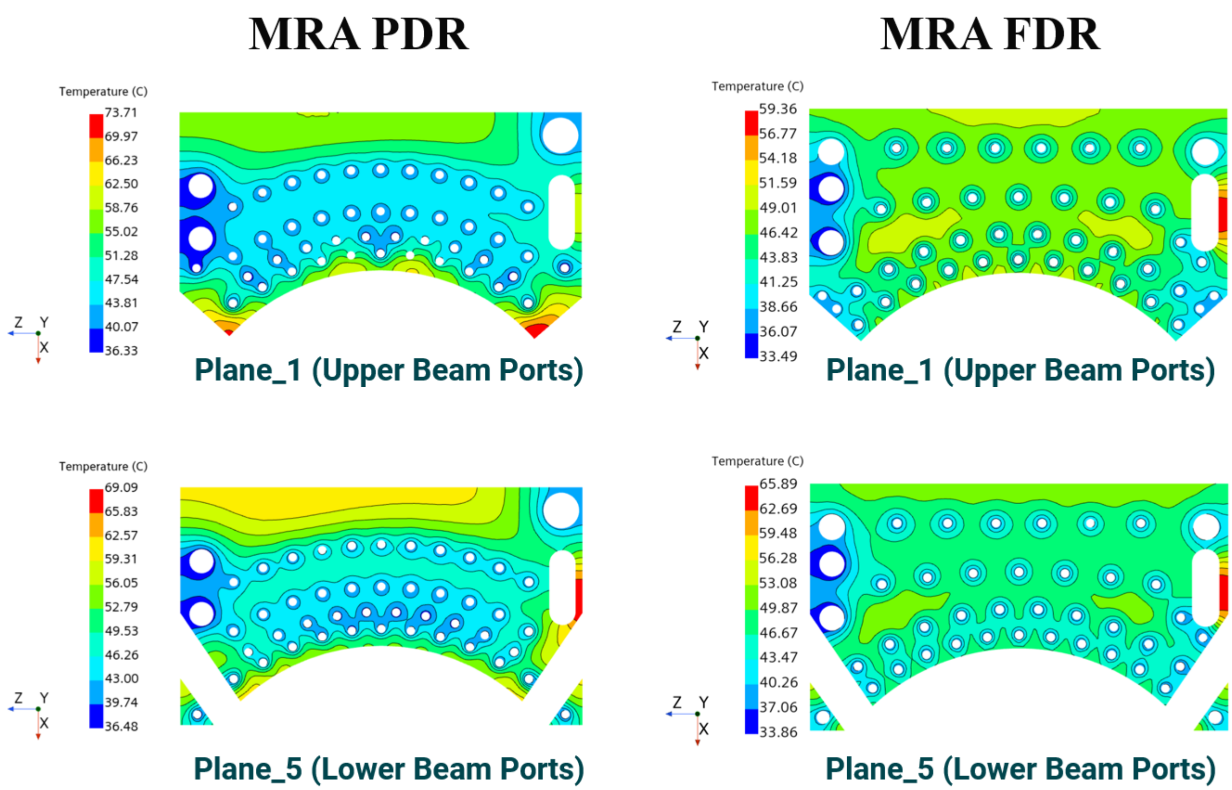

Figure 62. Comparison between the MRA PDR and FDR designs.

8.2.4 Velocity, Streamlines, and Temperature in Reflector Vessel Assembly (Excluding Hydrogen Loop)

The water velocity and streamlines in the aluminum reflector vessel (excluding the hydrogen loop) are shown in Figure 63. The flow directions in the water domain and the backbone are described in the GEOMETRY section and in Figure 8, Figure 9, and Figure 10.

Figure 64 shows the volumes of the premoderator water and reflector cooling water. It can be observed that the premoderator waters provide larger flow volumes for water circulation and therefore exhibit a lower pressure drop of approximately 5-7 psi. In contrast, the cooling channels in the reflector cooling circuits are much narrower, resulting in a higher pressure drop of 9.6 psi, as shown in Figure 50.

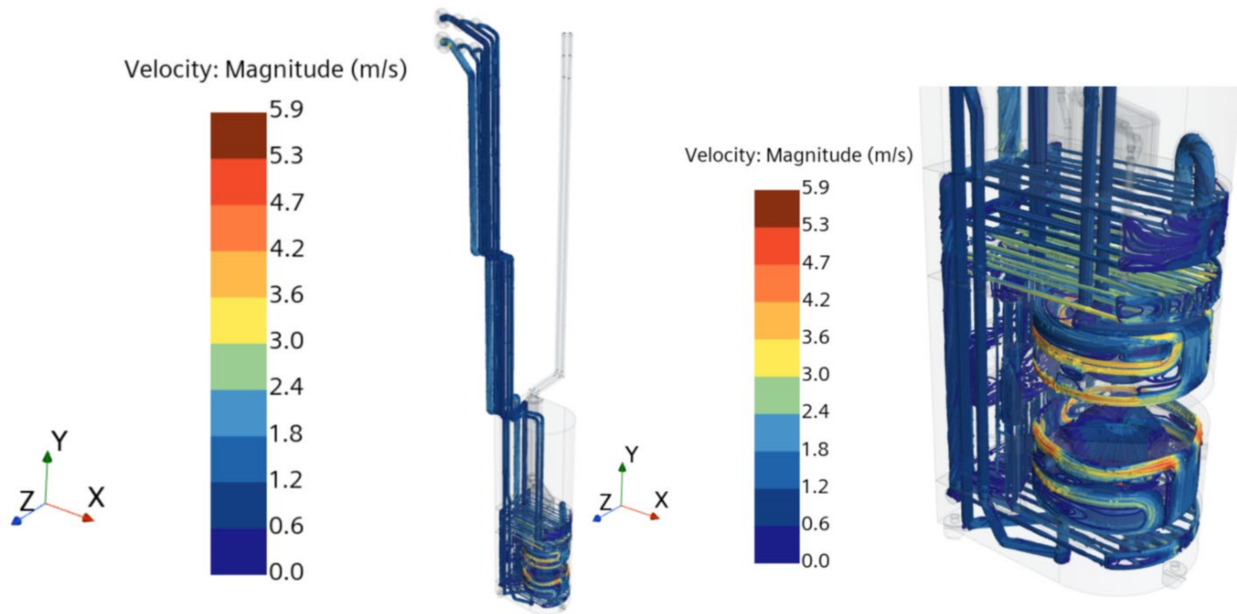

Figure 63. Water streamlines in MRA (excluding the hydrogen loop).

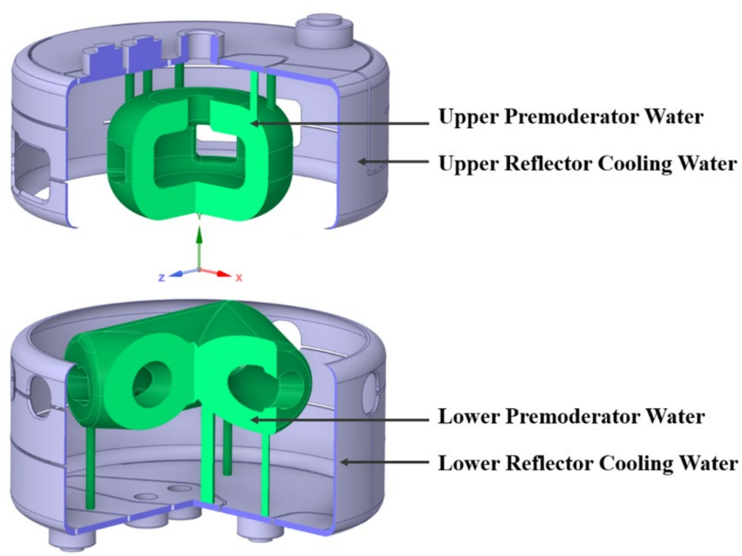

Figure 64. Water domains in the upper and lower MRA assemblies, showing premoderator regions (inner) and reflector cooling regions (outer).

Figure 65 and Figure 66 present sectional and cutaway views of the upper and lower reflector vessel assemblies. As expected, the water velocity in the reflector cooling water regions is higher and can exceed 5 m/s due to the narrower cooling channels, whereas the velocity in the premoderator water regions remains below 4 m/s due to their larger flow passages. The corresponding velocity profiles and vector fields are presented in Figure 67.

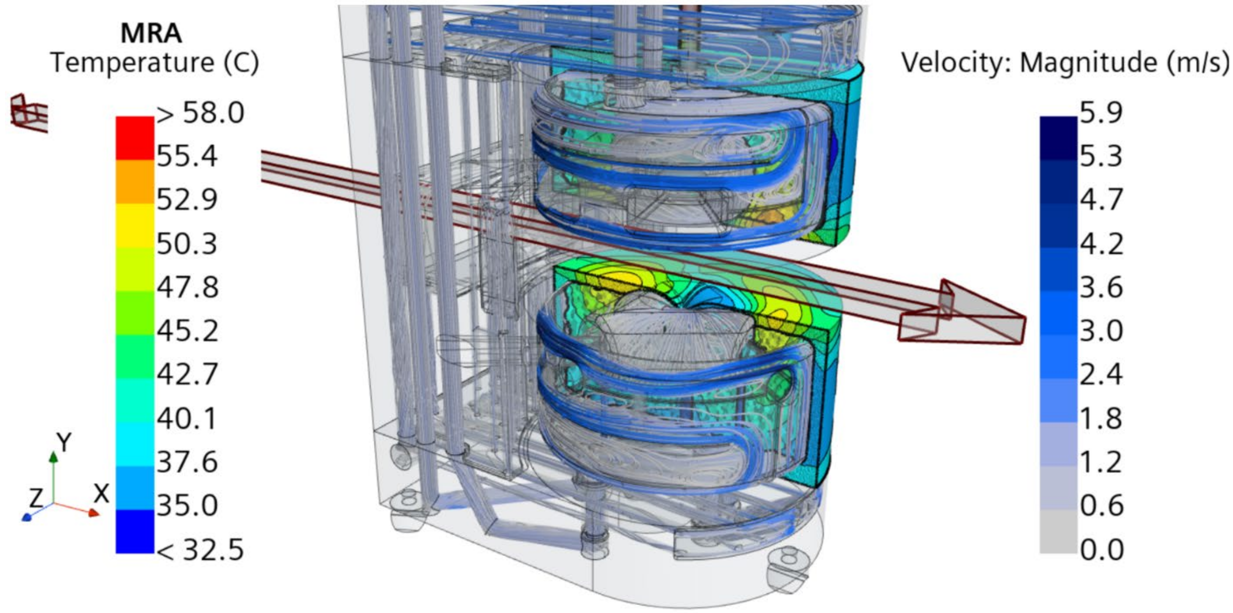

Figure 65. Temperature distribution and streamlines in the water domain (reflector cooling water and premoderator water) (sectional view).

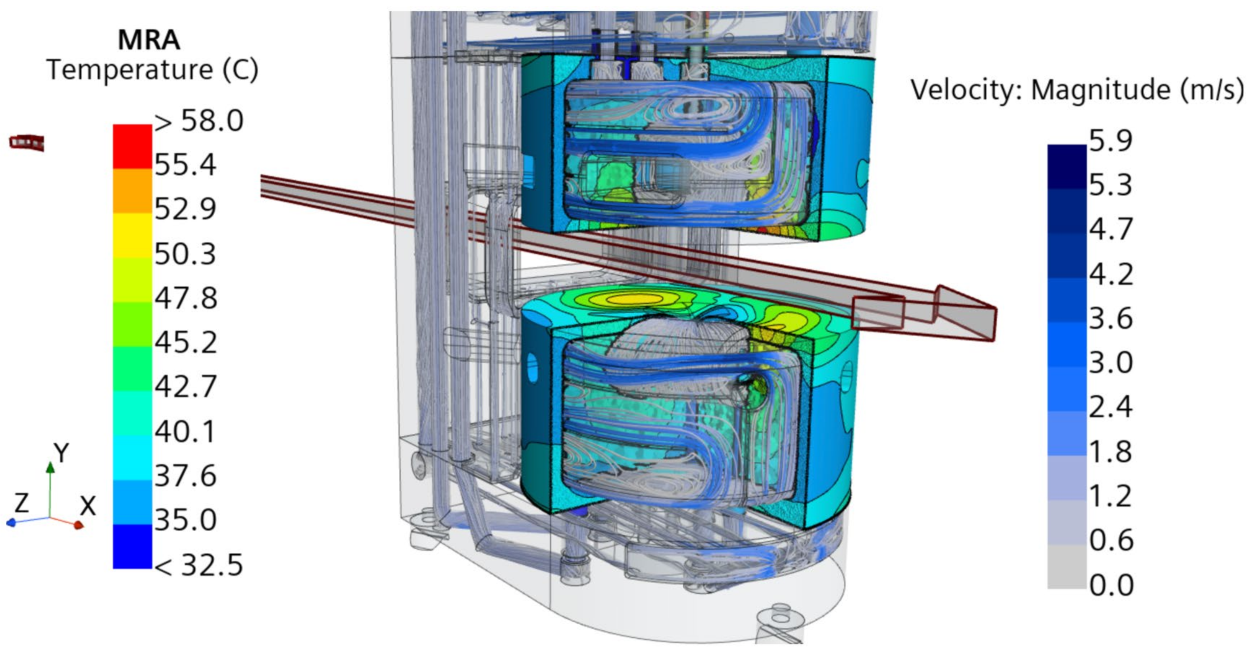

Figure 66. Temperature distribution and streamlines in the water domain (reflector cooling water and premoderator water) (cutaway view).

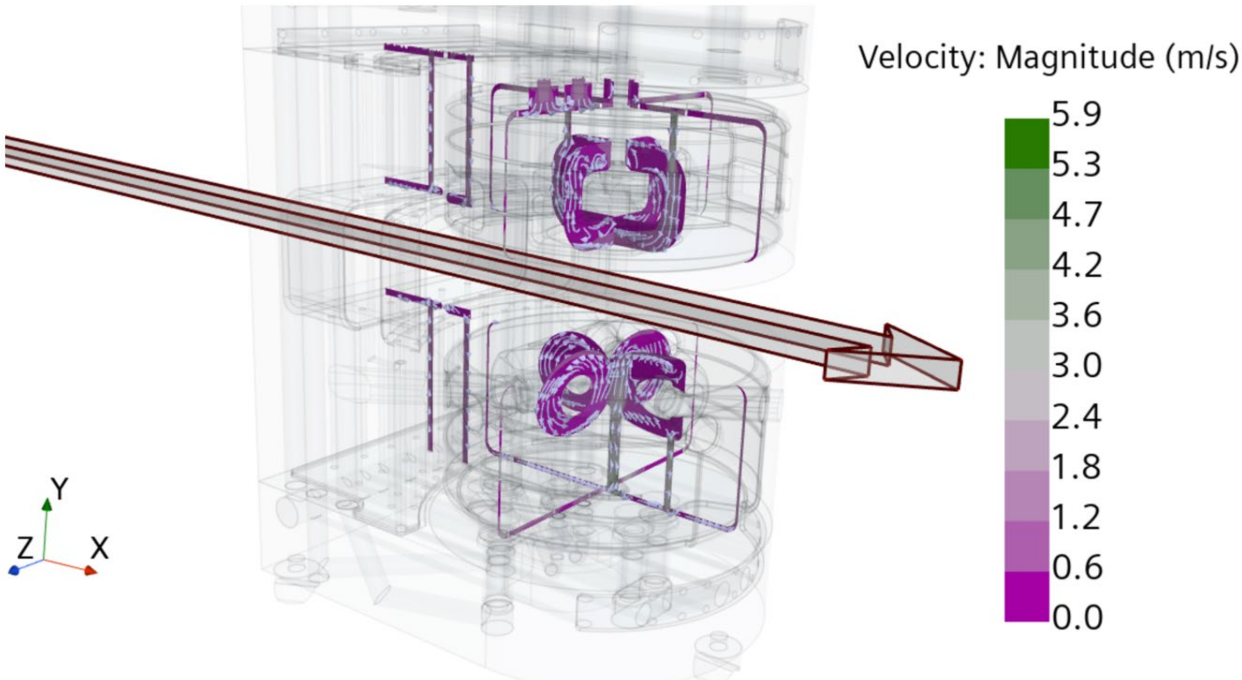

Figure 67. Velocity distribution in the water domain (reflector cooling water and premoderator water).

Figure 68, Figure 69, Figure 70, and Figure 71 present the temperature distributions and velocity fields in the upper and lower reflector vessel assemblies. The peak beryllium temperature reaches 55 °C (Figure 55) and is located in a region remote from the premoderator water and reflector water cooling streams. The aluminum vessel exhibits a similar behavior, with a maximum temperature of 58 °C (excluding the aluminum pipe near the vacuum gap) occurring in a similar region.

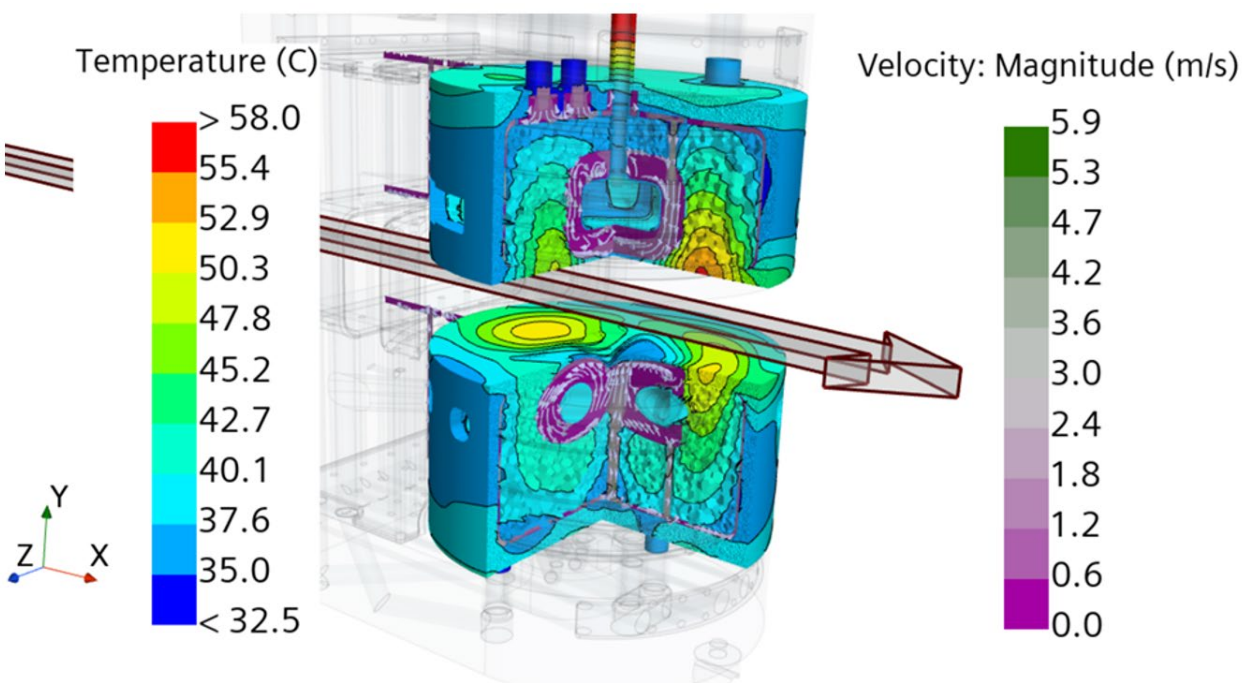

Figure 68. Temperature and velocity distributions in the upper and lower reflector vessel assemblies, excluding H_2 loop (cutaway view).

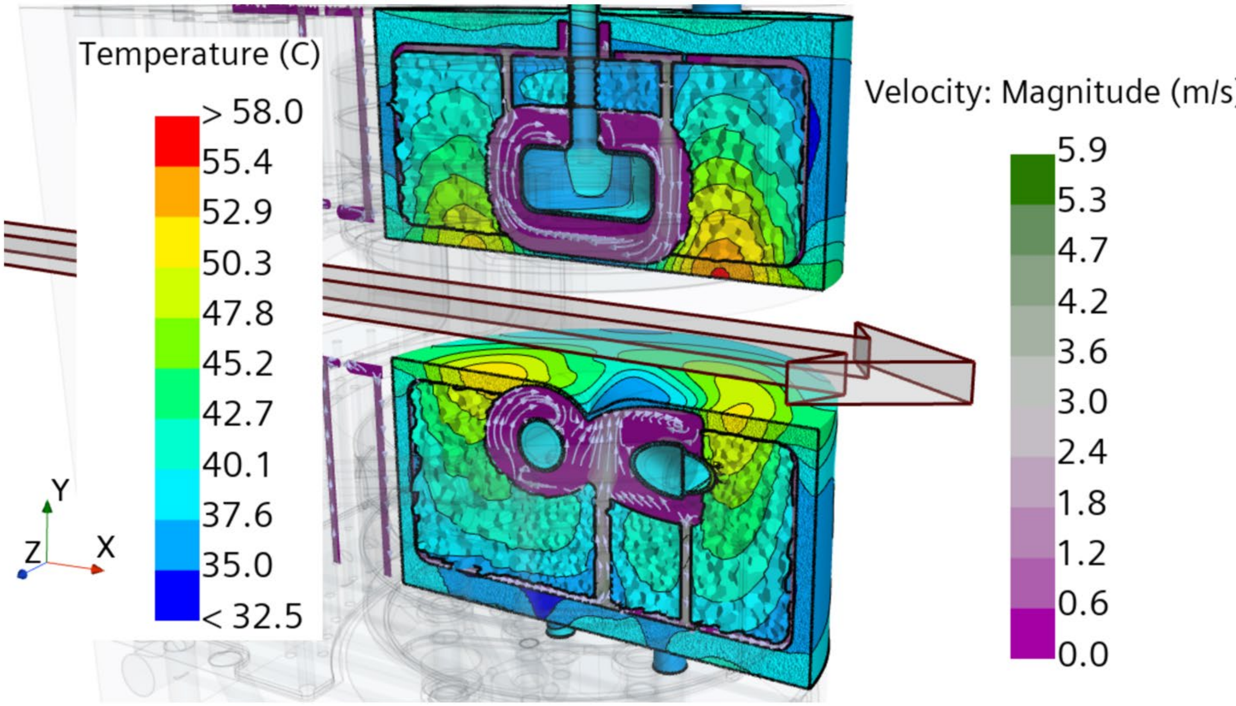

Figure 69. Temperature and velocity distributions in the upper and lower reflector vessel assemblies, excluding H_2 loop (sectional view).

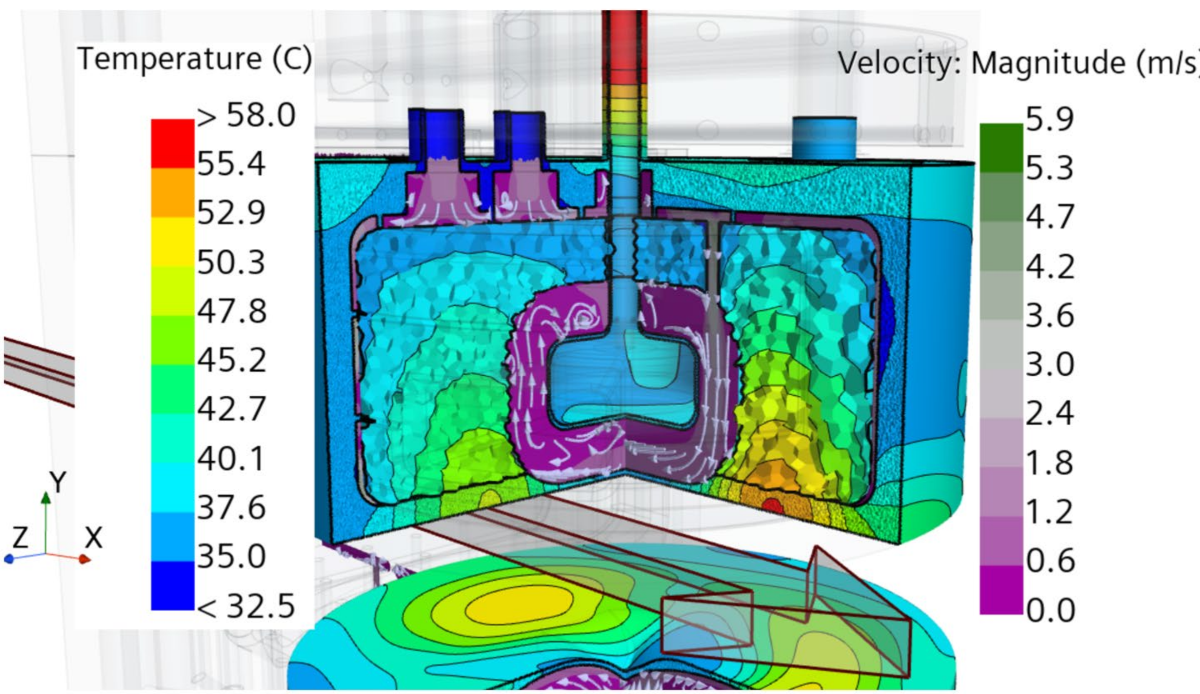

Figure 70. Temperature and velocity distributions in the upper reflector vessel assembly, excluding H_2 loop (cutaway view).

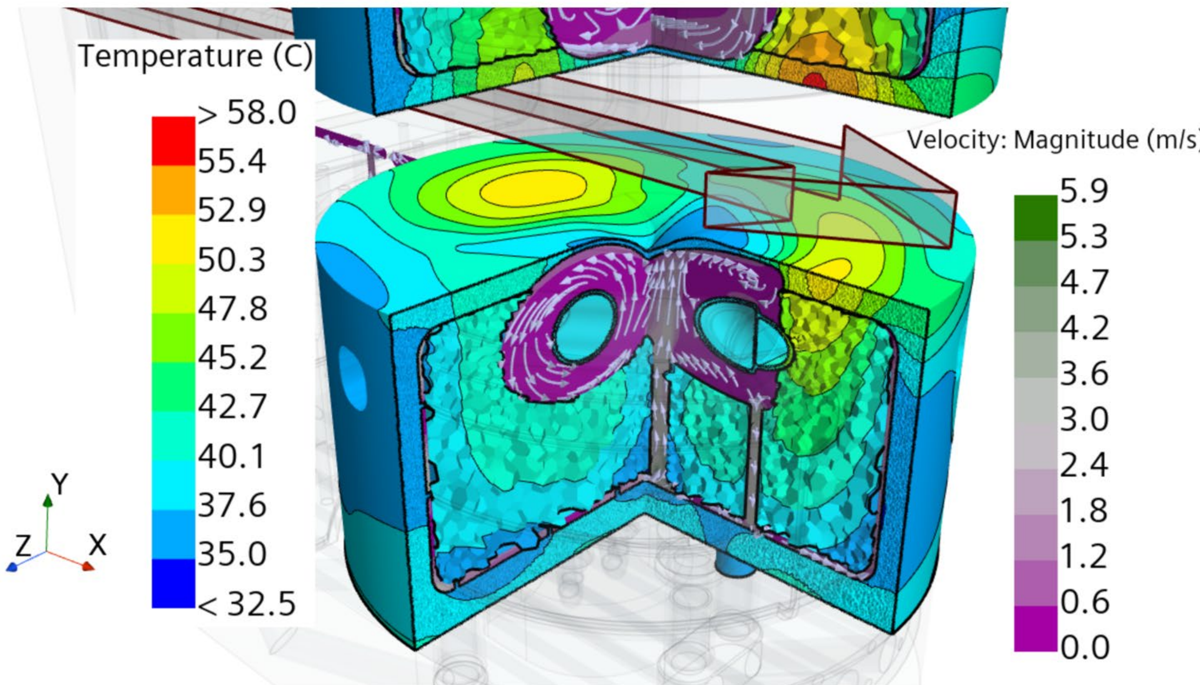

Figure 71. Temperature and velocity distributions in the lower reflector vessel assembly, excluding H_2 loop (cutaway view).

8.2.5 Streamlines and Temperature Distribution of the Entire MRA

Figure 72 shows the temperature distribution and streamlines of the entire MRA, including the hydrogen loop. Figure 73 illustrates the components and the vacuum region between the moderator and aluminum reflector vessels.

Figure 74, Figure 75, Figure 76, Figure 77, and Figure 78 present the temperature distribution of the entire MRA. In these figures, the images on left include all materials (including water and cryogenic hydrogen), whereas the images on the right show only the solid components of the MRA.

Figure 79 shows the interface temperature between the hydrogen and the aluminum vessels. The average interface temperature between the cylindrical vessel and the hydrogen is 20.96 K. The corresponding value for the tube vessel is 21.80 K, which is slightly higher because the cryogenic hydrogen flows sequentially through the cylindrical and tube moderators, and the flow field in the tube moderator is less uniform (Figure 37).

The temperature distributions at the interfaces between the water and the aluminum reflector vessels are shown in Figure 80, Figure 81, and Figure 82.

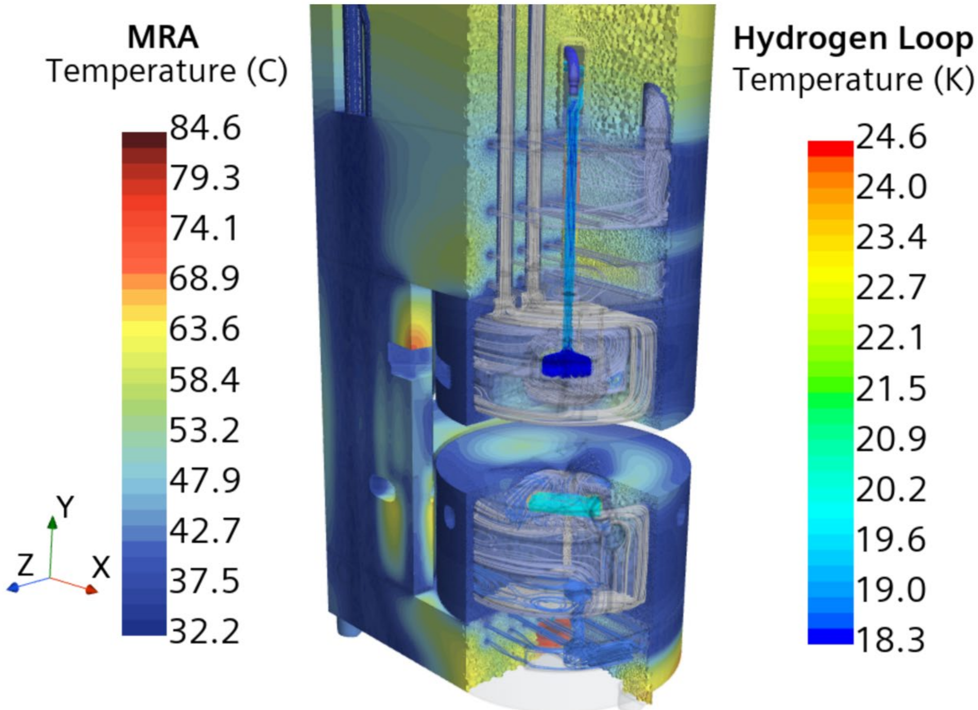

Figure 72. Temperature distribution and streamlines in the entire MRA (cutaway view).

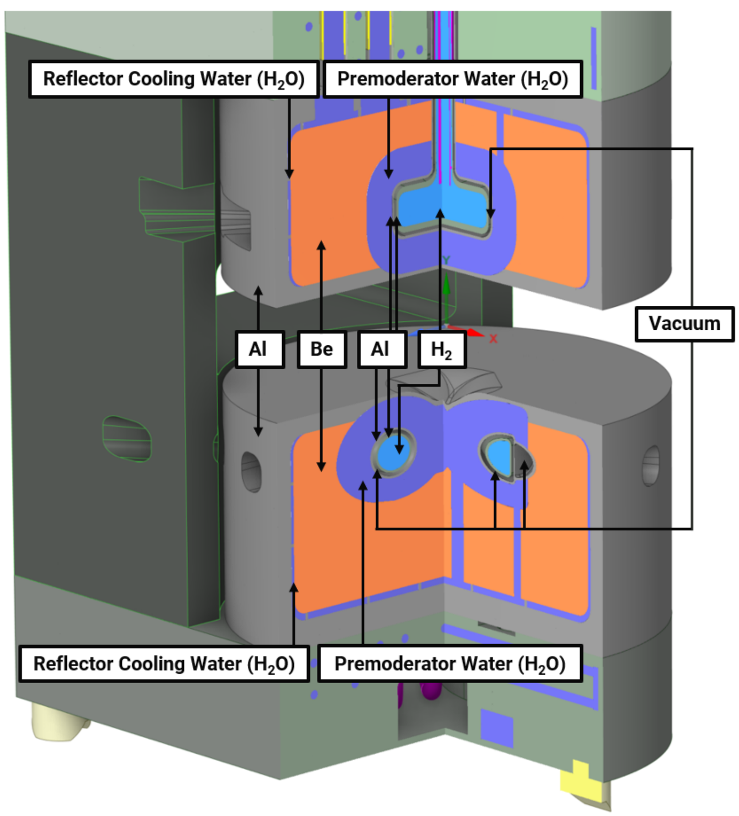

Figure 73. Schematic showing components and the vacuum region in the MRA.

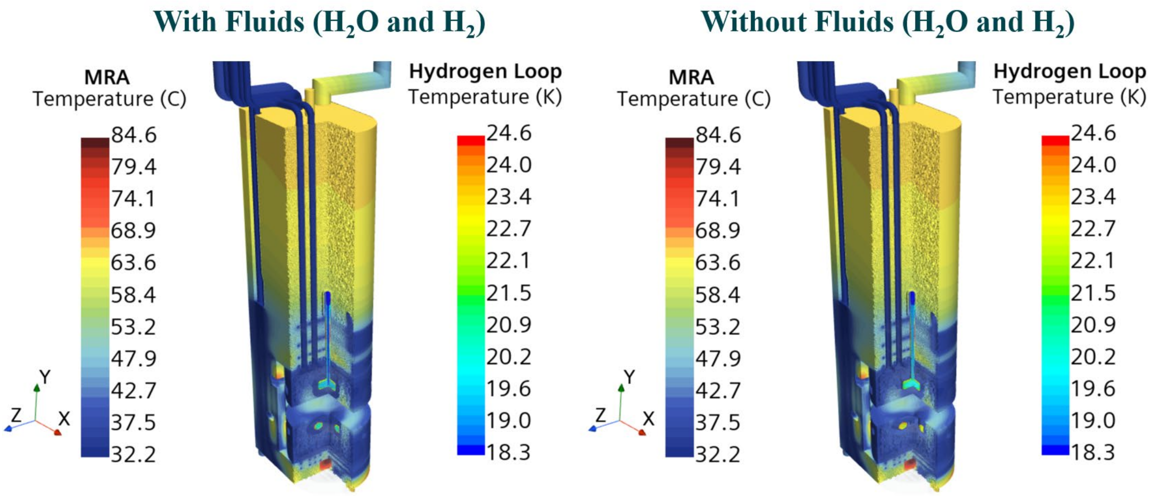

Figure 74. Temperature distribution in the MRA, left with fluids (H_2O and H_2); right: without fluids (H_2O and H_2).

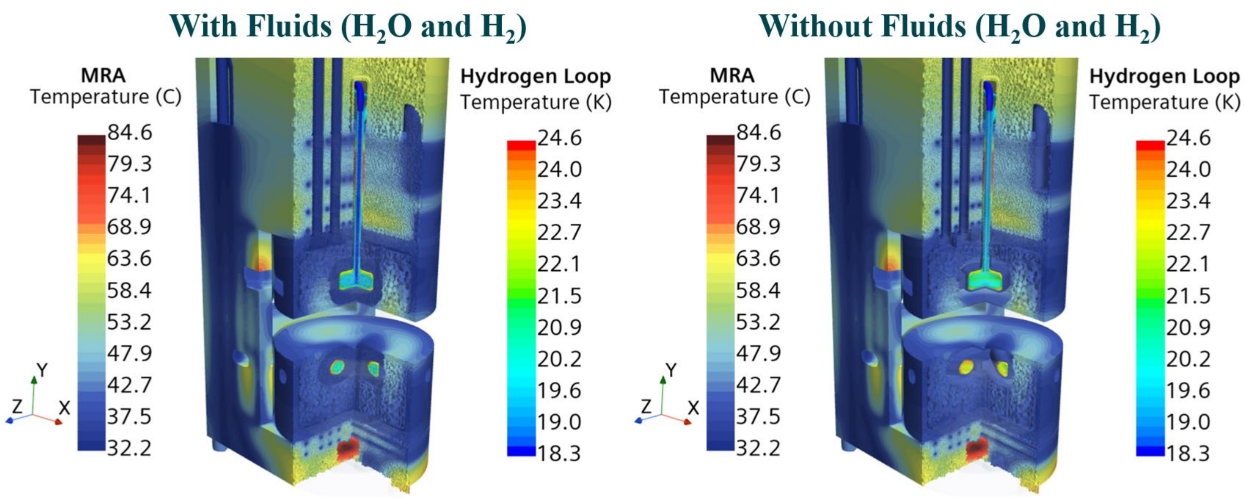

Figure 75. Temperature distribution in the MRA (zoomed view), left with fluids (H_2O and H_2); right: without fluids (H_2O and H_2).

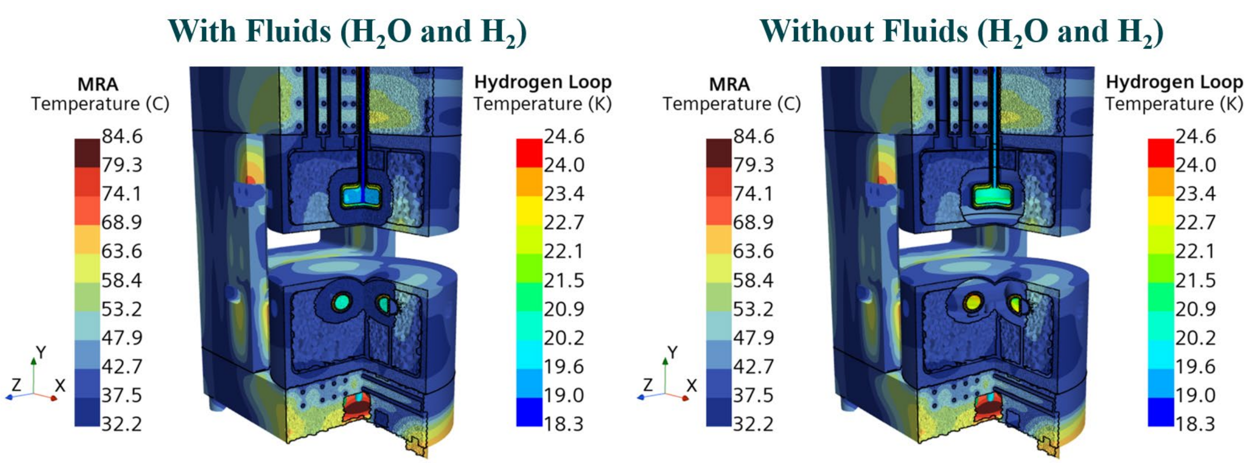

Figure 76. Temperature distribution in the upper and lower MRAs, left with fluids (H_2O and H_2); right: without fluids (H_2O and H_2).

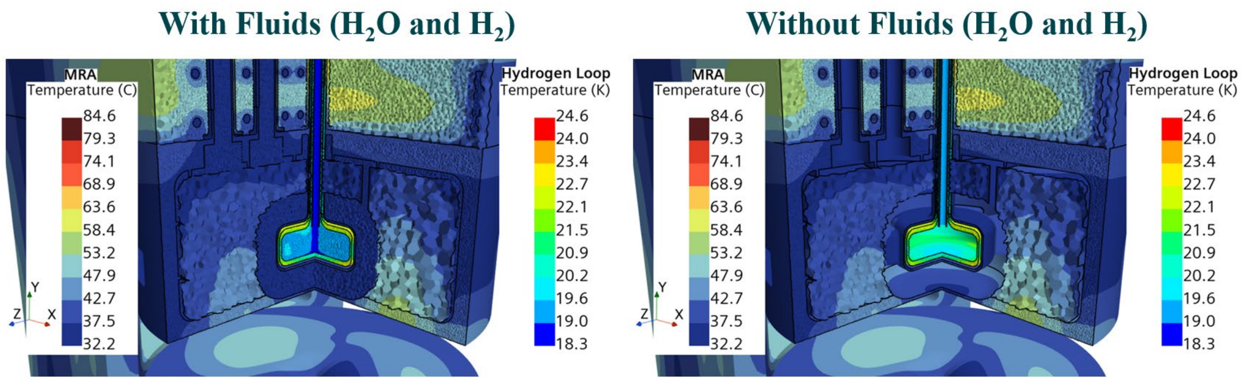

Figure 77. Temperature distribution in the upper MRA, left with fluids (H_2O and H_2); right: without fluids (H_2O and H_2).

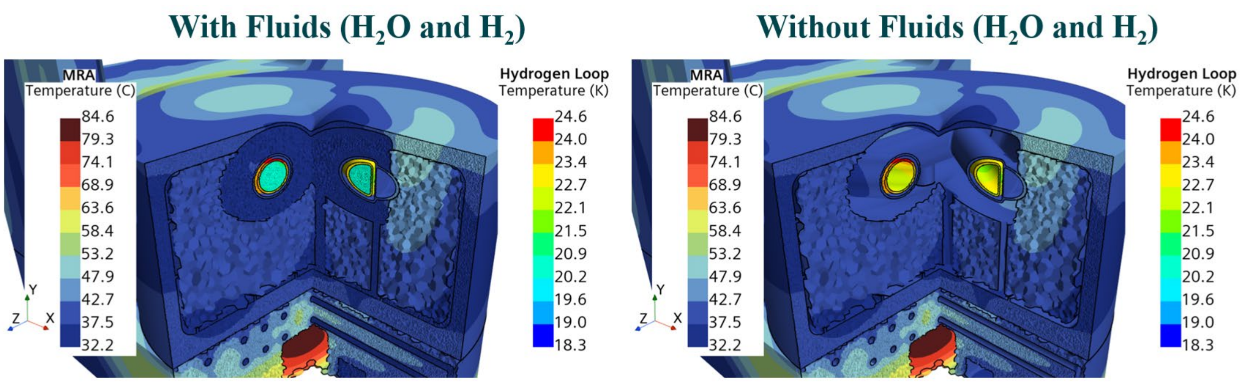

Figure 78. Temperature distribution in the lower MRA, left with fluids (H_2O and H_2); right: without fluids (H_2O and H_2).

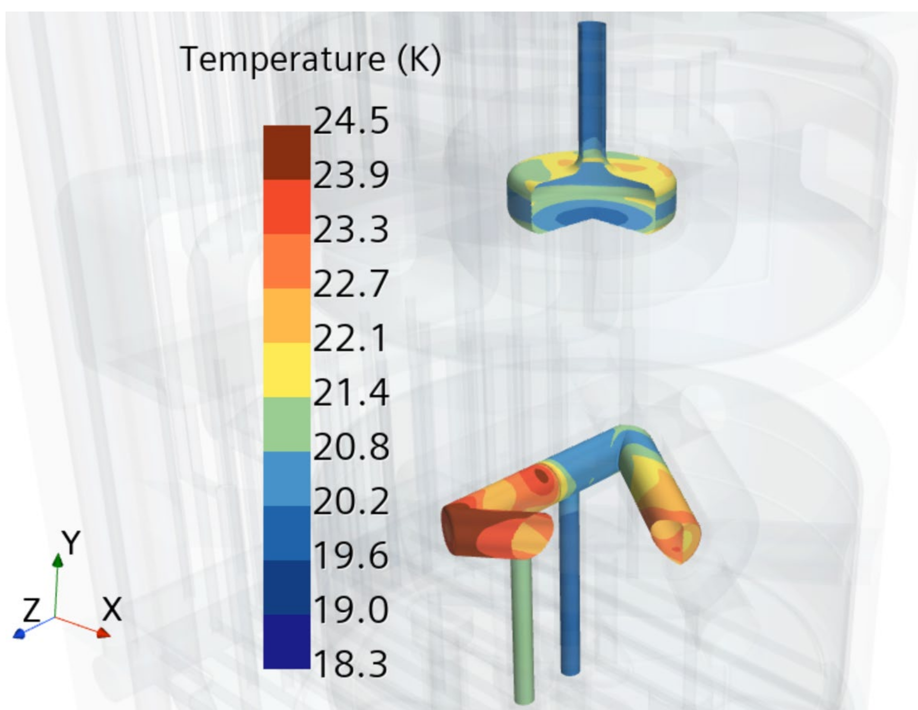

Figure 79. Temperature distribution at the interfaces between hydrogen and the aluminum vessel.

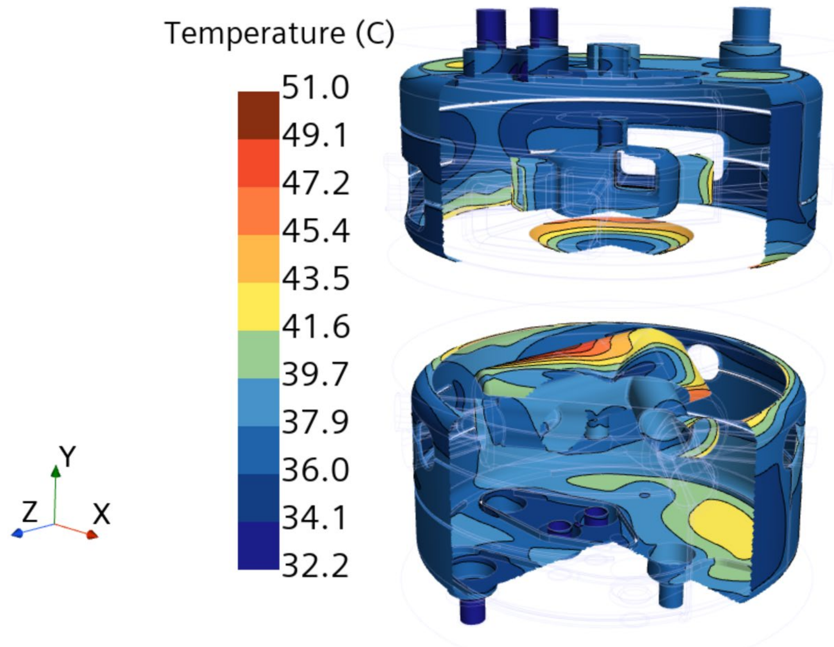

Figure 80. Temperature distribution at the interfaces between water and the aluminum vessels in the upper and lower MRAs.

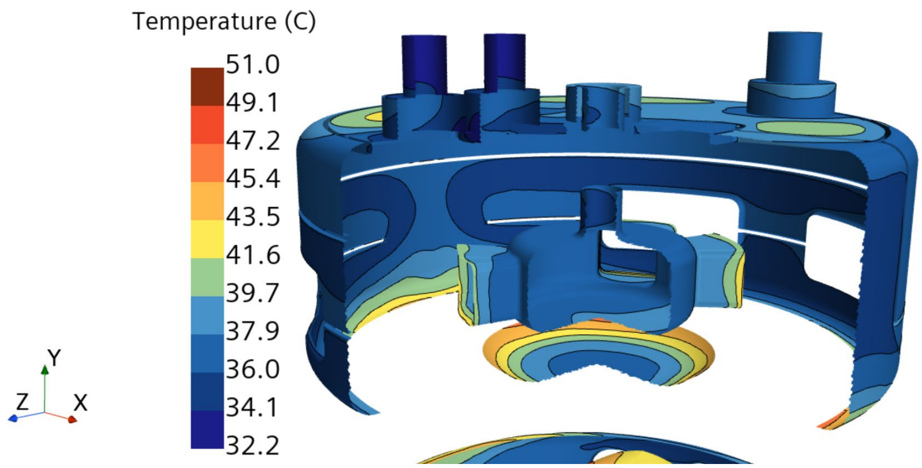

Figure 81. Temperature distribution at the interfaces between water and the aluminum vessel in the upper MRA.

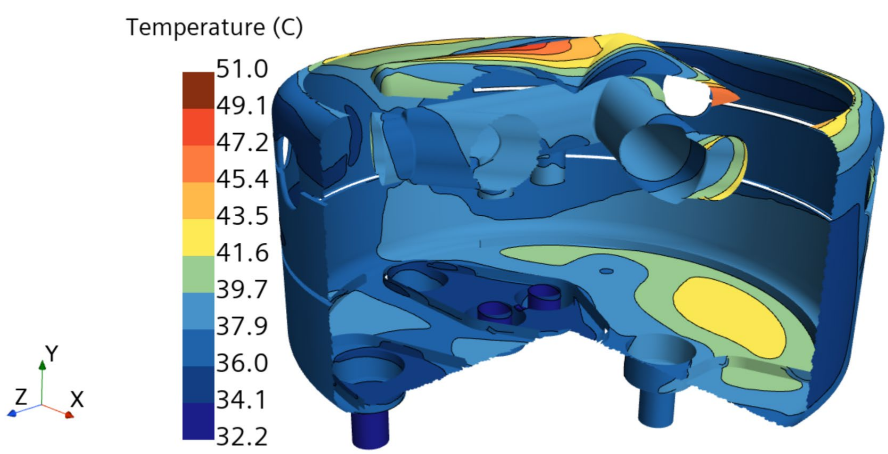

Figure 82.Temperature distribution at the interfaces between water and the aluminum vessel in the lower MRA.

9. AIR ACCUMULATION IN THE LOWER REFLECTOR VESSEL

Air pockets within the water cooling channels may result in local flow blockages or maldistribution, introduce additional thermal resistance due to the low thermal conductivity of air, and lead to localized hot spots within the MRA. Furthermore, air entrainment or accumulation may induce flow instabilities, including oscillations and pressure fluctuations. During the initial filling of the MRA with water, residual air can remain trapped within complex geometries and confined regions, thereby serving as a source for subsequent air accumulation during operation.

Although the water constitutes a single continuous hydraulic domain, its functional role varies spatially. Water adjacent to the liquid hydrogen moderator acts as a premoderator (in addition to serving as coolant), while water located farther from the moderator primarily functions as coolant. Air accumulation within the premoderator region may introduce local void fractions, thereby altering neutron moderation characteristics and potentially degrading neutronic performance. In the reflector cooling regions—particularly within the narrow flow channels shown in Figure 64—air accumulation may impede coolant flow, resulting in local flow maldistribution and reduced heat transfer effectiveness.

Within the STS MRA, no significant stagnant or low-velocity regions are identified in the upper reflector vessel; therefore, air entering this region is expected to be removed by buoyancy-driven venting. In contrast, air accumulating in the lower reflector vessel may become trapped near the upper portion of the tube premoderator region (as all inlets and outlets are located at the bottom of the vessel.) or within the narrower cooling channels of the lower reflector cooling water region (Figure 64), where geometric constraints and local flow conditions may limit effective venting. Accordingly, the lower reflector vessel is identified as the primary region of interest for air accumulation.

This chapter first quantifies the potential volume of air accumulation within the lower reflector vessel and subsequently evaluates its impact on thermal-hydraulic performance through multiphase CFD analysis.

In STAR-CCM+, several multiphase models are available, including the Eulerian Multiphase (EMP), Mixture Multiphase (MMP), Volume of Fluid (VOF), Dispersed Multiphase (DMP), Lagrangian Multiphase (LMP), and Discrete Element Method (DEM) [3]. For the present study, resolving the motion of individual bubbles or bubble-bubble interactions (e.g., coalescence or breakup) is not required. The objective is to quantify the accumulated air volume in the lower reflector vessel and determine whether it remains locally trapped or grows sufficiently to alter the flow field and degrade overall heat transfer performance.

Accordingly, the Volume of Fluid (VOF) method is selected. The VOF method is an interface-capturing approach used to simulate immiscible multiphase flows, such as air-water system. In immiscible flows, each phase forms relatively large, distinct regions separated by a distinct interface. The model tracks the volume fraction of each phase and resolves the interface between them.

Although commonly applied to air-water systems (different substances), the VOF method is also widely used in boiling simulations, where liquid water and steam—despite being the same substance—are separated by a sharp liquid-vapor interface. Therefore, the VOF method is appropriate for analyzing air accumulation and its thermal impact in the lower reflector vessel.

In the VOF approach, a scalar transport equation is solved for the volume fraction of each phase (e.g., air or water). The model tracks the volume fraction of each phase within computational cells to determine the spatial distribution of the phases and the location of the interface. The volume fraction ranges from 0 to 1.

To identify regions of air accumulation, the volume fraction of air (rather than water) is presented in all results in this chapter. A volume faction of air equal to one indicates that the computational cell contains only air, whereas a value of 0 indicates that the cell contains no air (i.e., 100% water). For example, a volume fraction of 0.7 indicates that the cell consists of 70% air and 30% water.

To systematically evaluate the effects of air accumulation, the transient behavior of the two-phase flow in the lower reflector vessel is analyzed under two conditions. First, a transient simulation without heat transfer is performed to isolate the hydrodynamic characteristics of air accumulation, including bubble migration, trapping locations, and void distribution. This step allows the identification of regions prone to persistent air entrainment based solely on flow behavior and geometry.

Subsequently, a transient simulation with conjugate heat transfer is conducted to assess the thermal impact of the accumulated air. This analysis quantifies changes in temperature distribution, local heat transfer performance, and potential hot spot formation resulting from the presence of trapped air.

Together, these two analyses provide a comprehensive understanding of both the accumulation mechanism and its thermal consequences in the lower reflector vessel.

9.1 TRANSIENT RESULTS WITHOUT HEAT TRANSFER

Two cases are analyzed in the section. In the first case, 23.4% of the fluid volume in the lower reflector vessel—where water serves both as premoderator water (inner region) and reflector cooling water (outer region)—is assumed to be initially occupied by air accumulated at the top of the domain. This case evaluates whether the water in the lower reflector vessel can successfully vent the trapped air during normal operation, with a flow rate of 7.5 GPM entering the premoderator water region and 7.5 GPM entering the reflector water region (Figure 9).

The second case represents an extreme condition, in which 98.7% of the fluid region is assumed to be initially occupied by air. This scenario is used to determine whether any dead zones exist within the lower reflector vessel that could permanently trap air.

Figure 83 shows the initial condition for the case with 23.4% of the fluid volume initially occupied by air. The total air volume and mass as functions of time are presented in Figure 84 and Figure 85, respectively. The simulation results indicate that after one minute of normal operation, approximately 4 cm^3 and 0.01 g of air remain in the system. Figure 86 illustrates the relative location of the accumulated air, and Figure 87 shows the air accumulation zone together with the corresponding streamlines. As observed, the remaining air accumulates in a low-velocity region where two fluid streams converge from opposite directions.

Similarly, Figure 88 presents the initial condition for the case with 98.7% of the fluid volume initially occupied by air. The corresponding air volume and mass over time are shown in Figure 89 and Figure 90, respectively. Figure 91 again illustrates the air accumulation zone together with the surrounding streamlines. Even with 98.7 % of the fluid volume initially filled with air, after 100 seconds of normal operation, only approximately 4.5 cm^3 and 0.015 g of air remain in the system.

Despite the significantly different initial conditions, Figure 87 and Figure 91 demonstrate similar behavior of the remaining air pocket. Rather than remaining stationary, the air pocket oscillates within this region, as observed in the simulation animations. Given the very small residual air volume, significant degradation of heat transfer performance in the lower reflector vessel is not expected.

A Comparison of the lower reflector air volume and mass over time for the two initial conditions (23.4% and 98.7%) is summarized in Figure 92 and Figure 93, respectively.

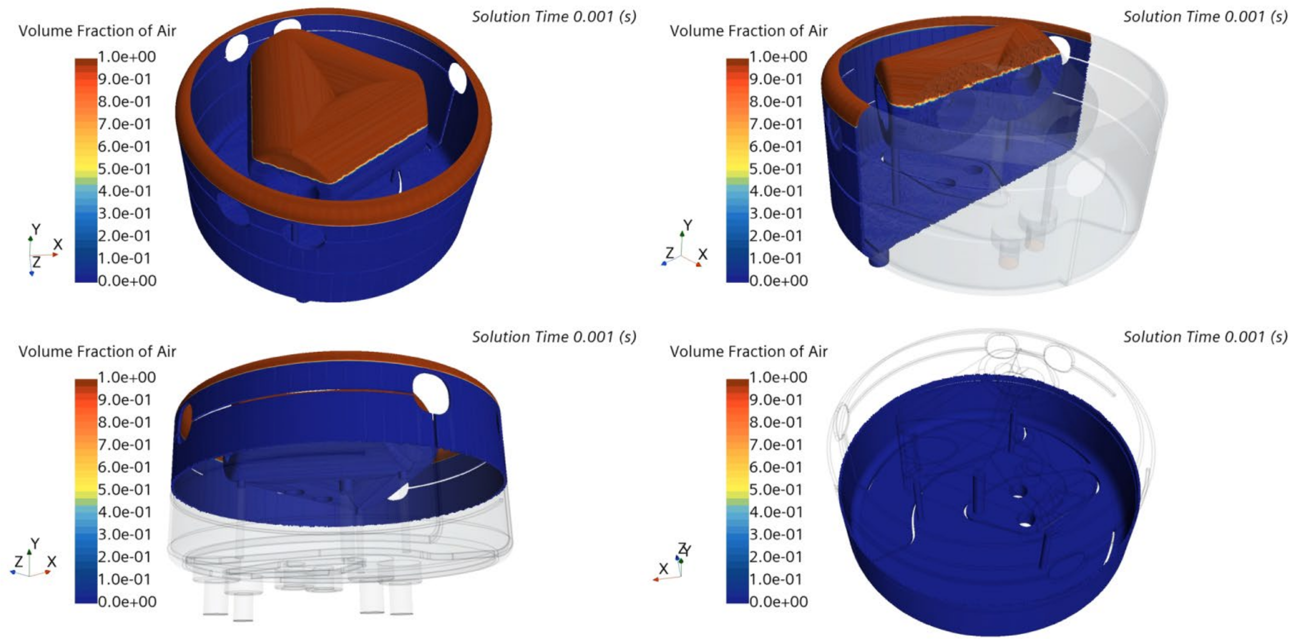

Figure 83. Initial condition: 23.4% of the volume is air.

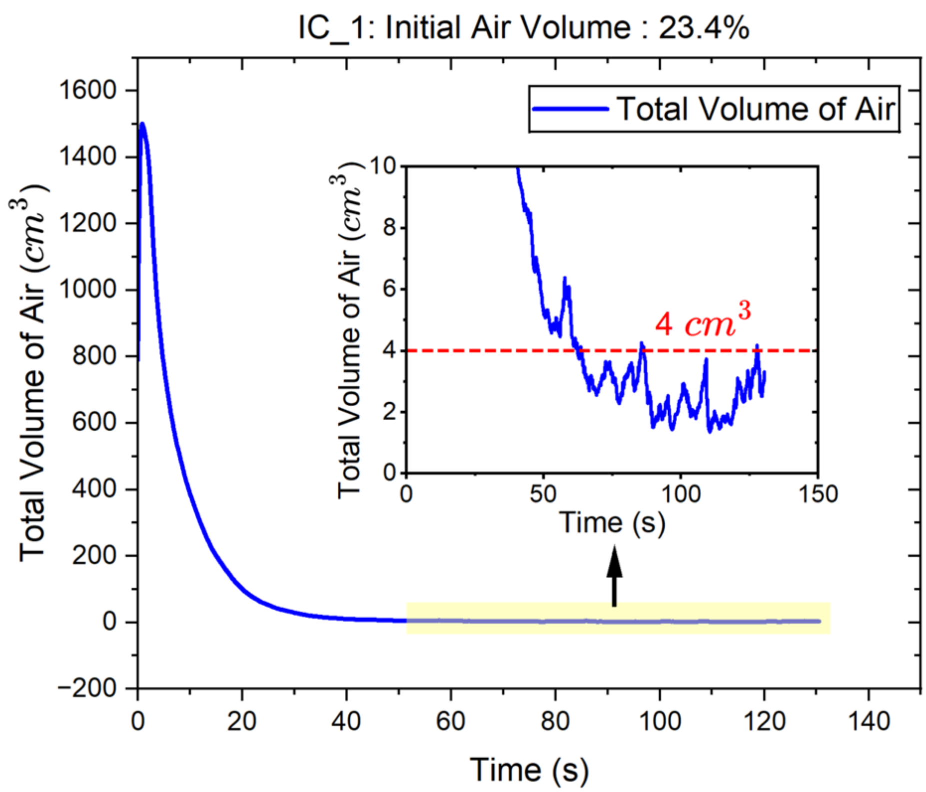

Figure 84. Air volume in the lower reflector vessel over time (initial air volume: 23.4%).

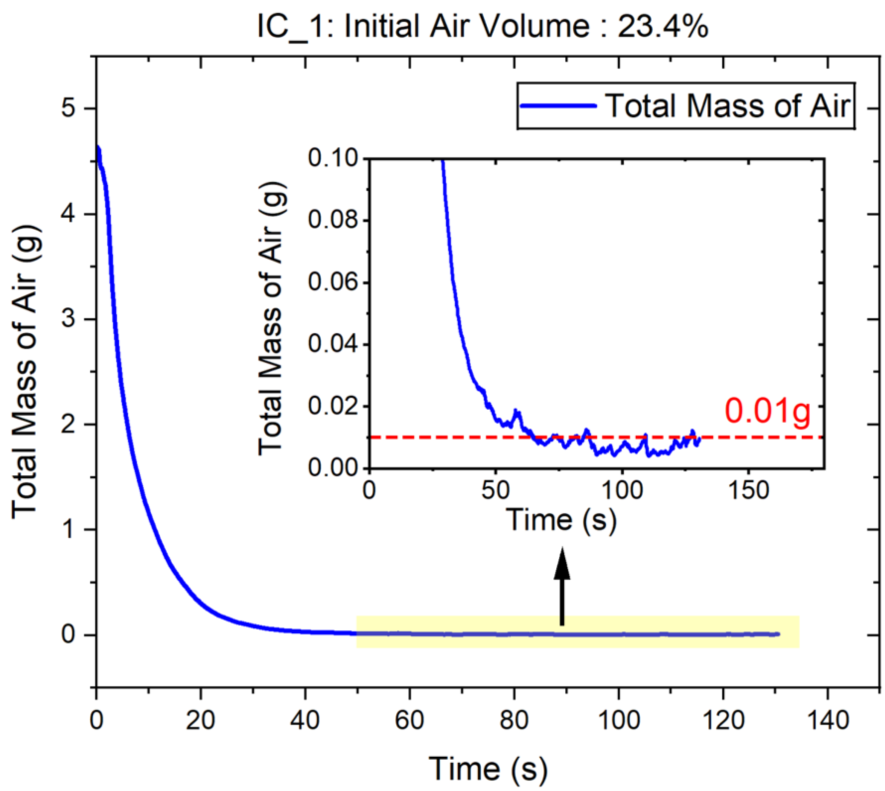

Figure 85. Air mass in the lower reflector vessel over time (initial air volume: 23.4%).

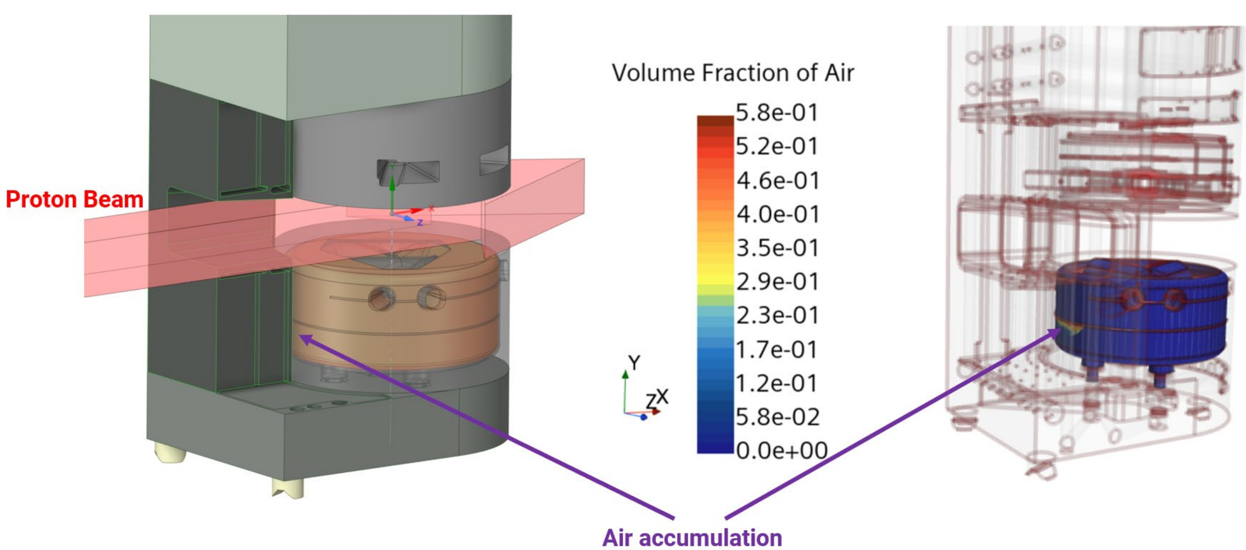

Figure 86. Identified air accumulation zone within the lower reflector vessel.

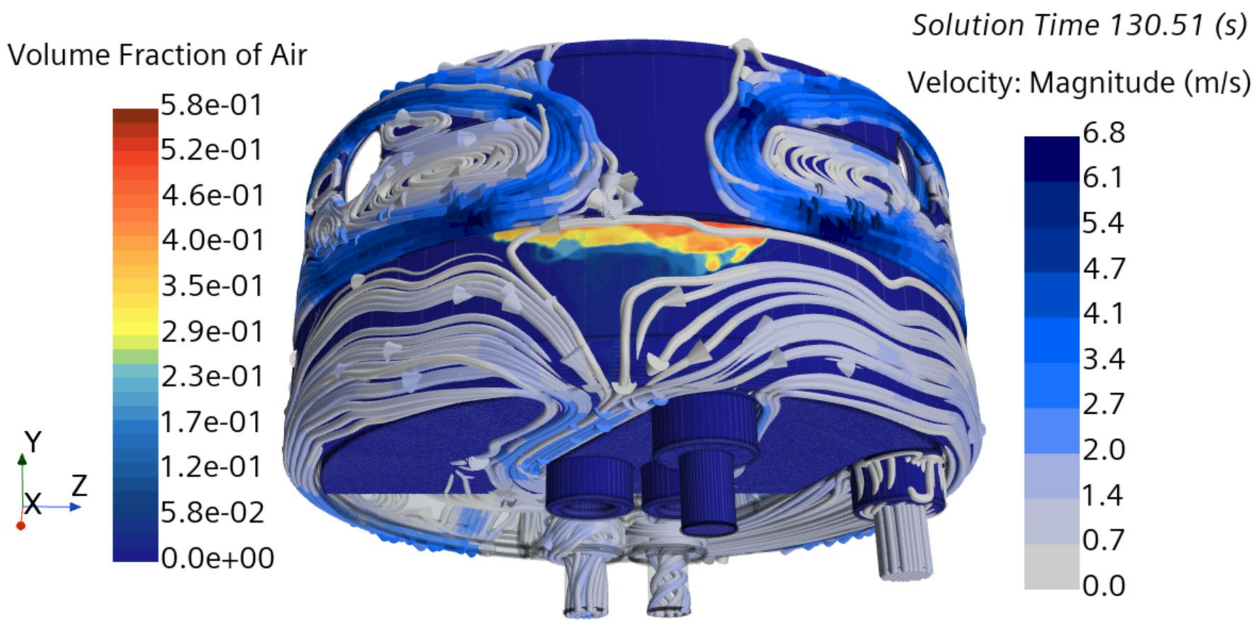

Figure 87. Air accumulation zone and flow streamlines (initial air volume: 23.4%).

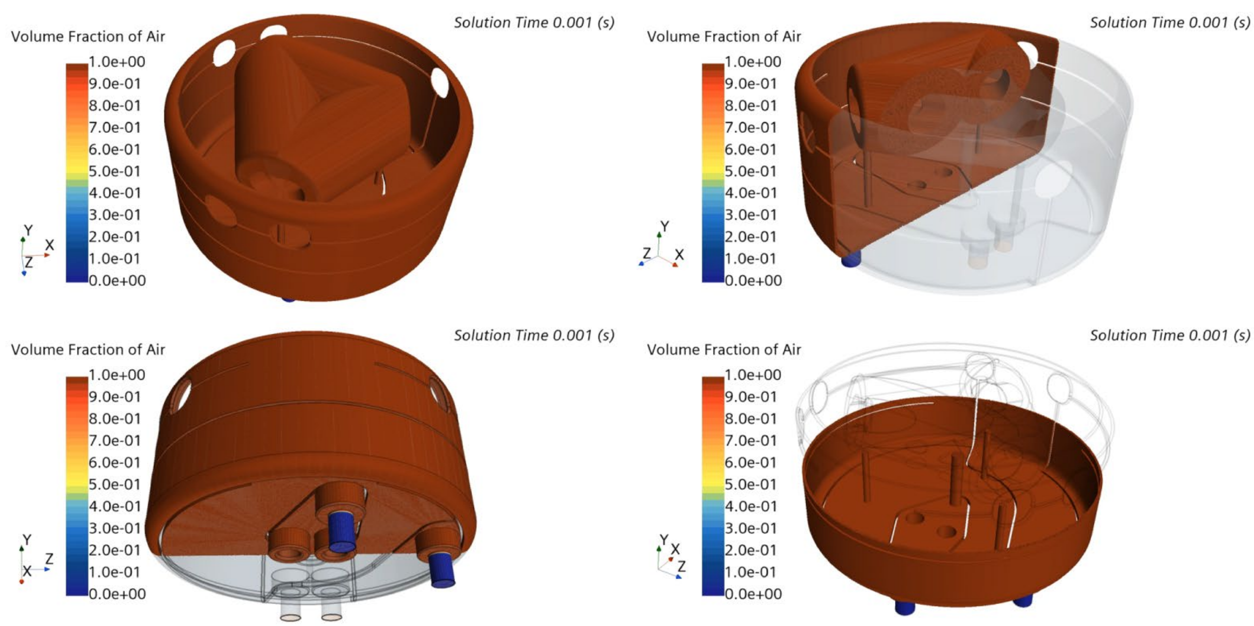

Figure 88. Initial condition: 98.7% of the volume is air.

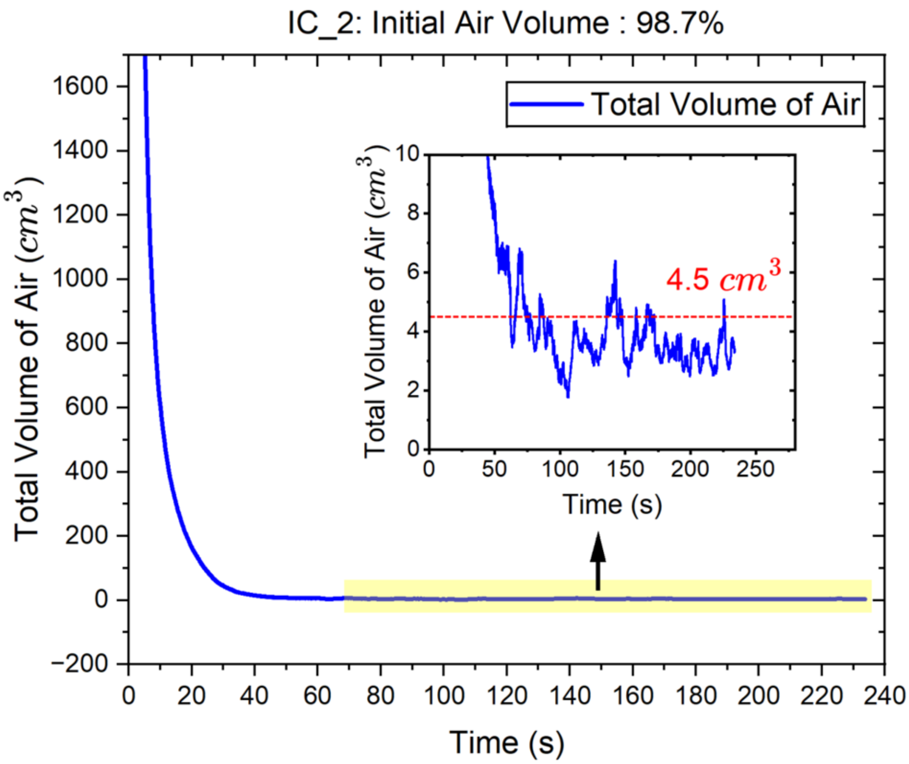

Figure 89. Air volume in the lower reflector vessel over time (initial air volume: 98.7%).

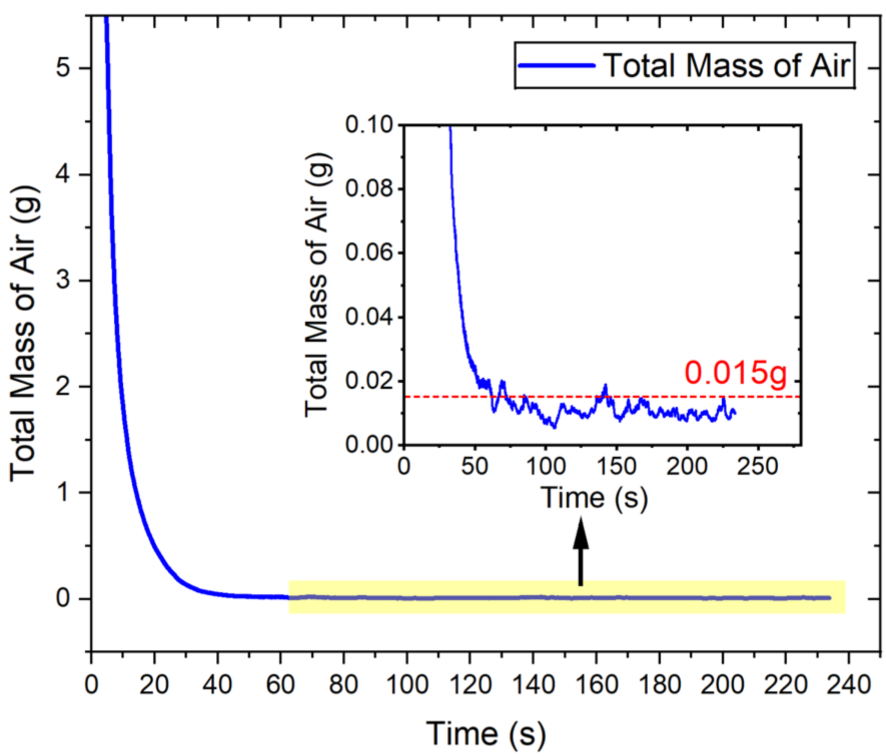

Figure 90. Air mass in the lower reflector vessel over time (initial air volume: 98.7%).

Draft. Not approved for public release.

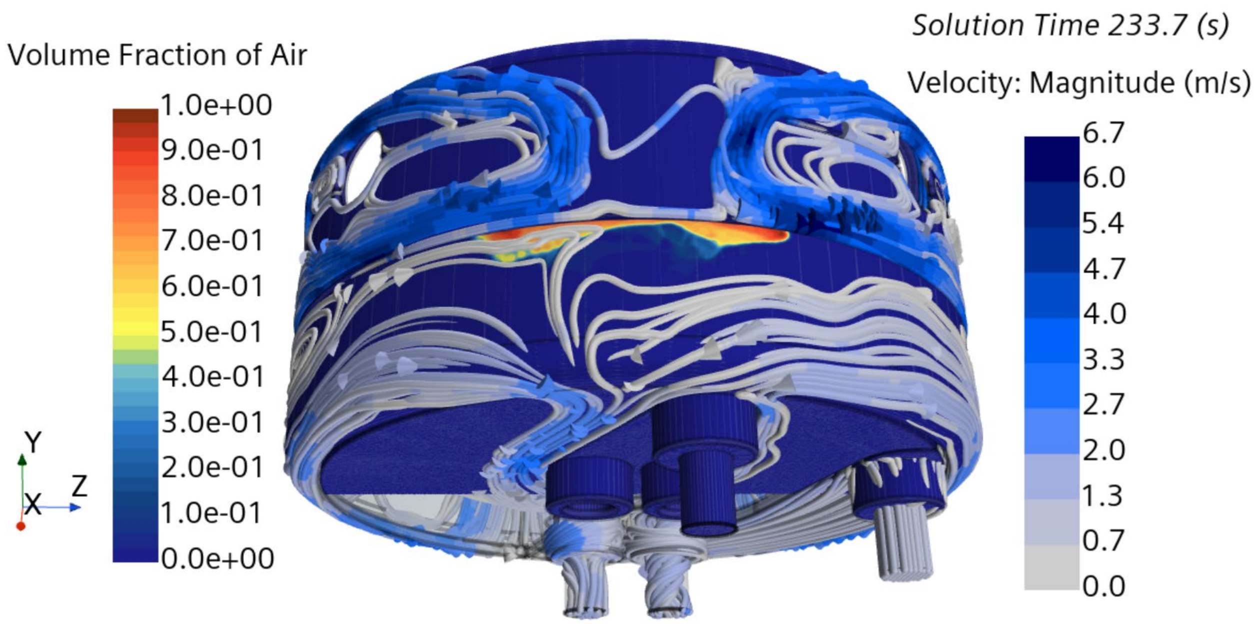

Figure 91. Air accumulation zone and flow streamlines (initial air volume: 98.7%).

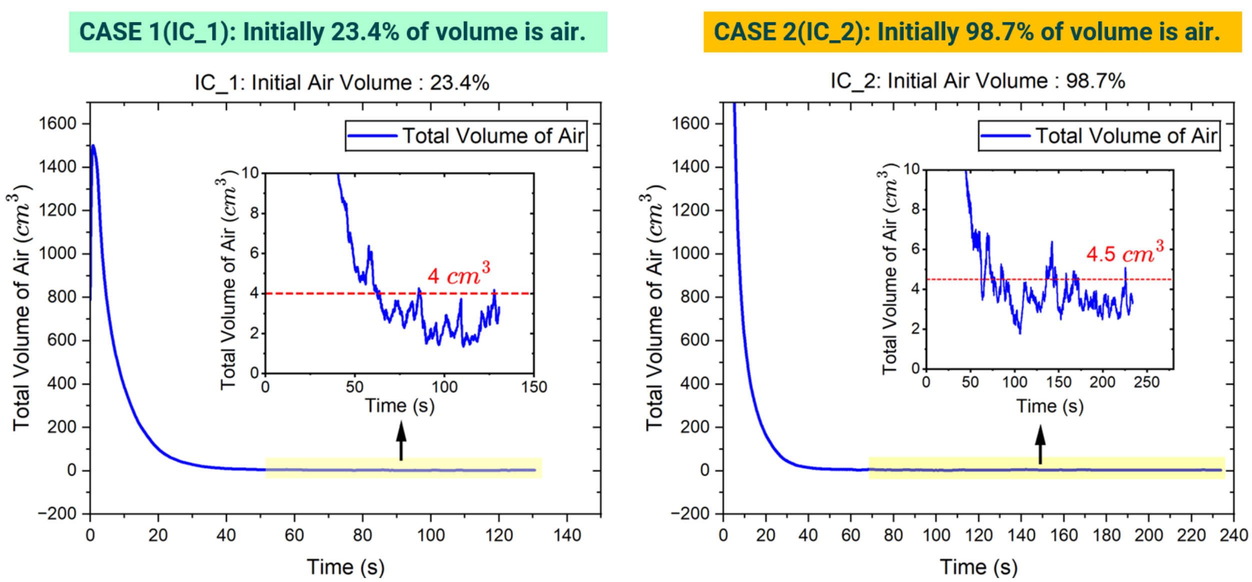

Figure 92. Comparison of lower reflector air volume over time for two initial conditions (23.4% vs. 98.7%).

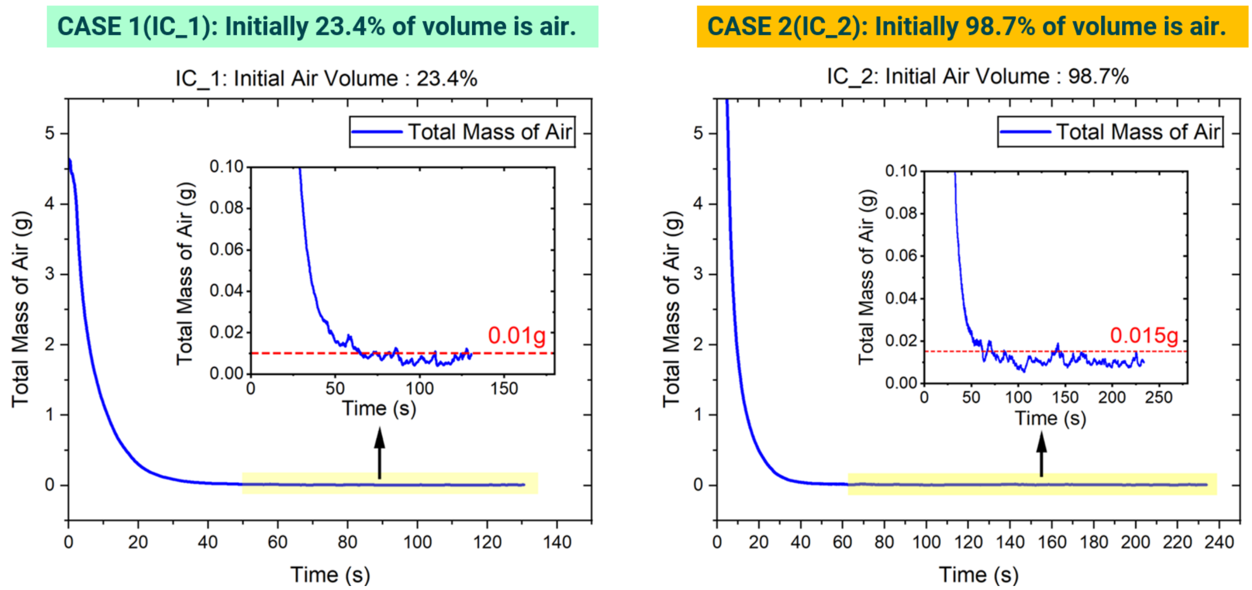

Figure 93. Comparison of lower reflector air mass over time for two initial conditions (23.4% vs. 98.7%).

9.2 TRANSIENT RESULTS WITH HEAT TRANSFER

To evaluate the impact of accumulated air in the lower reflector vessel, the extreme case in which 98.7% of the fluid region is initially occupied by air is analyzed. A fixed time step of 0.01 s with a maximum of 20 inner iterations per time step is used for this simulation. Second-order schemes are employed for temporal discretization, gradient evaluation, and convection terms. A first-order High Resolution Interface Capturing (HRIC) is used in the VOF model.

The simulation is initially performed with the energy equation disabled until 243 s, allowing most of the accumulated air to be vented from the lower reflector vessel. This approach reflects the actual operating sequence, in which the cooling system is activated and stabilized prior to proton beam injection. At t = 243 s, the energy equation is activated to simulate the heat deposition under normal operating conditions.

A comparison between Figure 93 and Figure 94 confirms that even under this extreme situation, the remaining air volume in the lower reflector vessel is approximately 4.5 cm^3 (0.015 g). Figure 95 shows the time evolution of the lower reflector temperature. The peak temperatures of aluminum, beryllium, and water reach 51°C, 50°C, and 49°C, respectively. These values are very close to the normal operating temperatures, confirming that air accumulation does not pose a thermal concern for the STS lower reflector vessel.

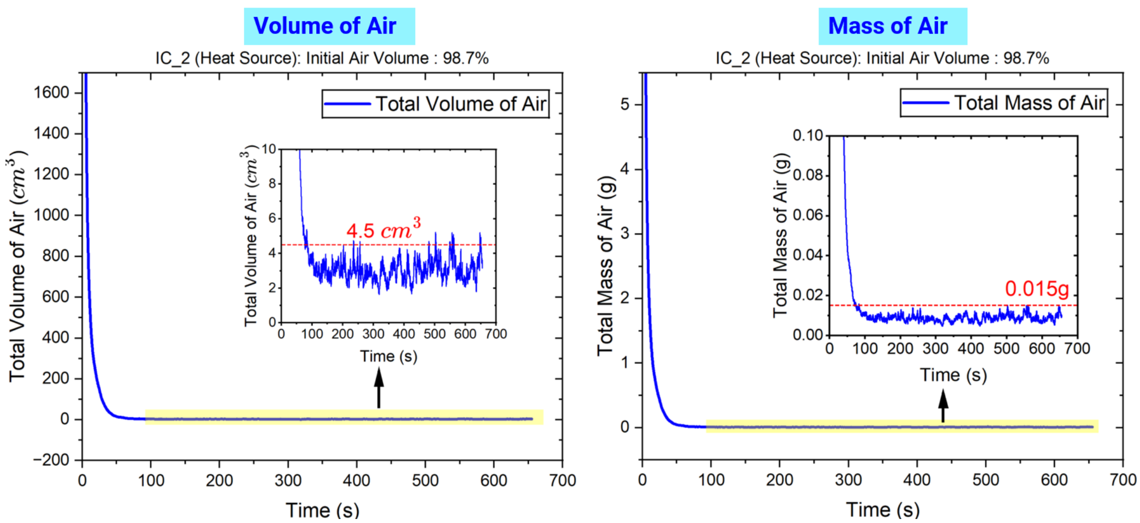

Figure 94. Time evolution of air volume (left) and air mass (right) in the lower reflector vessel with heat transfer.

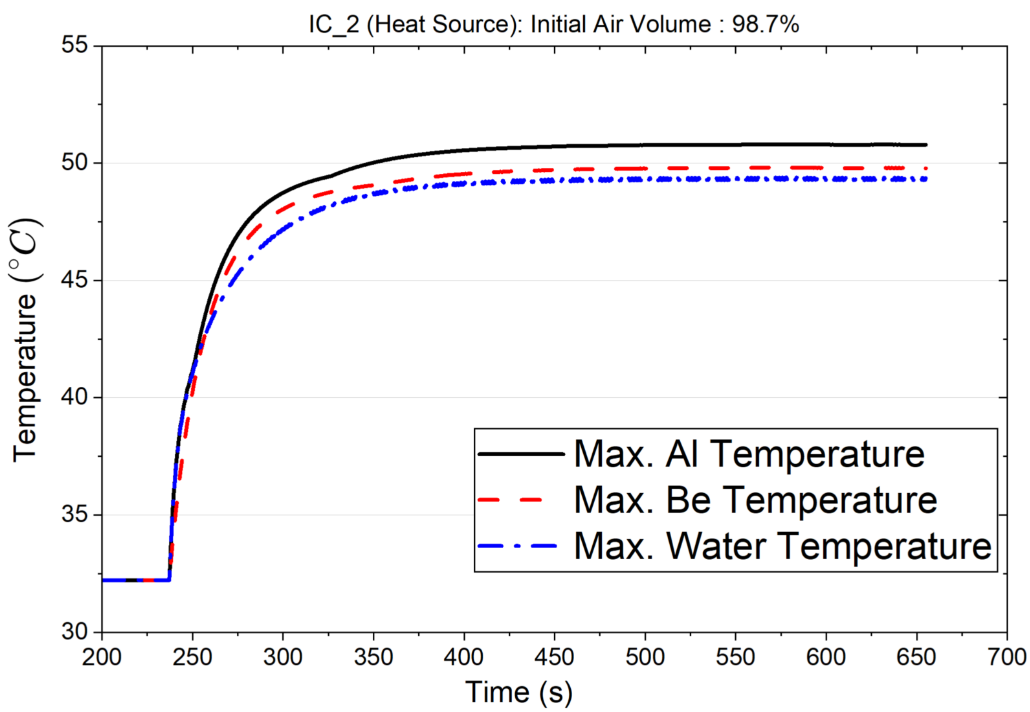

Figure 95. Time evolution of the lower reflector assembly temperature for the case with air accumulation.

10. REQUIREMENT SATISFACTION

Satisfactions of thermal hydraulics requirements documented on Codebeamer are summarized in Table 10.

Table 10. Requirement satisfaction of MRA.

Requirement Name	Codebeamer ID	Requirement	CFD Result	Status
MRA Water Loop				
MRA Aluminum Temperature Requirement	2325	The MRA aluminum 6061-T6 structures shall have a maximum operating temperature of 100 °C.	73.1 °C	Pass
MRA Stainless Steel Temperature Requirement	2326	The MRA stainless steel structures shall have a maximum operating temperature of 200 °C.	84.6 °C	Pass
MRA Beryllium Temperature Requirement	2327	The MRA beryllium shall have a maximum operating temperature of 100 °C.	54.9 °C	Pass
MRA Water Temperature Requirement	2328	The MRA cooling water shall have a maximum temperature of 100 °C.	51.0 °C	Pass
MRA Upper Premoderator Pressure Drop Requirement	2362	The MRA upper premoderator water loop shall have a pressure drop of less than 15 psi at 7.5 gpm and 32.2 °C inlet temperature.	5.20 psi	Pass
MRA Lower Premoderator Pressure Drop Requirement	2363	The MRA lower premoderator water loop shall have a pressure drop of less than 15 psi at 7.5 gpm and 32.2 °C inlet temperature.	6.86 psi	Pass
MRA Upper Reflector Pressure Drop Requirement	2364	The MRA upper reflector water loop shall have a pressure drop of less than 15 psi at 7.5 gpm and 32.2 °C inlet temperature.	9.65 psi	Pass
MRA Lower Reflector Pressure Drop Requirement	2365	The MRA lower reflector water loop shall have a pressure drop of less than 15 psi at 7.5 gpm and 32.2 °C inlet temperature.	9.55 psi	Pass
MRA Backbone Pressure Drop Requirement	2366	The MRA backbone water loop shall have a pressure drop of less than 15 psi at 15 gpm and 32.2 °C inlet temperature.	4.29 psi	Pass
MRA Hydrogen Loop				
MRA Hydrogen Loop Pressure Drop Requirement	2356	The MRA hydrogen loop pressure drop shall be less than 0.15 bar @ 0.5 l/s and 18.34 K.	0.105 bar	Pass
MRA Moderator Hydrogen Density Requirement	2888	The hydrogen in both moderators shall have a minimum average density of 72.0 kg/m^3.	Upper Cylindrical Moderator: 73.185 kg/m^3 Lower Tube Moderator: 72.353 kg/m^3	Pass
MRA Moderator Hydrogen Maximum Temperature Requirement	2889	The hydrogen temperature shall at no point in the moderators exceed 32 K.	24.5 K	Pass

11. CONCLUSIONS

A comprehensive thermal-hydraulic assessment of the Moderator Reflector Assembly (MRA) for the Second Target Station (STS) at Oak Ridge National Laboratory was performed using CFD simulations under normal operating conditions. The analysis included the hydrogen moderator loop, reflector vessel assemblies, backbone structure, shield block, and a transient evaluation of potential air accumulation in the lower reflector vessel.

The results confirm that **all thermal-hydraulic requirements defined in the MRA requirements document (S03040000-SR0001) are satisfied**, as summarized in Table 9.

The hydrogen loop demonstrates stable performance with a total pressure drop of **0.105 bar**, meeting the requirement of less than 0.15 bar. The maximum hydrogen temperature is **24.5 K**, which remains well below the 32 K limit, providing a substantial thermal margin relative to the critical temperature of hydrogen. The average hydrogen density in both moderators exceeds the minimum requirement of 72 kg/m^3, with values of **73.185 kg/m^3 (upper cylindrical moderator)** and **72.353 kg/m^3 (lower tube moderator)**. Thermal behavior is effectively quasi-steady, as the calculated temperature rise per residence time remains below **1 K** (0.75 K in the cylindrical moderator and 0.96 K in the tube moderator), corresponding to an estimated temperature rise per pulse of approximately **0.08 K**, indicating negligible transient fluctuation and stable moderator operation under pulsed beam loading.

The water cooling system and structural components also satisfy all performance requirements. All coolant pressure drops remain below the **15 psi limit**, with the highest value occurring in the reflector loops (up to 9.65 psi). Peak temperatures remain within allowable limits, including:

- Aluminum structures: **73.1°C** (< 100°C limit)
- Beryllium: **54.9°C** (< 100°C limit)
- Steel structures: **84.6°C** (< 200°C limit)
- Cooling water: **51.0°C** (< 100°C limit)

The reflector vessel assemblies and backbone temperature distributions indicate effective heat removal and acceptable thermal gradients. Design improvements from the preliminary configuration, including optimized cooling channel layouts and replacement of SS316 with A36 steel in the shield block, result in improved thermal uniformity and reduced risk of thermally induced misalignment of neutron beam ports.

Transient multiphase simulations of the lower reflector vessel indicate that air introduced during filling or operation is effectively removed under normal flow conditions. Even under extreme initial conditions, only a negligible residual air volume (~4.5 cm^3) remains, which is confined to a localized low-velocity region. Conjugate heat transfer analysis confirms that this residual air has no significant impact on temperature distribution or heat transfer performance.

Overall, the CFD analyses demonstrate that the STS MRA design satisfies all thermal-hydraulic requirements with adequate safety margins. The system exhibits stable hydrogen moderator performance, effective cooling of structural components, and robust resilience against potential air accumulation, thereby ensuring reliable operation and supporting consistent cold neutron production for the STS.

REFERENCES

[1] I. Remec and F. X. Gallmeier, “Neutronics analyses for the conceptual design of the SNS Second Target Station,” *J. Neutron Res.*, vol. 22, no. 2–3, pp. 265–273, Oct. 2020, doi: 10.3233/JNR-200165.

[2] *SpaceClaim 2024 R2*. [Online]. Available: https://www.ansys.com/products/3d-design/ansys-spaceclaim

[3] *Simcenter STAR-CCM+ 2306.0001*. [Online]. Available: https://www.siemens.com/en-us/products/simcenter/fluids-thermal-simulation/star-ccm/

APPENDIX A. MESH INDEPENDENCE STUDY

Results from several mesh configurations were compared to ensure that sufficient resolution was used to capture the significant phenomena in the MRA while maintaining acceptable numerical errors and reasonable computational cost. Figure 96 shows the different mesh configurations used in the mesh independence study, and Figure 97 provides a close-up view of the meshes near the vacuum gap between the moderator and reflector. The numbers of mesh elements for Mesh_1, Mesh_2, Mesh_3, and Mesh_4 are 20.3, 36.5, 81.2, and 92.6 million, respectively. The results from Mesh_4 were used as a reference for the error estimates.

The peak temperatures and pressure drop in the hydrogen loop for the different mesh configurations are summarized in Table 11, and the corresponding percentage errors are shown in Table 12. The errors in the predicted peak temperatures of hydrogen and aluminum vessel are less than 1 % for all mesh configurations. For the pressure drop, the difference between the coarsest and finest meshes is approximately 2%. Although the coarsest mesh already provides reasonable predictions for the hydrogen loop, a finer mesh is required to capture temperature profiles with sufficient resolution for the thermal stress analysis.

Similarly, the peak temperatures and pressure drop in the remaining MRA components are shown in Table 13, with percentage errors summarized in Table 14. The MRA contains five water loops sharing a common outlet at the top. Water loop_1, representing flow into the upper reflector water domain with narrower cooling channels, exhibits the highest pressure drop among all loops and is therefore selected for reporting in the mesh independence study. As shown in Table 14, the difference in peak temperatures between the coarsest and finest meshes is less than 4%. However, the pressure drop predicted using the coarsest mesh if 8.2% off, which is insufficient. The Mesh_3 configuration predicts both peak temperatures and pressure drop within 1% of the finest mesh and is thus considered sufficient; results from this mesh are used for the MRA FDR report.

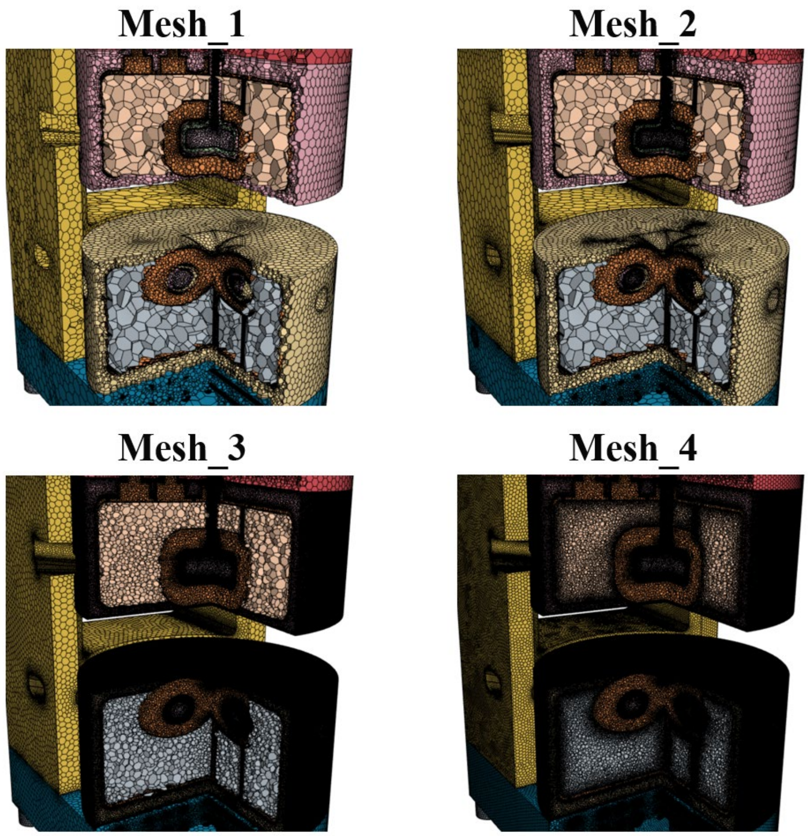

Figure 96. Different mesh configurations used in the mesh independence study.

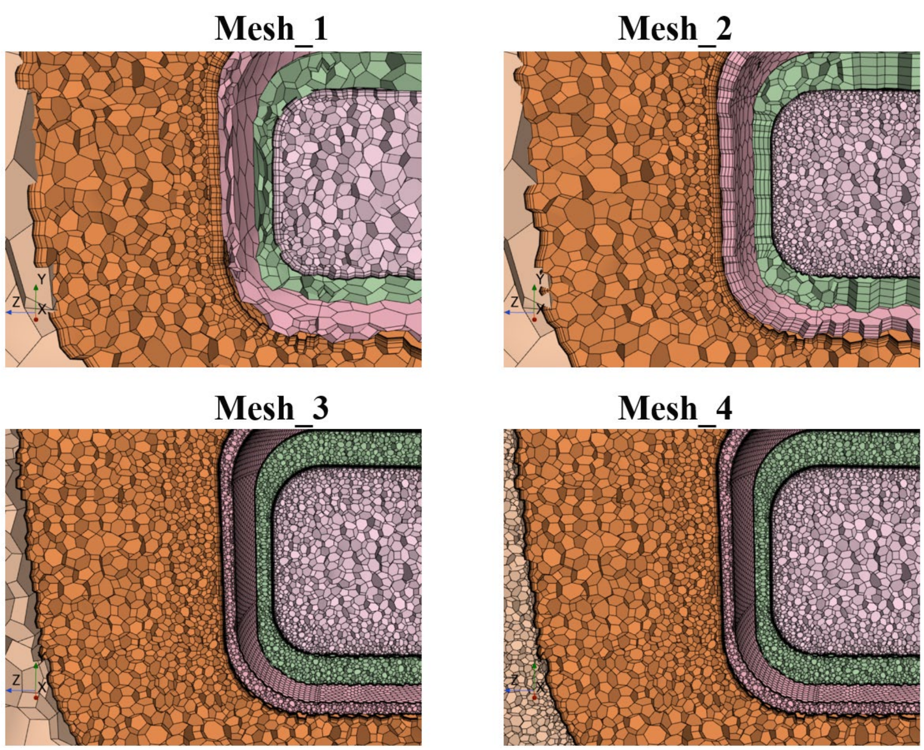

Figure 97. Close-up view of mesh configurations in the vicinity of the vacuum gap between the moderator and reflector.

Table 11. Temperatures and pressure drop in the hydrogen loop, obtained for the mesh independence study.

Mesh	H_2 (K)	Al (K)	Invar (K)	ΔP (psi)
M1	24.68	24.81	21.44	0.11
M2	24.39	24.48	21.51	0.10
M3	24.53	24.63	21.34	0.10
M4	24.54	24.63	21.34	0.10

Table 12. Percentage errors relative to the finest mesh (M4) for the H_2 loop.

Mesh	H_2 (%)	Al (%)	Invar (%)	ΔP (%)
M1	0.54	0.69	0.48	2.06
M2	0.64	0.63	0.81	0.60
M3	0.04	0.04	0.00	0.10
M4	0.00	0.00	0.00	0.00

Table 13. Temperatures and pressure drop in the MRA, excluding the H_2 loop, obtained for the mesh independence study.

Mesh	Be (°C)	Al (°C)	A36 (°C)	SS316 (°C)	Water (°C)	ΔP (psi)
M1	56.73	71.29	66.61	83.29	50.18	8.84
M2	56.31	73.25	65.41	84.68	50.37	9.07
M3	54.93	73.15	65.25	84.55	51.00	9.65
M4	54.69	73.18	65.18	84.52	50.77	9.64

Table 14. Percentage errors relative to the finest mesh (M4) for the MRA, excluding the H_2 loop.

Mesh	Be (%)	Al (%)	A36 (%)	SS316 (%)	Water (%)	ΔP (%)
M1	3.72	2.58	2.19	0.01	0.01	8.24
M2	2.95	0.10	0.35	0.00	0.01	5.83
M3	0.44	0.04	0.10	0.00	0.00	0.15
M4	0.00	0.00	0.00	0.00	0.00	0.00

APPDNDIX B. IMPACT OF THERMAL CONTACT RESISTANCE

Figure 98 illustrates the thermal contacts between the blocks in the MRA backbone. Assuming the core vessel operates in helium mode, the thermal contact resistance can be calculated using the following relation:

$$R = L/k, \tag{4}$$

where R is the thermal contact resistance, L is the size of the gap, and k is the thermal conductivity of helium.

Two helium gap sizes—0.1 mm and 1.0 mm—were investigated, as summarized in Table 15 and Table 16. As shown in Figure 99Figure 98, the peak stainless steel temperatures corresponding to the cases of perfect contact, 0.1mm, and 1.0mm helium gaps are 117.26°C, 117.32°C, and 120.95°C, respectively.

Since the impact of the helium gap size on temperature is less than 4°C, it is reasonable to assume perfect thermal contact between the blocks in the MRA backbone for all subsequent thermal analyses.

It should be noted that the results presented in Figure 99 are based on the CAD geometry developed for the MRA Preliminary Design Review (PDR). The cooling channel designs have since been improved for the Final Design Review (FDR).

Table 15. Thermal contact resistance with 0.1 mm helium gap

Contact	Gap Size, L (mm)	Helium, k (W/m-K)	R (m^2-K/W)
Lower/Middle Blocks	0.1	0.154933	6.4544E-04
Middel/Upper Blocks	0.1	0.154933	6.4544E-04
Upper/Shield Blocks	0.1	0.154933	6.4544E-04

Table 16. Thermal contact resistance with 1 mm helium gap

Contact	Gap Size, L (mm)	Helium, k (W/m-K)	R (m^2-K/W)
Lower/Middle Blocks	1	0.154933	6.4544E-03
Middel/Upper Blocks	1	0.154933	6.4544E-03
Upper/Shield Blocks	1	0.154933	6.4544E-03

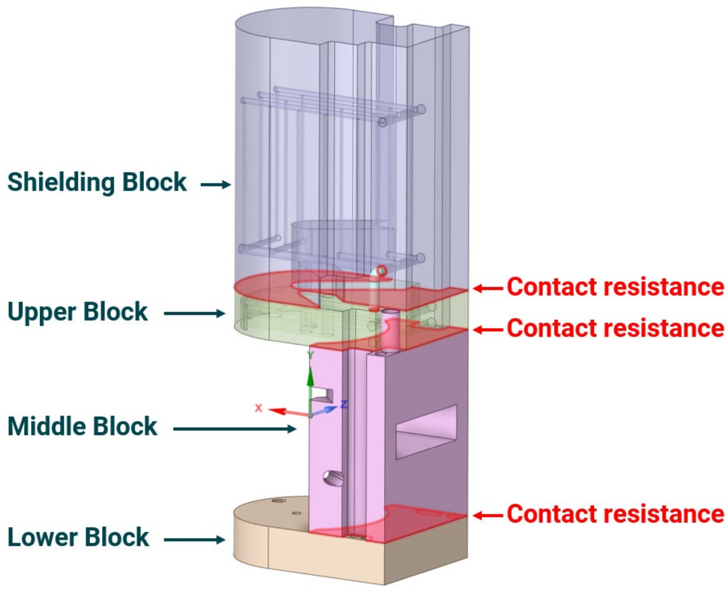

Figure 98. Contacts between blocks in MRA backbone.

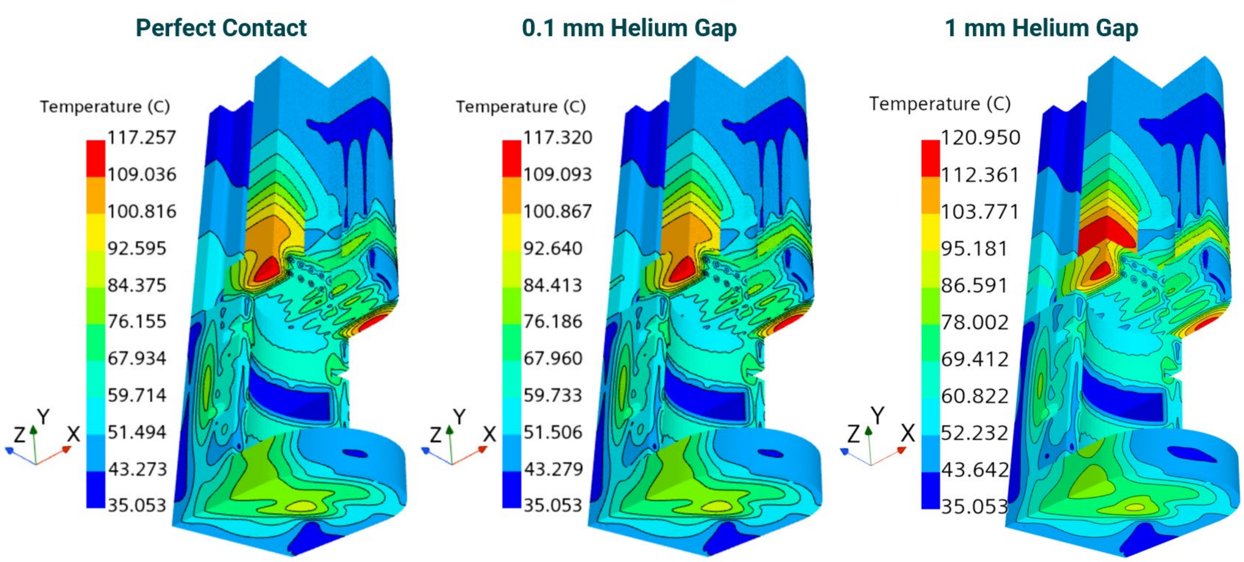

Figure 99. Impact of different sizes of helium gaps on the temperature distribution in MRA backbone.